DEVELOPMENT OF THE "ION SURFING" METHOD FOR THERMAL ION TRANSPORT IN BUFFER GAS

By

Amanda Elizabeth Gehring

A DISSERTATION

Submitted to
Michigan State University
in partial fulfillment of the requirements
for the degree of

Chemistry - Doctor of Philosophy

2013

ABSTRACT

DEVELOPMENT OF THE "ION SURFING" METHOD FOR THERMAL ION TRANSPORT IN BUFFER GAS

By

Amanda Elizabeth Gehring

Projectile fragmentation followed by in-flight separation produces radioactive nuclear beams (RNBs) at energies of ∼100 MeV/u and corresponding velocities of up to half the speed of light at the National Superconducting Cyclotron Laboratory (NSCL). In order to use nuclei produced at these high energies in low-energy experiments, the beams must be slowed to kinetic energies of ∼1 eV. Collection and thermalization of rare ions in a gas cell using static electric fields was first demonstrated at the NSCL [1]. Other gas cells have used radio frequency (RF) electric fields coupled to a static drift field to transport the ions through the helium buffer gas instead of a simple electrostatic field [2, 3, 4]. A new so-called "ion surfing" method for ion transport was proposed by Bollen [5] and demonstrated experimentally in this work through detailed measurements with thermal rubidium and potassium ions. These elements were found to be efficiently transported over distances of up to 40 cm in helium gas pressures ranging from 40 to 200 mbar. Transport speeds as high as 75 m/s and 60 m/s were reached for rubidium and potassium ions, respectively, at a gas pressure of 80 mbar. Measured ion speed and transport efficiencies were found to be in good agreement with the results of detailed ion transport simulations. This work validates "ion surfing" as a viable method to transport thermal ions in buffer gas and documents its preparation for use in next-generation beam thermalization devices.

For Ryan

ACKNOWLEDGMENTS

I am the product of great teachers.

From preschool through graduate school, I have been blessed with instructors who were kind and supportive as well as intelligent and hard-working. I am tempted to list them all by name, but I would inevitably leave someone out. Special thanks must go to a few of my primary educators. Thanks to Donna Craig for her excellent grammar instruction and for somehow instilling in me an appreciation of literature; to Jack Flagg for sharing his contagious love of learning; to my science teachers - to Kim Overman for introducing me to chemistry and physics and to Joe Overman for going the extra mile by offering a Physics II class just for me; and to my math teachers - Nicole Walters, Steve Walton, and my father, Chris, without whom I would not have received such excellent preparation.

At Rose-Hulman Institute of Technology, I was fortunate to have many professors who truly loved to teach and who went above and beyond their office hours to make sure I earned a top-level education. I owe Professor Dan Morris, Jr. a debt of gratitude for supervising my first research project and for his endless patience as I learned many valuable lessons, and Professor Mike Moloney also deserves my gratitude for supervising my physics research project and for altering it to include nuclear science. To the Chemistry, Physics and Optical Engineering, and Math departments - thank you truly is not enough!

At the graduate level, I must first thank the professors who served on my guidance committee - thank you to Paul Mantica for being my second reader and for organizing many nuclear chemistry gatherings, to Georg Bollen for being like a second advisor in his support and interest in my project, and to Brad Sherrill (and Sean Liddick as well) for mentoring me as I made my way through graduate school. Saving the best for last, thank you to my

advisor, Dave Morrissey, for his guidance and patience over the last five years.

I would be remiss if I did not thank several groups of people not only for the knowledge I have gained (both professional and about myself) due to their aquaintance, but also for their support and friendship. Thanks to Max, Stefan, Chandana, and the other members of the LEBIT/Gas Cell group. (Double thanks to Max - I have probably learned the most from him over the past three years, and all the La Fin du Monde in North America would not be enough to thank him!) Thank you to my fellow graduate students, especially the members of the LEBIT group and my officemates past and present, for your unwavering mental and moral support! Many members of the lab helped me with my project, and again my thanks really aren't enough to convey how deeply I valued all their cheerfully-given expertise. And to my friends who cheered me on in this endeavor - I appreciated your love and encouragement more than you know.

Finally, I must thank my parents, Chris and Kelly, and the rest of my family for always having faith in me. I thank God for the abilities he has given me, and I hope that I am making the most of them. This dissertation is dedicated to my husband, Ryan Smeltzer, for without him the past five years would have been much more difficult. I will forever appreciate his love and support through both the good days and the bad. I would like to secondarily dedicate this dissertation to two men who will not be able to celebrate its completion with me. The first is my late great-uncle, Professor Charles "Chuck" Gehring, who gave me priceless advice about graduate school as well as life, and I miss his ability to make the most out of every moment. The second is my grandfather, Delbert Flynn, whom I look to as the best example of a hard-working man who loves his family unconditionally. I know how happy and proud the two of them would be - they would probably even read this!

TABLE OF CONTENTS

LIST OF TABLES

LIST OF FIGURES

Chapter 1

Introduction

This work concerns the development of an electrode system referred to as "radio frequency (RF) carpets" for the transport of decelerated, thermal radioactive ions through helium buffer gas. Specifically, the "ion surfing" mode [5] of RF carpets was investigated and found to be the preferred method for ion transport due to its simplicity [12] and will be utilized in the next generation beam thermalization device at the National Superconducting Cyclotron Laboratory (NSCL), the so-called cyclotron gas stopper [16, 17, 18].

1.1 Rare Isotope Production at the National Superconducting Cyclotron Laboratory

In the field of nuclear science, rare radioactive nuclei are studied in order to investigate the general features of nuclear structure and astrophysical nucleosynthesis. Due to these nuclei being unavailable in nature (or not easily available), they must be produced in a laboratory environment. Moreover, the nuclei that are most interesting are generally very short-lived,

with half-lives on the order of fractions of a second, and must be made available for study before they decay. The production mechanism of the rare nuclei determines, to some extent, the range of accessible isotopes.

Radioactive nuclei have been produced at Isotope Separation On-Line (ISOL) facilities such as ISOLDE at CERN, HRIBF at ORNL, and ISAC at TRIUMF [19, 20, 21]. At ISOL facilities, radioactive nuclei are produced by directing a beam of high-energy protons or deuterons into a thick target. The target is heated to extract the volatile and chemically mobile reaction products. The isotope of choice has to be ionized and then mass-selected for study, and can be accelerated to higher energies. The availability of a specific isotope is limited by the time and, due to its chemical nature, difficulty of diffusion in the target, although nuclei with half lives as short as 8.8 ms have been measured in special cases at ISOL facilities [22]. Since the ions start essentially at rest, the quality of the resulting beam can be very high.

Projectile fragmentation [23, 24, 25] provides a physical selection process (chemically independent) with rapid transfer of the rare ions from production location to experiment. This method is employed at several facilities including GANIL, GSI, RIKEN, and the NSCL [24, 25]. At the NSCL, stable ions are accelerated to speeds as high as half the speed of light by two coupled cyclotrons, the K500 and K1200. The ions are impinged upon a low mass production target. (At the NSCL, beryllium is often chosen as the production target due to its high number density, solid state at room temperature, and ability to be handled easily in air [26].) Exotic beams, still at high speeds, are produced by the resulting nuclear collisions [25]. At the NSCL, the A1900 fragment separator is used to select the desired nuclei, determining the purity of the secondary beam that is then directed to an

experimental station [26]. Advantages of this method include the chemically independent nature of the production mechanism and the quick delivery of the isotopes to high-energy experiments [24, 25]. Properties of nuclei with half lives of ∼10 ms are routinely measured since the transport time to experiment (on the order of one microsecond) dictates the half-life limit of measurable isotopes [25].

The projectile fragmentation production method produces beams that are energetically unsuitable for low-energy precision experiments such as laser spectroscopy and Penning trap mass spectroscopy. The ions' energies must be reduced to lower, room temperature energies, or "thermalized," to facilitate the aforementioned precision experiments. Illustrated in Figure 1.1 are the overall features of the two production mechanisms. The goal of the present work is to improve the system for thermalizing and collecting the wide range of nuclei available from projectile fragmentation.

1.2 Low-Energy Experiments at the NSCL

A variety of experimental techniques have been developed at ISOL facilities for nuclear structure studies with thermal ions. For example, high precision Penning trap mass measurements of exotic nuclei are an important class of experiments in modern nuclear science [27]. These experiments are only possible with thermal beams and were first carried out at ISOL facilities [28]. The development of gas cells for projectile fragmentation have enabled Penning trap mass measurements of nuclei inaccessible at ISOL facilities [27, 28, 29, 30, 31]. This section gives a short summary of the experiments at the NSCL facilitated by the slowing and collecting of the produced rare isotopes.

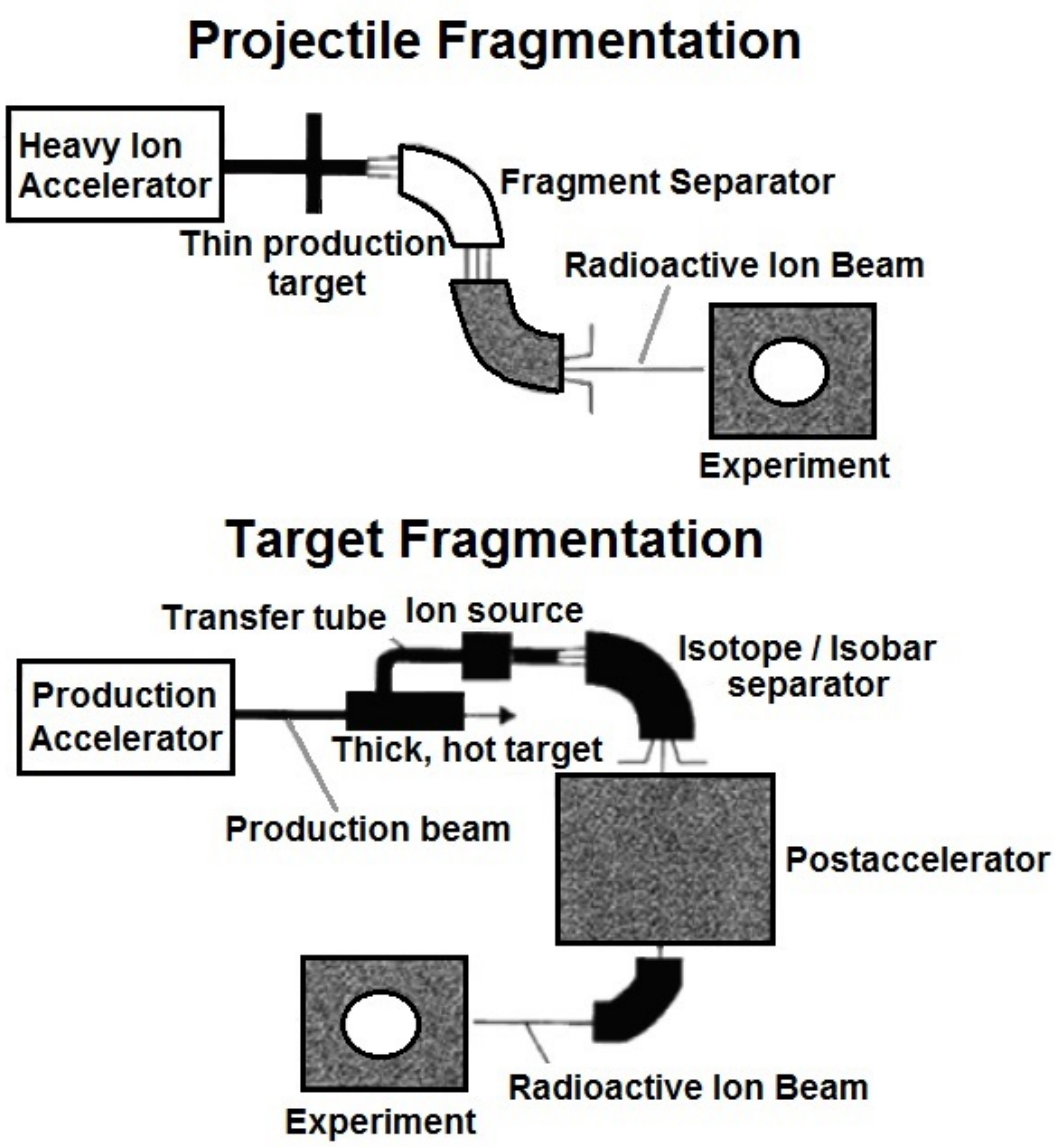

Figure 1.1: Schematic comparison of the ISOL and projectile fragmentation production mechanisms [6].

1.2.1 Penning Traps for Mass Measurements

Mass is one of the fundamental properties of a nucleus. Mass differences between neighboring nuclei give nucleon separation energies, which indicate the overall variation of nuclear structure and the limits of nuclear stability - the theoretical proton and neutron drip lines. Detailed information concerning nucleon interactions, shell and subshell closures, and nuclear deformation can be deduced from comparisons of mass measurements to theoretical mass models ([28, 29, 31], etc.).

Mass measurements can be performed indirectly or directly. Decay measurements, in which the total energy emitted in transitions between ground states is measured, are one example of an indirect method. Indirect methods based on β spectroscopy can achieve precision levels below 100 keV [32], but as the nuclei studied are increasingly farther away from stability, statistical uncertainties also increase due to the smaller number of available nuclei. Penning traps have become the devices of choice over the last decade for mass measurements of exotic nuclei due to their high precision and high sensitivity [27, 28]. The Low Energy Beam and Ion Trap (LEBIT) project at the NSCL has achieved precision on the order of 10^{-8}, or 1 keV for a typical short-lived exotic ion [28, 33, 34].

An early series of LEBIT experiments focused on nuclei along the N = Z line, important rp-process waiting point nuclei, and neutron-rich nuclei in the sulfur and phosphorous region up to N = 28 [27, 34]. The experiments were highly successful, and the masses of the following isotopes were determined with high precision: ^{26,32,33}Si, ^{29,34}P, ^{37,38}Ca, $^{40\text{-}44}$S, $^{63\text{-}66}$Fe, $^{64\text{-}67}$Co, $^{63\text{-}64}$Ga, $^{65\text{-}66}$Ge, $^{66\text{-}68,80}$As, $^{68\text{-}70,81,81\text{m}}$Se, and $^{70\text{m},71}$Br, which indicates the broad range of atomic number and half-lives that can be extracted and studied with this system after thermalization.

1.2.2 Laser Spectroscopy for Hyperfine Measurements

The BEam COoling and COllinear LAser (BECOLA) spectroscopy facility is a new addition to the low-energy program at the NSCL. Low-energy beams will be transported to a radio frequency quadrupole trap for storage, and then short pulses of ions will be injected into the laser polarizer beam line [35, 36]. A variety of measurements will be possible with the interaction of laser light with exotic ions and atoms. For example, β decay of the nuclear spin polarized nuclei will be measured by the Beta Nuclear Magnetic Resonance (βNMR) system, and laser spectroscopic experiments and the resulting hyperfine spectrum of the rare ions or atoms will lead to important nuclear properties including magnetic dipole moments, spectroscopic electric quadrupole moments, nuclear spins, and mean-square charge radii [35, 37]. Such properties can serve to test models of nuclear deformation, nuclear structure, and fundamental interactions [35].

1.2.3 Reaccelerated Beam Experiments

The ReA3 reaccelerator is currently under construction at the NSCL. Thermalized rare isotopes will be transported to a charge breeder and then to the reaccelerator [38]. The range of energies available from ReA3 is 0.3 to 6 MeV/u for ions of $A < 50$ with a maximum reaccelerated energy of 3 MeV/u for ^{238}U [38]. Examples of potential reactions at these energies include Coulomb excitation, fusion, and nucleon transfer [38]. Although similar beam energies are available at ISOL facilities, a more extensive selection of rare nuclei will be available at the NSCL due to the reliance on chemistry independent projectile fragmentation reactions [24, 25].

New experimental devices are being developed for the reaccelerated beams that will

produce new data relevant to the areas of nuclear structure and nuclear astrophysics. The Array for Nuclear Astrophysics Studies with Exotic Nuclei (ANASEN) will be used for inverse kinematics experiments such as (α,p) reactions [39]. The Active Target-Time Projection Chamber (AT-TPC) is a versatile apparatus that can be operated in two modes, active target and detector, and will be used to study isobaric analog states, light nuclei cluster structure, fission, giant resonances, and fusion and transfer reactions when operated in active target mode [40]. The Summing NaI(Tl) (SuN) detector will be used for (p,γ) and (α,γ) reaction experiments [41]. Lastly, the development of the SEparator for CApture Reactions (SECAR) is planned for investigating proton capture reactions at astrophysically relevant energies [38]. The Jet Gas Target JENSA will be used to study transfer reactions for SECAR. Thus, there is a large and varied range of equipment and experiments that require the efficient and rapid thermalization and collection of projectile fragments.

1.3 Beam Thermalization Overview

As summarized above, projectile fragmentation allows rapid access to a wide range of isotopes due to the chemically independent, in-flight production and separation. However, precision experiments and reacceleration of these ions require the starting energy of the rare ions to be $\sim$1 eV. At the NSCL, rare ion beams have energies of about 100 MeV/u and the reduction in energy from the high production energies to thermal energies of $\sim$1 eV requires an eight order-of-magnitude decrease [1, 30]. Energy straggling during the slowing-down process leads to final energy spreads so large that efficient collection is only possible in solid catchers. However, a solid catcher would possibly have similar chemical selectivity as the ISOL process due to problems with ion migration in the solid. Thus, gas cells are the only

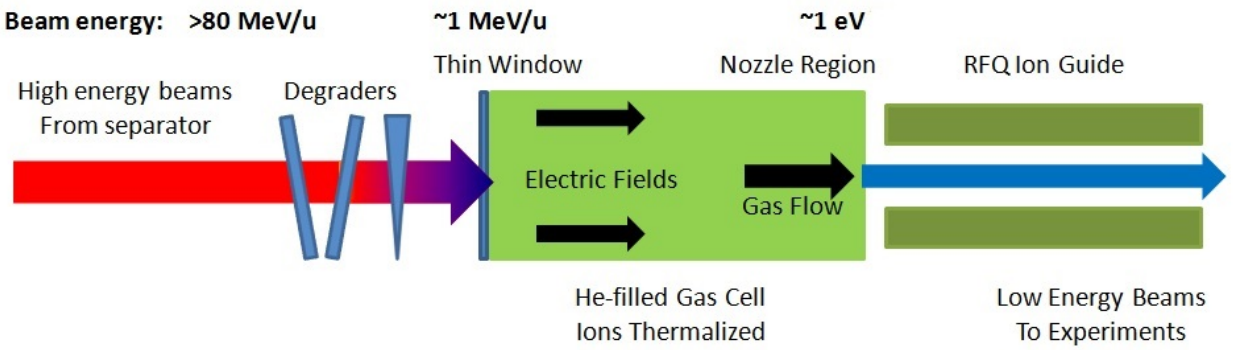

Figure 1.2: Schematic of the beam thermalization process. Most of the ions' kinetic energy is removed by the degraders before the ions pass into the gas cell. The ions are thermalized by the helium buffer gas and directed to the nozzle extraction region by electric fields [1]. For interpretation of the references to color in this and all other figures, the reader is referred to the electronic version of this dissertation.

tools available at present to collect and extract essentially all chemical elements.

A basic overview of a linear gas cell system is shown in Figure 1.2. The collection of nuclear recoils in a buffer gas was first employed in the Ion Guide Isotope Separator On-Line (IGISOL) systems [42]. Due to the low density of gases, solid degraders are necessary to remove most of the kinetic energy of the incident ions. A gas cell tens of meters long would be required to thermalize projectile fragments without upstream degraders, and the large amount of ionization depositied in the gas and the long extraction time would limit the range of unstable isotopes available due to radioactive decay during extraction [16, 17, 18]. In addition to the degraders, the ions pass through a window separating the gas chamber from the high vacuum of the beamline. The window separating the vacuum of the beamline from the gas chamber is generally thin, less than 1 mm [1, 3, 43, 44]. The window is made of material with a low atomic number to minimize energy loss, and the thickness is chosen to be as thin as possible with the mechanical strength to withstand the difference in pressure between the vacuum of the beamline and the pressure inside the gas cell without bowing.

The degraders are usually composed of borosilicate glass or aluminum [1, 3, 43, 45].

A wedge degrader can be used to compress the momentum range of the incident beam [1, 3, 43, 44] if the high-energy beam is suitably prepared by a dispersive magnetic dipole, resulting in a linear correlation between position and momentum so that the ions with higher momentum pass through the thicker part of the wedge [46, 47, 48, 49].

The stopping process is statistical in nature since not all ions will experience the same number and type of collisions, but the number of collisions is huge. Therefore, the ions will undergo an average energy loss as they pass through the degraders and will become thermalized in the gas over a range of longitudinal distances [50]. This range variability is called straggling. The degraders are rotated to an optimum thickness so that the ions have just enough energy to pass through the window into the gas cell and the maximum amount of the range straggling distribution falls inside the gas cell to maximize the number of stopped ions [1, 3, 45].

Thermal ions are guided through the buffer gas by electric fields and extracted through an orifice [1, 3, 43, 45]. Helium or argon is often chosen as the buffer gas so that a fraction of the nuclei remain ionized due to the high ionization potential of helium and argon relative to all the other chemical elements [1, 3, 51]. The extracted ions are then captured in a radio frequency quadrupole (RFQ) or sextupole after the orifice and transported through a differentially pumped region where the buffer gas is removed, and then to an experimental station [1, 3, 4, 45].

1.4 Gas Cells

A gas cell provides the essential transition between the high-energy secondary beams and the low-energy, high-quality beams required for low-energy precision experiments and reac-

celerator programs. The use of gas cells is now a well-established method for slowing ions produced from projectile fragmentation at RIKEN, NSCL, and GSI [1, 3, 4, 45]. This section provides an overview of the gas cells previously or currently in use at projectile fragmentation facilities. The limitations of the current systems are also discussed as motivation for the development of a next generation device, the cyclotron gas stopper under construction at the NSCL.

1.4.1 NSCL Gas Cell

The initial NSCL linear gas cell was commissioned in 2002 and successfully supplied the ions for the LEBIT precision mass measurement program until 2009 [9, 48, 49]. The degraders were a pair of rotatable borosilicate glass plates and an aluminum wedge for momentum compression, and the window separating the vacuum of the beamline from the cylindrical gas chamber was either 0.5 or 1.0 mm thick beryllium [1]. The ions were guided by a DC electric field and extracted through a supersonic nozzle [1]. The extraction efficiency was on the order of a few percent [1, 33].

1.4.2 Gas Cells at Projectile Fragmentation Facilities

Similar cylindrical-geometry, or "linear," gas cells have been developed at other facilities including Argonne National Lab (ANL), GSI, and RIKEN [3, 4, 44, 45]. At RIKEN, a combination of DC electric fields and a RF carpet transport the ions through the cell to a nozzle [3, 4]. RF carpets will be discussed in detail in Section 1.5.3. The first GSI cell for fast beams was developed at ANL then moved to GSI for testing with high-energy beams [2, 45, 51]. In this gas cell, DC electric fields transport the ions through the cell to a radio

Table 1.1: Comparison of lengths and pressures of current linear gas cells.

Lab	Cell Length (cm)	Gas	Gas Pressure (mbar)	Mass Thickness mg/cm^2
NSCL (1st cell) [1, 9, 33, 48, 49]	50	He	400-1000	3.28-8.21
GSI (ANL) [2, 45, 51]	120	He	175	3.45
		Ar	130	27.7
RIKEN [3, 4]	200	He	130	4.27
GSI (KVI) [43]	100	He	430*	7.06
NSCL (ANL) [52]	120	He	120	2.36

*The gas cell developed at KVI operates under cryogenic conditions at ∼85 K. This value is the room temperature equivalent pressure of the results in [43]. In future tests with fast beams, the room temperature equivalent pressure may be increased to ∼1200 mbar [43].

Table 1.2: Comparison of current linear gas cells: transport methods and efficiencies (in helium gas). The pressures are listed in Table 1.1.

Lab	Transport Method	Incoming Beam Energy (MeV/u)	Efficiency (Isotope) (%)
NSCL (1st Cell) [1, 9, 33, 48, 49]	DC Only	∼100	4 (^{38}Ca, ^{37}K)
GSI (ANL) [2, 45, 51]	DC + DC/RF Funnel	∼100 - 1000	1.8 (^{54}Co)
RIKEN [3, 4]	DC + RF Carpet	∼100	3 (^{8}Li)
GSI (KVI) [43]	DC + DC/RF Carpet	∼0.5*	
NSCL (ANL) [52]	DC/RF Body & Funnel	∼100	∼10 (^{76}Ge)

*The cell developed at KVI has only been tested with fission fragments.

frequency (RF) funnel region that converges towards a nozzle [2, 45, 51]. A gas cell was subsequently developed at KVI for use at GSI. This cell employs a DC gradient along the cell body with an RF carpet on the exit wall to direct ions to the extraction orifice, and it was the first cell to be operated at cryogenic temperatures [43]. Another linear cell was constructed at ANL for use at the NSCL (and FRIB). Ring electrodes line the body of this cell on which an RF signal and DC is applied, and the end of the cell is an RF + DC funnel [44]. Important features of these cells are summarized in Tables 1.1 and 1.2.

1.4.3 Limitations of Linear Gas Cells

As shown in Table 1.2, current devices have achieved efficiencies of 2-10%. In order to improve this efficiency, it is useful to investigate the causes of ion losses. As shown in Equation 1.1, the total gas cell efficiency consists of three components: the stopping, transport, and neutralization efficiencies. The source of each efficiency will be discussed in this section.

$$\epsilon_{total} = \epsilon_{stop}\,\epsilon_{trans}\,\epsilon_{neut} = \frac{N_{stop}}{N_{in}}\,\frac{N_{trans}}{N_{stop}}\,\frac{N_{ion,trans}}{N_{trans}} = \frac{N_{ion,trans}}{N_{in}} \tag{1.1}$$

The stopping efficiency, ϵ_{stop}, is the number of ions stopped in the gas, N_{stop}, divided by the total number of incoming ions, N_{in}. Not all ions can be thermalized within the gas cell due to range straggling and limits on the cell length. The rare isotope beam of projectile fragments is not monoenergetic - the ions have a range of kinetic energies primarily due to the production reaction and target thickness. The ions on the low end of this distribution may come to rest in the degrader. The ions at the high end of the distribution will encounter insufficient mass to successfully slow them to thermal energies; they will pass through the degrader and the buffer gas before being stuck in the back wall of the gas cell. Optimization of the stopping distribution, or range distribution, of the ions in the buffer gas increases the stopping efficiency and benefits all experiments that rely on the production of low-energy beams by thermalization of projectile fragments. The thickness of the degrader is adjusted in all of the devices to optimize the amount of ions that are stopped in the buffer gas [1, 3, 43, 45].

In order to discuss the stopping efficiency of a gas cell, a short summary of the relevant variables is useful. The linear stopping power, S, of ions passing through matter is defined as follows:

$$S = -\frac{dE}{dx} \tag{1.2}$$

where dE is the energy deposited over a path length, dx. The range R over which the ions come to rest in the absorber is:

$$R(E_0) = \int_0^{E_0} \frac{\mathrm{d}E}{S} \tag{1.3}$$

where E_0 is the initial kinetic energy of an ion. The Bethe-Bloch formula provides a theoretical description of the stopping power, also called specific energy loss. The formula is as follows [53]:

$$-\frac{dE}{dx} = \frac{4\pi e^4 z^2}{m_0 v^2} NZ \left[ln\frac{2m_0 v^2}{I} - ln\left(1 - \frac{v^2}{c^2}\right) - \frac{v^2}{c^2} \right] \tag{1.4}$$

where e is the fundamental electronic charge, c is the speed of light, z is the charge state of the projectile, v is the projectile velocity, m_0 is the electron rest mass, I is the average ionization and excitation potential of the impeding material, N is the atomic number density of the material, and Z is the atomic number of the material. Ions moving through matter lose the bulk of their energy through Coulombic interactions with the substance's electrons. Collisions with the nuclei of the material are much less common and have negligible effect on the energy loss of the ions. This formula has undergone many refinements, and several models and codes are available for predicting the stopping power of ions in various materials and the resulting range distributions. For example, the SRIM code (Stopping and Range of Ions in Matter) [50] is a Monte-Carlo-based calculation of the ions' energy loss based on tracking individual collisions. The ATIMA code provides an analytical calculation of the

stopping power specifically tailored for high-energy, heavy ions [54, 55].

In Equation 1.4, the ionization potential and atomic number of the stopping medium strongly influence the energy loss calculation. As aformentioned, helium is usually chosen as the stopping medium for linear gas cells due to its high ionization potential. The only other remaining variable that can be changed to increase the stopping efficiency is the number density of the matieral, which requires additional cell length and/or a higher gas pressure. The difference in the stopping power of the gas cells can be evaluated using these parameters by determining the mass thickness, the density of the buffer gas multiplied by cell length, which is a measure of the amount of matter the incoming ions encounter. An example varying these parameters for the first NSCL gas cell, the RIKEN gas cell, and the gas cell developed for GSI by KVI follows. The RIKEN gas cell is 200 cm long, and at 130 mbar and 293 K has a mass thickness of 4.27 mg/cm^2 [3]. The initial NSCL gas cell was 50 cm long, and at 1 bar pressure and 293 K the mass thickness was 8.21 mg/cm^2 [1]. Despite a length four times greater than that of the NSCL gas cell, the RIKEN cell's mass thickness is about half of the NSCL gas cell mass thickness due to its pressure being lower by about a factor of 8. The cell developed at KVI for GSI has target operating conditions of 250 mbar and 60 K, resulting in a mass thickness of 20.0 mg/cm^2 [43]. Cooling of the buffer gas leads to an increased mass thickness as compared to the two room temperature gas cells. These examples show the gains in mass thickness that can be obtained by varying the parameters of pressure, length, and temperature. However, as discussed below, the optimal collection of the ions occurs at lower mass density.

An increase in the mass thickness also increases the transport time of the ions through the cell due to increased collisions with buffer gas atoms. The collisions hinder the ions'

motion either by greater "resistance" (higher pressure, lower temperature) or by the longer distance the stopped ions must traverse (longer length). Increasing the time the rare ions drift in the gas cell is undesirable as it may lead to increased losses by radioactive decay.

All thermal ions will not successfully travel through the buffer gas to the extraction orifice. Ion losses can occur due to the collisions of the ions with the chamber wall or to the neutralization of the ions in three-body processes [8]. The transport efficiency, ϵ_{trans}, is the ratio of the number of ions transported through the cell, N_{trans}, to the number of stopped ions, N_{stop}. Space charge in the gas can also impede ion transport. Even though the projectile fragments have lost nearly all of their kinetic energy before entering the gas, each low-energy incident ion still generates $10^4 - 10^7$ ion-electron pairs in the buffer gas [8, 56]. The electrons are rapidly collected on the positive-charged electrodes due to their high mobility while the positive atomic ions remain in the gas. The positive residual charge builds up in the volume of the gas cell, creating space charge, and repelling the like-charged positive ions from the edges of the distribution into the walls. The extraction efficiency decreases in proportion to the square root of the ionization density and was found to be limited at ionization rates above $\sim 10^8$ ion pairs/cm^3/s [57]. To contain the ions driven to the wall by the space charge, RF fields have been used to repel the ions from the walls. RF electrodes were placed along the body of the second generation gas cell developed at ANL for the NSCL [44], and the RF funnels or RF carpets present in the RIKEN [3, 4], GSI (from ANL) [2, 45, 51], and GSI (from KVI) [43] gas cells also serve to repel the ions from the surface of the electrodes as the ions are transported through the cell.

Finally, the neutralization efficiency, ϵ_{neut}, is the fraction of the transported ions that remain charged, $\frac{N_{ion,trans}}{N_{trans}}$. Studies at KVI [58, 59] suggested that the neutralization effi-

ciency may be limited to about 30%. However, there is relatively little information on this fraction and further studies are needed to see, for example, if ϵ_{neut} depends on the ionization potential of the thermalized species.

1.5 The Cyclotron Gas Stopper

The performance and limitations ($\epsilon_{total} \leq 10\%$) of the current linear gas cells at projectile fragmentation facilities were outlined in the previous section. The NSCL is constructing the next generation gas stopping device, the cyclotron gas stopper, with a larger momentum acceptance, longer stopping path length (allowing lower operational pressures), and ion transport with RF carpets. In addition, operation under cryogenic conditions will improve beam purity. These changes will address many of the shortcomings of the current linear gas cells.

The performance of the cyclotron gas stopper is highly dependent on the properties of the incoming ion beam. A new momentum compression beam line, called the "AC-line," has been constructed in the N4 vault. Momentum compression of the beam profile will increase the maximum momentum acceptance of the gas cell from 0.5% to 2%. The momentum dispersion at the wedge position is 1.8 cm/% at the entrance to the gas cell, so the spatial range of incident ions will fall within the beam pipe inner diameter of 10 cm. It is noted, however, that the maximum spread in momentum is 5% after the A1900 fragment separator, so even the planned improvements will not permit acceptance of all of the produced fragments.

1.5.1 Increased Path Length

As discussed in the previous section, the stopping efficiency of ions in buffer gas can be improved by increasing the amount of gas used to collect the ions. In the cyclotron gas stopper [16], the ions will decelerate in the presence of a ∼2 T magnetic field, causing their trajectories to spiral inwards [16, 17, 18]. Similar devices have been developed for slowing pions, muons, antiprotons [60, 61], and proposed for light ions [62]. The gas volume also differs from previous beam thermalization devices; instead of a cylinder along the incoming beam axis, the gas volume of the cyclotron gas stopper will have a squat cylindrical shape, and the beam will enter the device tangentially at the edge of the cell [16, 17, 18]. See Figure 1.3 for a schematic of the cross section of the cyclotron gas stopper. Since the ions make multiple circuits in the gas as they spiral to a stop, the mass thickness that the ions encounter can be large. Simulations have shown that the typical stopping radius from the central extraction orifice is ∼30 cm regardless of ion identity [7]. In Figure 1.3 is shown the simulated stopping region and energy deposition by singly-charged ^{79}Br ions in 120 mbar of helium gas [7]. The ^{79}Br ions complete about 5 revolutions at a radius of ∼35 cm [7], which corresponds to a mass thickness of 18.5 mg/cm^2. Lighter ions will require more revolutions to thermalize [7]. For example, a mass thickness of 74 mg/cm^2, or 20 revolutions at 30 cm and 120 mbar, is shown by simulations to be necessary to slow singly-charged ^{24}O ions [7]. The increased stopping path length leads to higher stopping efficiencies [16, 17, 18].

The cyclotron gas stopper will be cooled with liquid nitrogen to ∼80 K. An increased buffer gas density was not the objective of cooling the buffer gas given the increased stopping path length. The cryogenic conditions provide another significant improvement, as discussed in the next section. The simulations mentioned previously were performed with room tem-

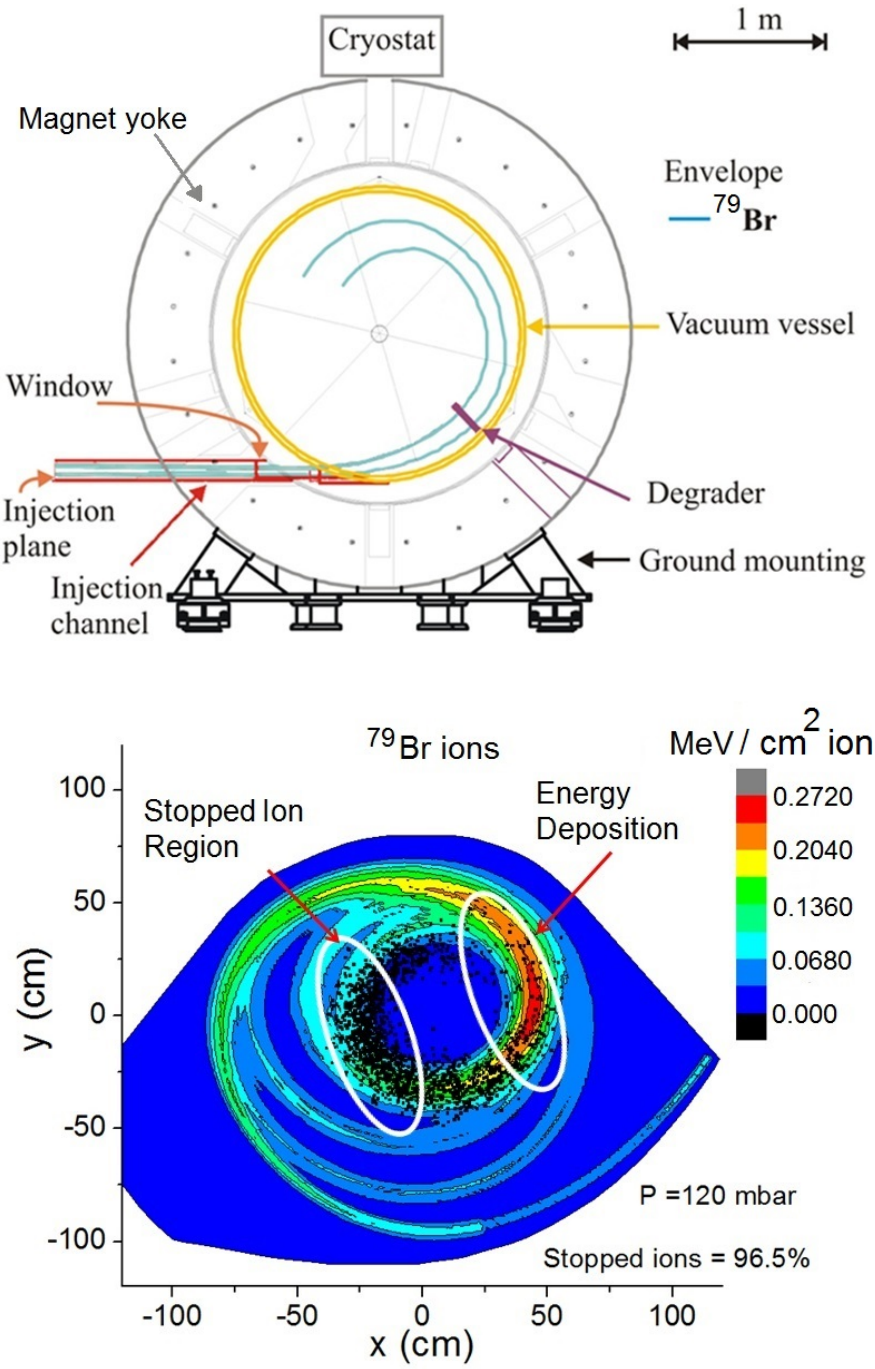

Figure 1.3: (Left) Schematic of the cross section of the cyclotron gas stopper. The blue lines designate the beam envelope of the first turn of the incoming ^{79}Br ions [7]. (Right) Simulated stopping region and energy deposition of ^{79}Br in 120 mbar of helium gas. A high stopping efficiency (96.5%) is achieved [7] in the simulation.

perature buffer gas at 80-120 mbar to compare the expected performance to current room temperature experimental results. The actual device will operate under the same buffer gas density conditions, which corresponds to 20-30 mbar at 80 K.

1.5.2 Cryogenic Conditions

Gaseous impurities in the helium gas originate from outgassing of the chamber, backstreaming of vacuum pumps, and the supply gas itself. The impurities reduce the extraction efficiency by binding to the thermalized rare ions and distributing the radioactivity over a range of molecular ions [8]. In addition, the contaminants undergo charge exchange with the copious He_2^+ ions and are extracted as stable, molecular ion beams [8]. During a number of LEBIT experiments, over 100 molecular ion contaminants were extracted and identified from the first generation NSCL gas cell, even though extremely pure helium gas was used and care was taken to bake and clean surfaces and to minimize backstreaming from vacuum pumps. A sample of these ions observed coming from the first NSCL gas cell under typical operating conditions is displayed in Figure 1.4. The molecular ions were a possible source of isobaric contamination depending upon the mass of the rare isotopes measured by LEBIT.

Current room temperature gas cells typically have impurities in the ppb range [8]. The cyclotron gas stopper will be cooled by liquid nitrogen to $\sim$80 K. At operational pressures, the majority of molecular contaminants are expected to freeze out of the gas phase so that the extracted beams should be more pure.

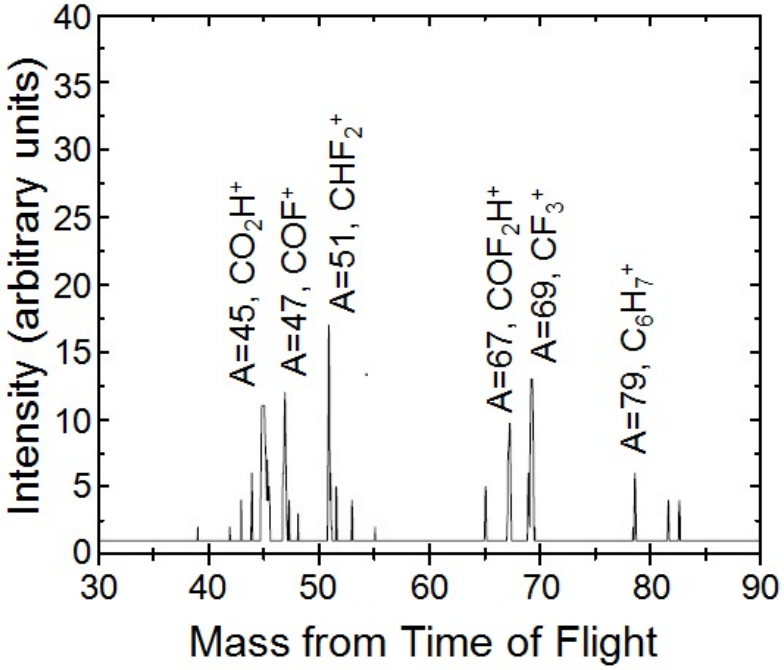

Figure 1.4: Example of contaminant molecular ions identified from gas cell discharge tests by time-of-flight [8].

1.5.3 Radio Frequency "RF" Carpets

In linear gas cells, the radial electric field caused by space charge in the cell pushes the rare ions towards the wall, limiting extraction efficiency to a few percent [56] (See Table 1.2). A novel technology was developed at RIKEN [3, 4] to transport ions in a buffer gas using oscillating RF electric fields applied on 2D arrays of parallel or concentric electrodes called "RF carpets." The oscillating electric field from adjacent electrodes results in a small net repelling force that prevents slow-moving positively charged ions from colliding with the electrodes. The RF carpets used in RIKEN are shown in Figure 1.5. A DC gradient is superimposed on the electrodes, in addition to the RF signal, to guide the ions to the extraction orifice.

The focus of the work was to develop a configuration of RF carpets for use in the cyclotron

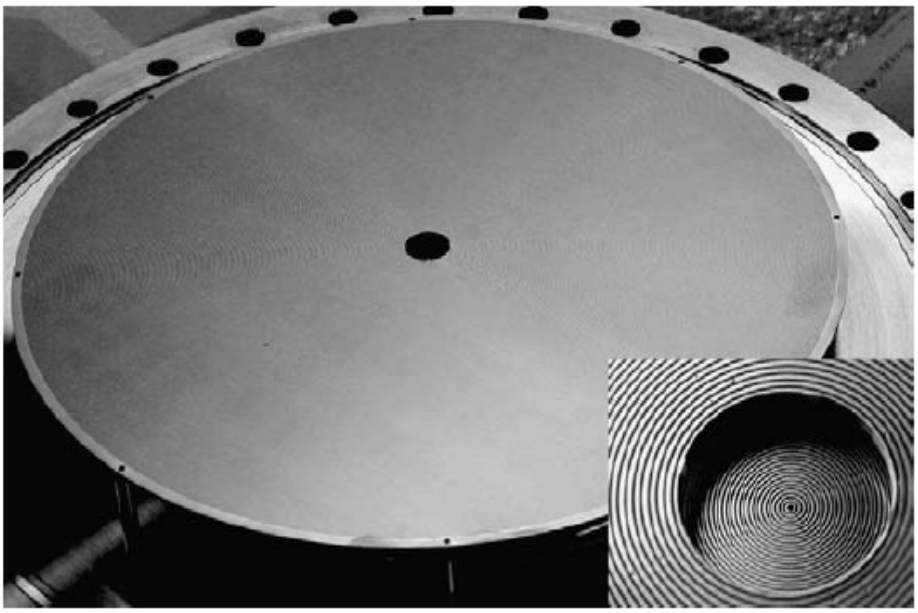

Figure 1.5: The RF carpets used in the RIKEN gas cell. The inset shows a close-up of the central region and the smaller carpet. The upper and lower carpets have trace and space widths of 0.25 mm and 0.155 mm, respectively. The upper carpet has a 29 cm diameter, and the opening is 10 mm in diameter. The extaction orifice of the lower carpet has a diameter of 0.6 mm [3].

gas stopper and to build on the initial studies of RF carpets completed at the NSCL by Pang [10]. In Section 1.5.1, nearly all of the ions were shown to stop in the cyclotron gas stopper at about 30 cm from the extraction orifice in the center of the device [7] (See Figure 1.3). The goal was to direct the thermalized, decaying rare ions to the extraction orifice as quickly and efficiently as possible. In order to be efficient, the RF carpets must cover a large fraction of the bottom of the gas cell, which requires a diameter of 90 cm, much larger than that of the RF carpets in the RIKEN gas cell (29 cm, [3]). The RF carpets are necessary to prevent the ions from colliding with the chamber walls due to the build up of space charge in the gas cell [63]. The development of large RF carpets presented many challenges. Initial work was performed using the traditional method of superimposing a DC gradient on the RF field [10]. Recently, the "ion surfing" method, in which the DC gradient is replaced by

a traveling wave, was proposed and numerically studied [5]. A predicted advantage of the surfing method is the decrease in the transport time of the stopped ions in the cell. Such a decrease in transport time will aid in rapid extraction of the shortest-lived rare isotopes and make them accessible to end users. A thorough explanation of the "ion surfing" method and its advantages is given in Chapter 2. The experimental demonstration of the "ion surfing" method as a viable and predictable means of rapid ion transport is presented in the remaining chapters of this dissertation.

Chapter 2

The "Ion Surfing" Method for RF Carpets

The manipulation and transport of ions with electric fields is a crucial technique necessary in many scientific experiments, from mass spectrometry to Penning traps. The use of RF fields in the form of funnels, small ring electrodes, or carpets to repel ions from the walls of a gas cell is a relatively new application, but with roots in quadrupole ion confinement. This chapter describes the general operation of RF carpets and the specific method of ion surfing developed in the present work. In the ion surfing method, the ions are transported along the surface of an RF carpet by a traveling wave potential.

2.1 Electric Potentials and Fields

Ion transport with RF carpets via the ion surfing method relies on the interaction of three different electric fields to capture and move thermal ions in a buffer gas. An oscillating RF potential which creates an effective potential that repels the ions from the electrodes' surface

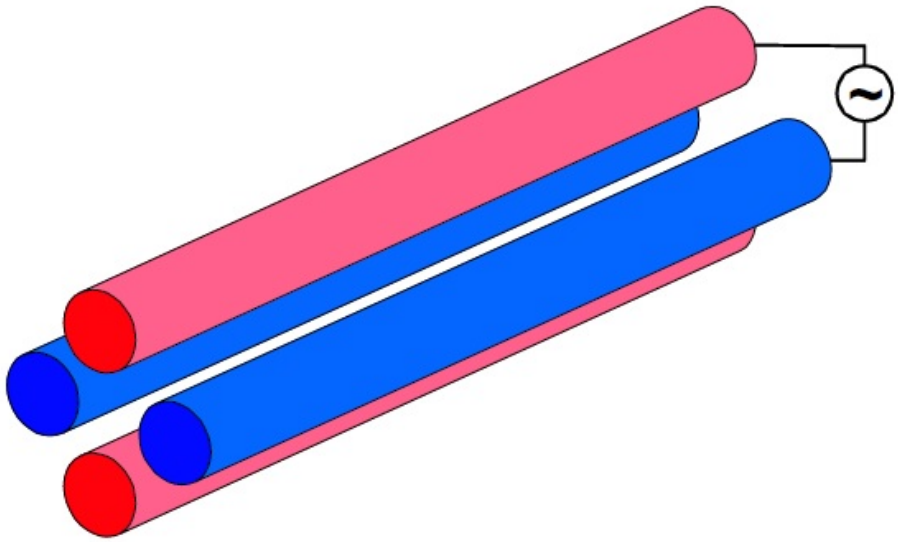

Figure 2.1: A simple cartoon of a quadrupole. The potentials applied to the two sets of rods oscillate 180 degrees out of phase. The oscillating potential creates an inhomogeneous electric field that confines ions within the quadrupole to its center [9].

is applied to the RF carpet electrodes (Section 2.1.1). A lower frequency and amplitude potential is superimposed onto the RF signal, forming a traveling wave that carries the ion along the carpet (Section 2.1.2). A push field is created by an electrode (or electrodes) above the carpet to direct the ions towards the RF carpet suface so that the ions can be transported by the traveling wave potential (Section 2.1.3). The general features of each potential are discussed in the following sections.

2.1.1 RF Effective Potential

In order to describe the repelling potential generated by the RF potential on the carpet electrodes, consideration of the trapping potential created by a quadrupole ion guide is useful. Quadrupole systems used for confining (and transporting, as in the RFQs after the gas cells in [1, 45] or more commonly in quadrupole mass spectrometry [64]) ions consist of

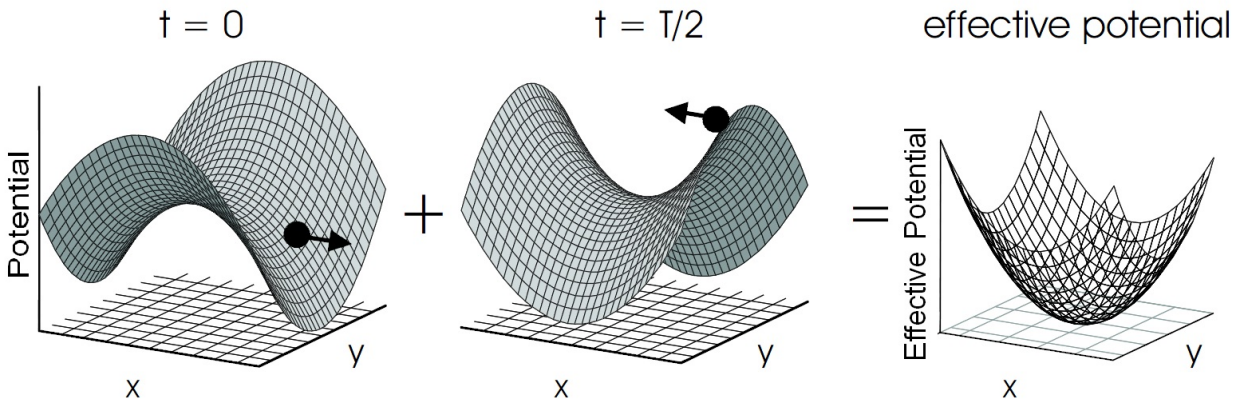

Figure 2.2: Left: An instantaneous snapshot of the potential experienced by an ion in the quadrupole at time zero. Center: The instantaneous potential when the time corresponds to half of the oscillation period, T. Right: The effective potential that traps the ion in the center of the quadrupole is due to the oscillation of the instantaneous potentials [9].

two sets of parallel hyperbolic or circular rods as shown in Figure 2.1. The potential applied to the first set of rods, V_t, oscillates in time, t, as follows:

$$V_t = V_0 \cos(\Omega t) \tag{2.1}$$

where V_0 is the amplitude and Ω is the frequency of oscillation (in rad/s). In order to trap ions along the central axis, the potential on the second set of rods is identical in amplitude and frequency but 180 degress out of phase. Instead of a homogeneous electric field, which would be produced by an alternating electrical signal on parallel plates, the curved shape of the rods produces an inhomogeneous electric field. Instantaneous visualizations of the potential experienced by an ion in the fluctuating quadrupole field is shown in Figure 2.2 (left and center) [9]. If the frequency of the oscillating potential is high compared to the drift velocity of the ion (on the order of MHz), the resulting small net repelling force produces an effective or pseudo-potential, the minimum of which lies along the central axis of the quadrupole, as depicted in Figure 2.2 (right). Slowly-moving ions within the rods are

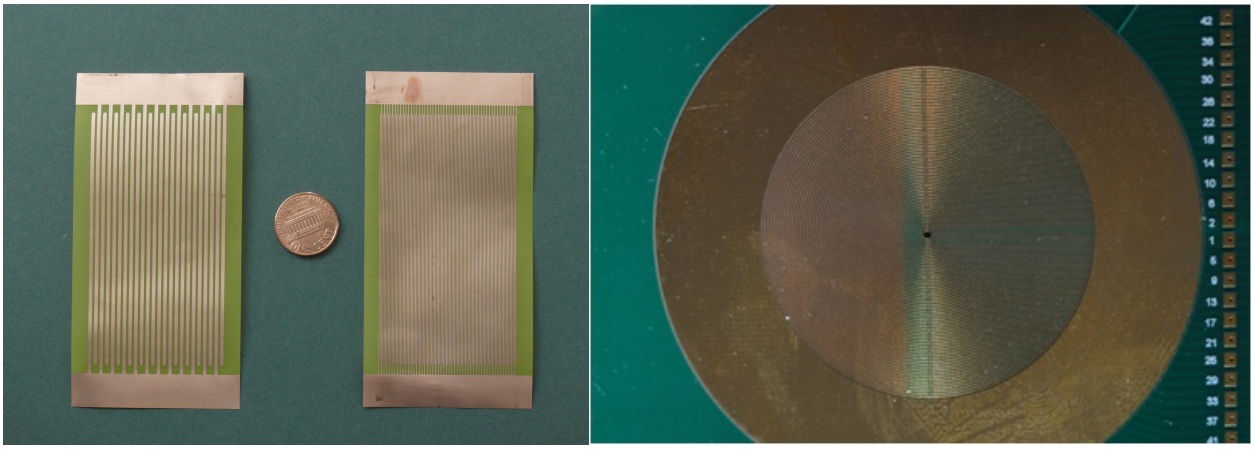

Figure 2.3: Examples of the two RF carpet electrode geometries. Left: RF carpets with linear electrodes (and two different pitches) used by Pang [10]. The pitch, a, is the sum of one electrode and one gap width. Right: RF carpet with concentric electrodes developed and employed by Wada [3].

then driven to the middle. The gradient of the inhomogeneous field increases with distance away from the center of the quadrupole, generating the focusing effect. The operation of quadrupole ion guides and mass filters is extensively described in the literature (see, e.g. Ref. [64]).

Similar to a quadrupole system, an RF carpet consists of electrodes onto which an oscillating potential is applied 180 degrees out of phase on successive electrodes. However, unlike a quadrupole, this potential is applied to hundreds, sometimes more than a thousand, of electrodes over the carpet surface [3]. Typically, RF carpet electrode geometries are a series of repeating long, narrow stripes or concentric rings. Examples of different carpet geometries are shown in Figure 2.3. The effective potential generated by the RF signal for a linear carpet geometry was derived by Schwarz [11] using the Dehmelt model [65] and is given by the expression:

$$V_{eff} = \frac{e}{4m\Omega^2}E_0^2 = \frac{e}{4m\Omega^2}(E_x^2 + E_y^2). \tag{2.2}$$

Here E_x is the electric field in the plane of the RF carpet perpendicular to the length of the electrodes and E_y is the electric field perpendicular to the carpet surface. E_x and E_y are given as:

$$E_x = \frac{V}{\gamma a \pi}\left[\arctan\left(\frac{\cos(\pi[\frac{\mathrm{x}}{\mathrm{a}} - \frac{\gamma}{2}])}{\cosh(\pi\frac{\mathrm{y}}{\mathrm{a}})}\right) - \arctan\left(\frac{\cos(\pi[\frac{\mathrm{x}}{\mathrm{a}} + \frac{\gamma}{2}])}{\cosh(\pi\frac{\mathrm{y}}{\mathrm{a}})}\right)\right] \tag{2.3}$$

$$E_y = \frac{V}{2\gamma a \pi}\ln\left[\frac{\cosh(\pi\frac{\mathrm{y}}{\mathrm{a}}) + \sin(\pi[\frac{\mathrm{x}}{\mathrm{a}} + \frac{\gamma}{2}])}{\cosh(\pi\frac{\mathrm{y}}{\mathrm{a}}) - \sin(\pi[\frac{\mathrm{x}}{\mathrm{a}} + \frac{\gamma}{2}])}\,\frac{\cosh(\pi\frac{\mathrm{y}}{\mathrm{a}}) - \sin(\pi[\frac{\mathrm{x}}{\mathrm{a}} - \frac{\gamma}{2}])}{\cosh(\pi\frac{\mathrm{y}}{\mathrm{a}}) + \sin(\pi[\frac{\mathrm{x}}{\mathrm{a}} - \frac{\gamma}{2}])}\right], \tag{2.4}$$

where V is the amplitude of the RF potential, a is the pitch of the carpet (sum of one electrode and one gap width), and γ is the ratio of the gap width to the pitch [11]. Since the RF carpets are generally operated in the presence of buffer gas, a damping factor, D [3, 66], must be added to Equation 2.2 as follows [11]:

$$V_{eff,damp} = \frac{\Omega^2}{\Omega^2 + D^2} V_{eff} = \frac{eE_0^2}{4m(\Omega^2 + D^2)}. \tag{2.5}$$

D is calculated from the ion's charge, e, mass, m, and mobility constant, K:

$$D = \frac{e}{mK} \tag{2.6}$$

The ion mobility constant is a well-known function of temperature, T, and buffer gas pressure, p (in mbar) and is defined as follows:

$$K = K_0 \frac{1013[mbar]}{p}\frac{T}{273.15[K]}, \tag{2.7}$$

where K_0 is the reduced ion mobility, which is 20 $\frac{cm^2}{V*s}$ for a typical 1^+ ion in helium

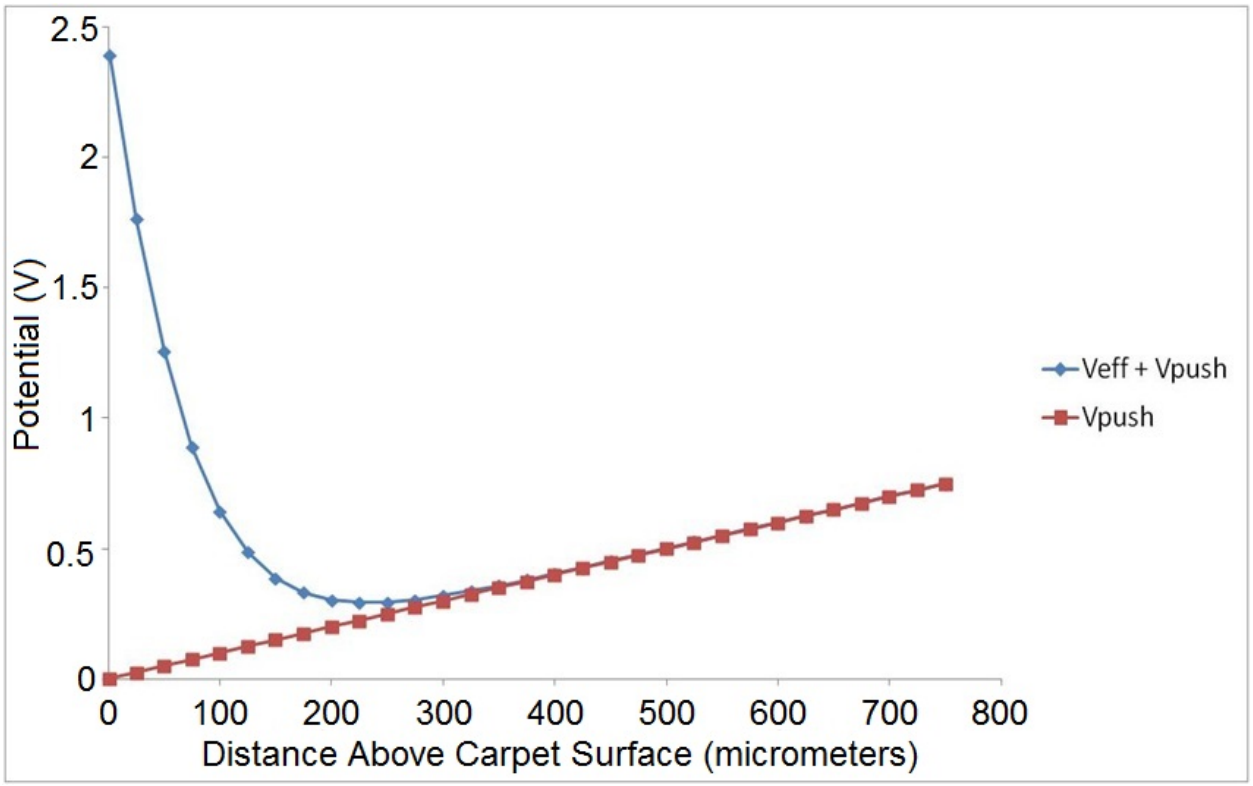

Figure 2.4: The potential experienced by a 85 u, singly-charged ion in 100 mbar of helium buffer gas under the following conditions: RF carpet pitch = 0.375 mm, gamma = 0.67, RF frequency = 8.38 MHz, RF amplitude = 75 V, and push field = 10 V/cm. Blue line: The combined push and effective potentials. The effective potential was calculated with Equation 2.5. Red line: The push potential only.

buffer gas [67]. Most thermalized ions remain in a singly-charged state (the other elements in a doubly-charged state) due to the high ionization potential of helium. An example of the damped effective potential, calculated with the previous equations, is shown in Figure 2.4. The push potential varies linearly with position above the carpet, which results in a constant push field, but the repelling field increases sharply near the carpet. The combination of push and repelling fields produces a pocket or minimum above the carpet surface.

The parameters most important in RF carpet design are a, γ, Ω, and V. First, the carpet pitch, a, and gap-to-pitch ratio, γ, are inversely proportional to the electric fields in the first term of the Equations 2.3 and 2.4, and determine the trigometric components

of the equations as well. In this work, carpets with different pitches, all having $a < 1$ mm, and various values of γ were tested, and the results will be presented and discussed in subsequent chapters. The RF frequency, Ω, and amplitude, V, also strongly affect the repelling force, and the increase in the attainable RF frequency of the carpets over the course of the experiments was found to greatly improve the ion transport efficiency. The effect of pitch and RF frequency on the repelling force is shown in Figure 2.5. The repelling force increases with decreasing pitch, a, and has a maximum in frequency for a given pitch.

Also, as the pressure of the buffer gas increases, the effective potential should decrease based on the relations shown in Equations 2.5, 2.6, and 2.7. The key parameter is the damping factor, which is proportional to pressure and appears as a squared term in the denominator of Equation 2.5. As a result, the transport of ions at higher pressures becomes more difficult. The decrease in the effective potential with pressure is illustrated in Figure 2.6. Note that the repelling potential drops sharply when the pressure is increased from 2 to 200 mbar, and the minimum distance of the ions above the carpet surface moves closer to the carpet surface. The six curves in Figure 2.6 were calculated at the six positions relative to the carpet electrodes as shown in the inset on the right hand side of the figure [11].

2.1.2 Push Field

The push field is generated by an electrode placed above the carpet surface. The carpet electrodes are unbiased, they are at 0 V (ground). This field guides the ions towards the carpet surface so that they can be collected by the traveling wave. In Figures 2.4 and 2.6 are shown examples of the potential minimum created by the effective potential and push field a short distance above the RF carpet surface. The combination of all three

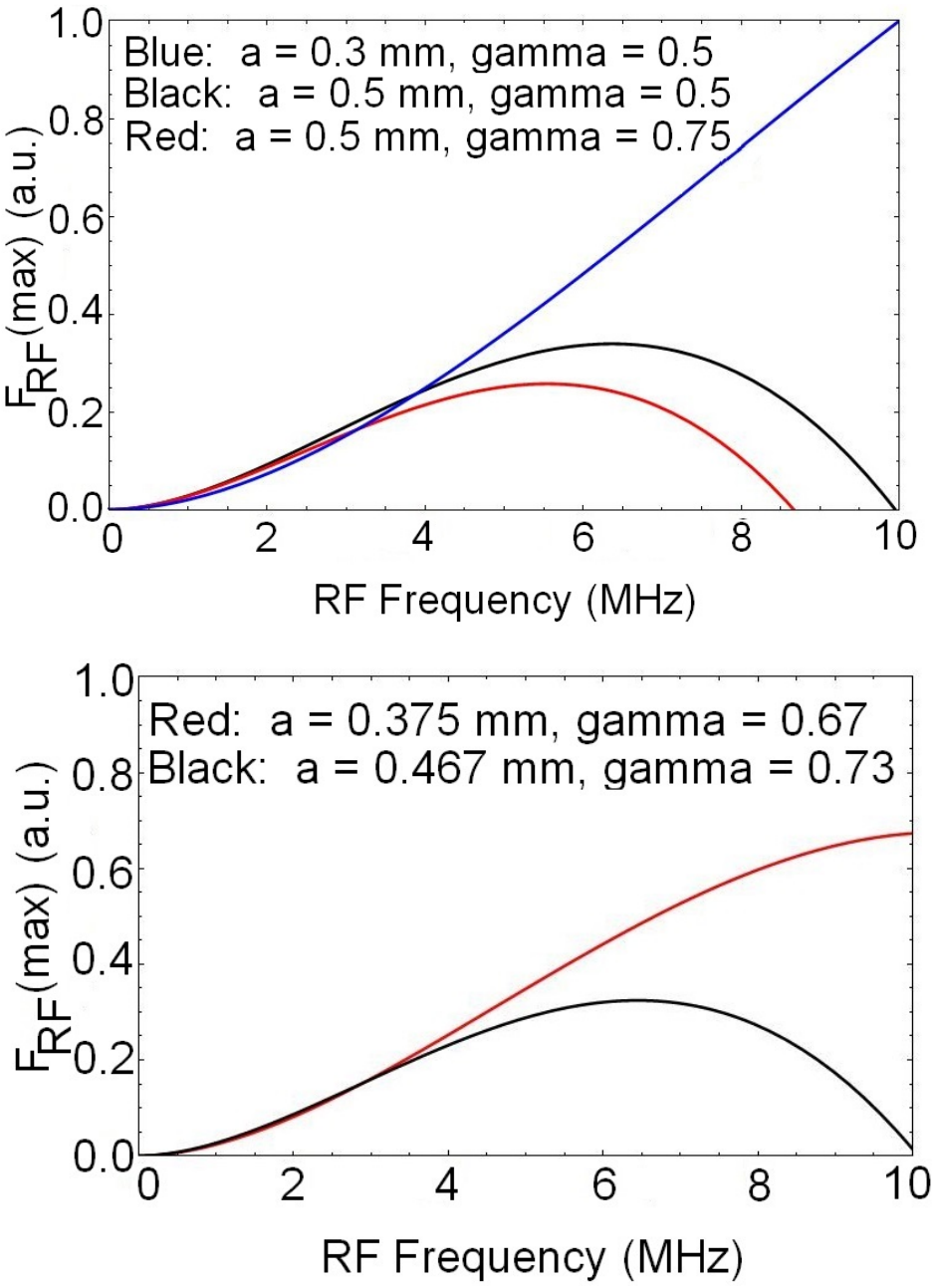

Figure 2.5: Comparison of the repelling force on a 23 u singly-charged ion for the various values of carpet pitch studied in this work as a function of RF carpet frequency. The units have been normalized to the value for pitch = 0.3 mm, $\gamma = 0.5$ at 10 MHz. A helium gas pressure of 100 mbar, temperature of 295 K, and a RF amplitude of 75 V were used in the calculations. Above: The blue and black curves demonstrate the effect of reducing the pitch of an RF carpet. Larger pitch sizes generate lower repelling fields, and the maximum repelling frequency occurs at lower values. The black and red curves illustrate the lesser effect of altering the γ of a RF carpet. Below: The max repelling force curves for two additional RF carpets discussed in this work.

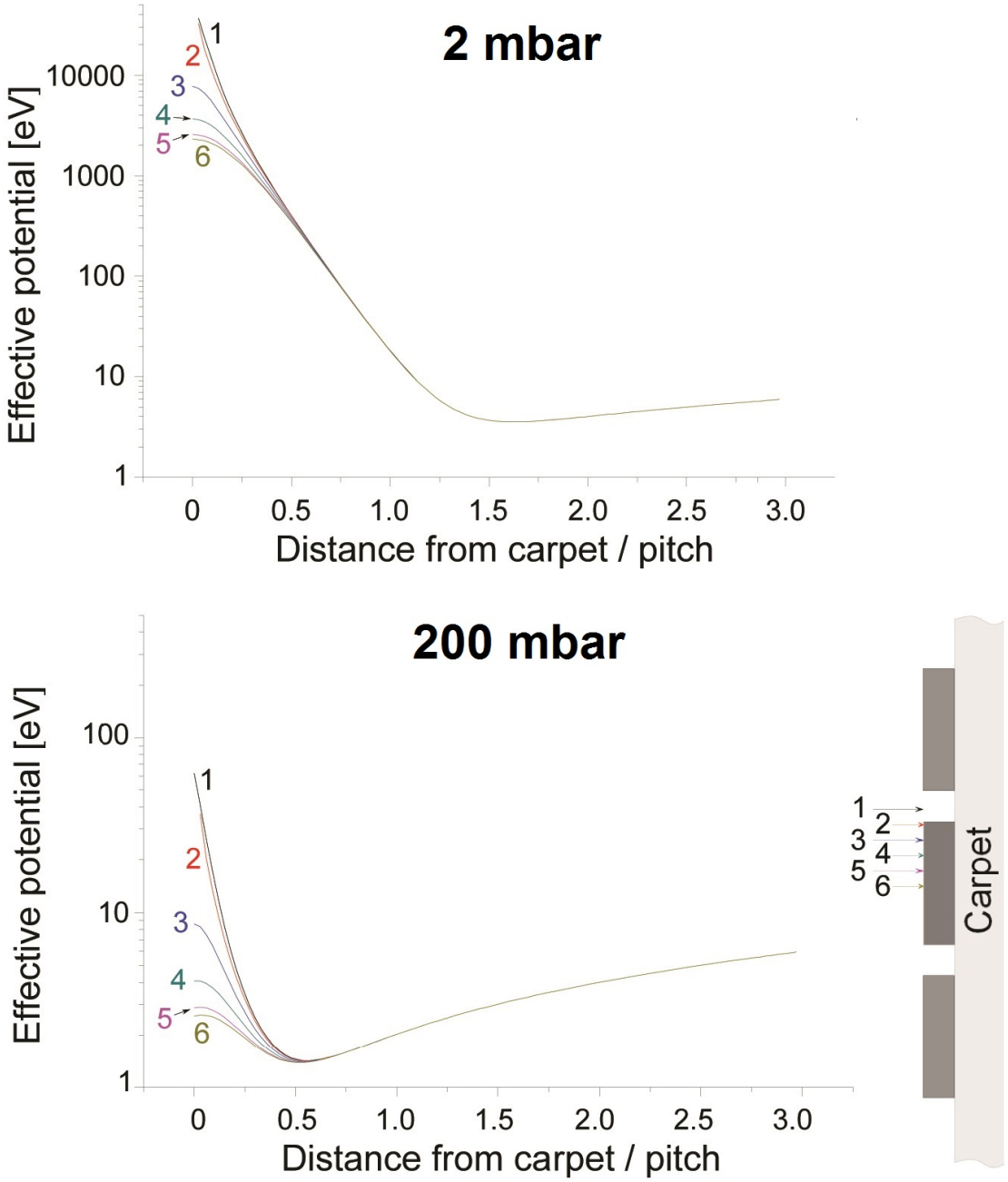

Figure 2.6: The calculated effective potential for six positions between two Rf electrodes (shown below right). The potential from a 20 V/cm push field is added to generate the potential minimum. The change in pressure from 2 mbar (above) to 200 mbar (below) results in a reduction of the minimum repelling potential by about two order of magnitude, which allows the ions to move closer to the carpet surface [11]. Note that the abscissa is the distance from the carpet in units of the carpet pitch. The parameters used in this calculation are as follows: a = 1 mm, $\gamma = 0.2$, A = 40 u (+1 ion), V_{RF} = 200 V, RF Frequency = 1 MHz, and T = 300 K.

potentials is presented in Figure 2.9. The push field must be large enough to form a potenital minimum capable of containing the ions, but not so great to overwhelm the repelling potential preventing the ions from hitting the carpet electrodes. The maximum push field an ion can withstand was derived in Ref. [11]:

$$E_{push,max} = \frac{ma}{q\pi}\Omega^2 \left[1 - 1.09\sqrt{\frac{a^2\Omega}{8VK_0}\frac{p/1013}{T/273.15}\frac{\gamma}{\sin(\frac{\pi\gamma}{2})}}\right] \tag{2.8}$$

Again, raising the gas pressure of the system presents a disadvantage since the maximum push field an ion can withstand decreases with the square root of the pressure. As expected, increasing the RF amplitude, V, also increases the maximum push field. The effect of the frequency on the maximum repelling field was illustrated in Figure 2.5 (the maximum push field an ion can withstand corresponds to the maximum repelling force). The effect of varying the carpet pitch, a, the value of γ, and RF frequency on the maximum repelling force is shown in Figure 2.7. A carpet pitch of 0.375 mm was selected for the calcuation in Figure 2.7 (below) because 0.375 mm is the current minimum pitch manufacturing limit for flex substrate carpets.

2.1.3 Traveling Wave Potential

The combination of the repelling RF potential and the push field contains the ions at a small distance above the electrode surface but does not transport the thermal or drifting ions to the exit of a gas cell. The flow of the buffer gas through the system is insufficient to efficiently transport the ions except for the region of the cell within a few millimeters of the extraction orifice. The simplest mode of transport is to superimpose a linear voltage on the carpet electrodes to move the ions [3, 10, 43]. However, difficulties with electrical

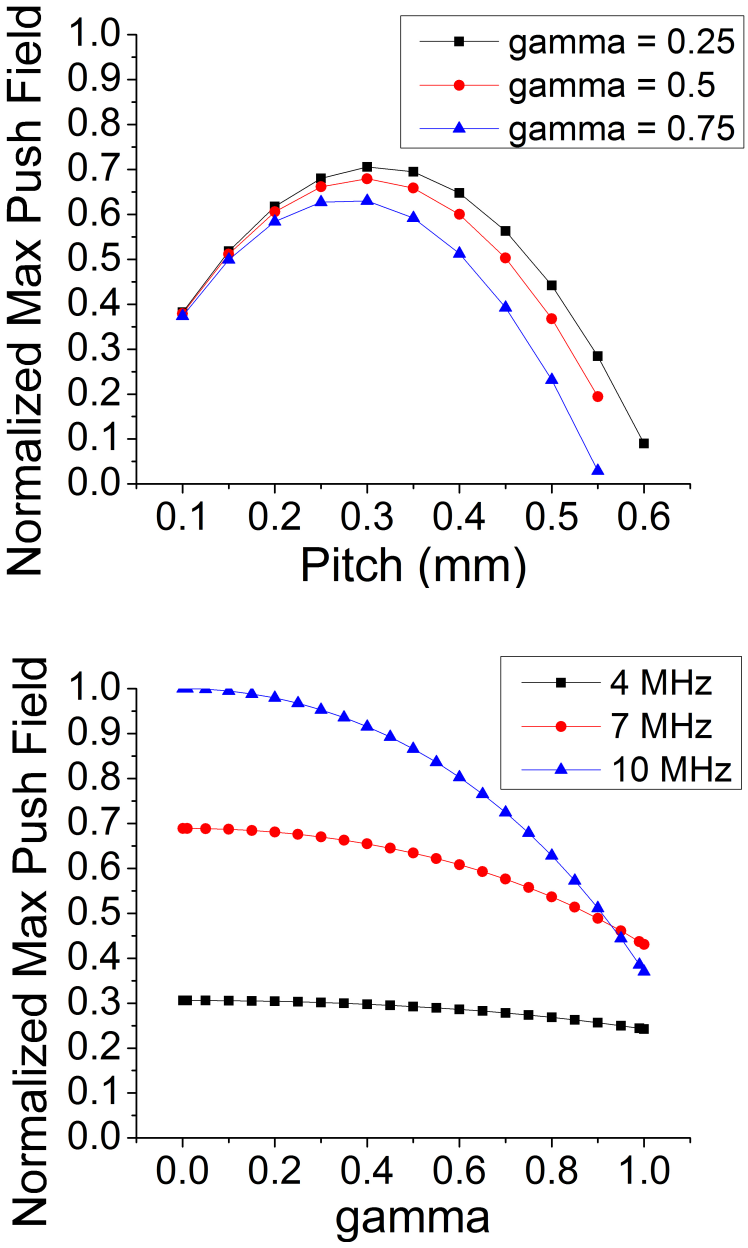

Figure 2.7: Comparison of the repelling force on a 23 u singly-charged ion for various values of carpet pitch, γ, and RF frequency. The maximum push field in Equation 2.8 is used as a measure of the repelling force. The units have been normalized to the value for pitch = 0.375 mm, $\gamma = 0.001$ at 10 MHz. A helium gas pressure of 100 mbar, temperature of 295 K, and a RF amplitude of 75 V were used in the calculations. Above: The effect of varying γ increases with the RF carpet pitch. A RF frequency of 7 MHz was chosen for this calculation due to 7 MHz being the approximate maximum repelling frequency for a = 0.5 mm (see Figure 2.5). Below: Varying γ is shown to effect the maximum repelling force significantly at high ($\sim$10 MHz) RF frequencies. For this calculation, a = 0.375 mm.

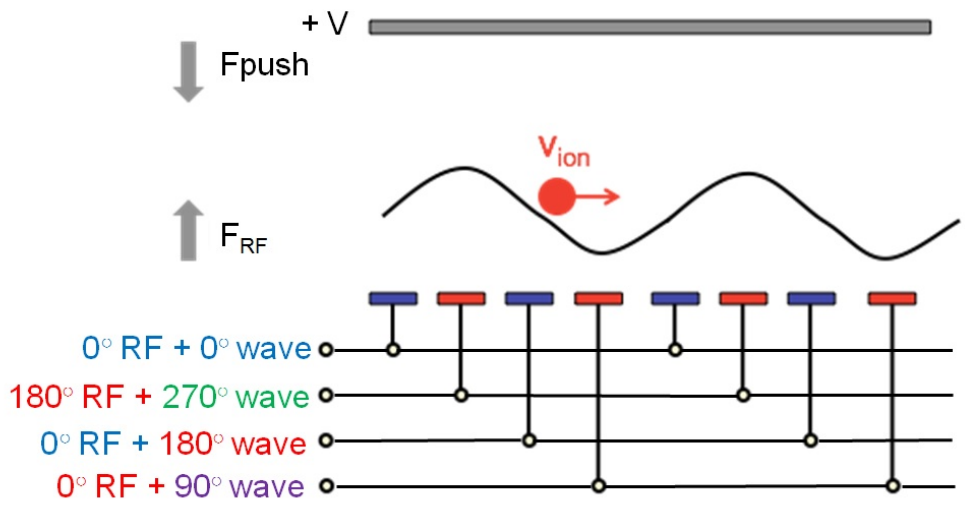

Figure 2.8: The RF and wave phases applied to the four sets of electrodes with the push field.

breakdown limit the maximum voltage that can be applied to a RF carpet in helium gas [5, 10]. The "ion surfing" method [5] derives its name from the traveling wave potential that is superimposed over the RF potential to transport the ions. The ions "catch" the wave and are transported to the extraction orfice in the minimum of this combined potential. All of the carpets tested in this work had a wavelength, λ, consisting of 4 electrodes ($\lambda = 4a$), with the wave signal on each electrode successively 90 degrees out of phase. A schematic, one-dimensional representation of the traveling wave electrode structure is shown in Figure 2.8. Figure 2.9 shows the total potential with the resulting traveling wave. The ions will be driven into the deep pockets formed by the overall potential and then be carried along by the traveling wave moving parallel to the carpet surface.

In general, the wave velocity is the product of the wavelength and frequency. In the present case, the wavelength of the traveling wave is determined by the electrode geometry and the frequency is a variable. The RF carpets used here were designed with wavelengths ($\lambda = 4a$) of 1.5 or 2 mm, and the wave frequencies ranged from 10 to 75 kHz, giving wave

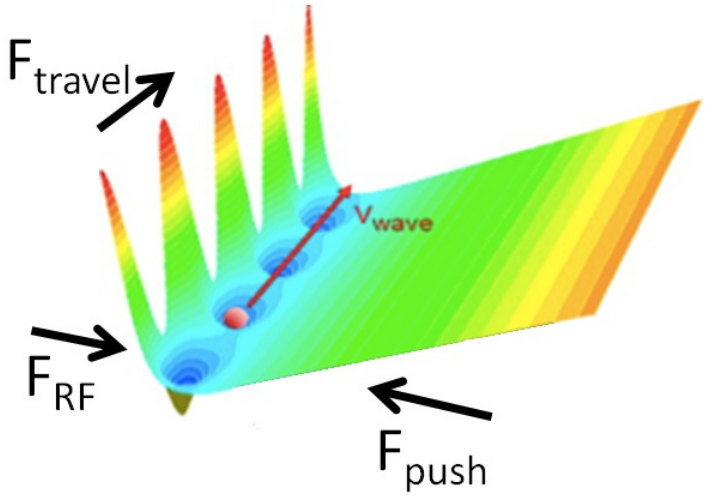

Figure 2.9: The combination of potentials required for ion transport via the "ion surfing" method. The RF-generated pseudo-potential creates the high barrier that prevents the ions from hitting the electrodes, and the push potential directs ions into the potential minimum. The pockets of the traveling wave potential are visible in the trough formed by the RF and push fields [5].

velocities in the range 15 to 150 m/s. Developing an RF carpet with a wavelength of 8 electrodes (with each electrode consecutively shifted 45 degrees in phase) was considered, but simulation results did not show a significant improvement in transport efficiency or velocity.

2.2 Features of Ion Surfing RF Carpets

A cartoon of an ion surfing RF carpet is shown in Figure 2.10. The carpet traces of each of the four wave phases are connected to a bus bar. The bus bars are copper strips at the edges of the carpet traces to which the RF and wave potentials shown in Figure 2.8 are applied. The wave phase 3 and 4 bus bars are located on the underside of the carpet, and vias through the carpet substrate connect the phase 3 and 4 carpet traces to the appropriate bus bar. The ions are transported to the collection pads, which are used to read the transported

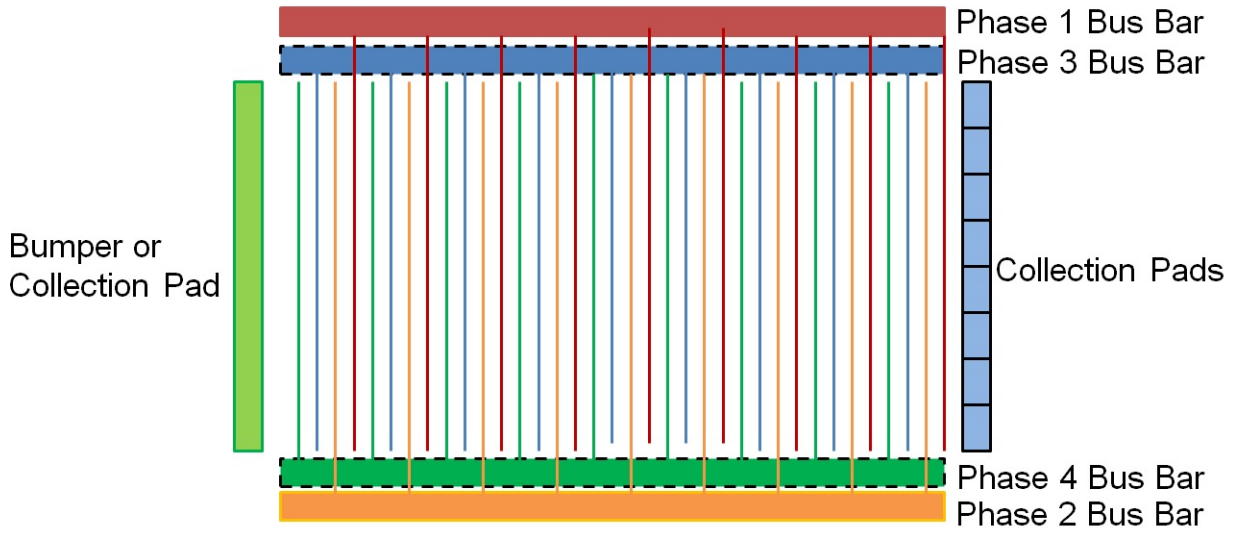

Figure 2.10: A cartoon drawing of an ion surfing RF carpet. The dashed lines around the phase 3 and 4 bus bars indicate that the bars are on the bottom layer of the carpet. Vias connect the ends of the phase 3 and 4 traces to the appropriate bus bars.

ion current. Thick copper strips near the edges of the carpet can be used as "bumpers" to contain ions near the carpet boundaries within the transport area above the carpet traces.

2.3 Transport Modes

Ions can be transported by the traveling wave in one of two modes: the so-called "locked" or "slipping" modes [5]. In locked mode, the ion velocity, v_{ion}, is equal to the wave velocity, v_{wave}. Ions stay within a single potential well of the traveling wave as they move along the carpet surface; they are "locked" in, $v_{ion} = v_{wave}$. In slipping mode, the ions do not stay within one traveling wave pocket. Instead, they repetitively slip out, get picked up by the next or a subsequent wave pocket, and then slip out of the traveling potential again. This mode results in $v_{ion} < v_{wave}$.

Simulated ion velocities from the initial code developed by Bollen for the first investigation of the ion surfing method are shown in Figure 2.11 [5]. The simulation model has perfect

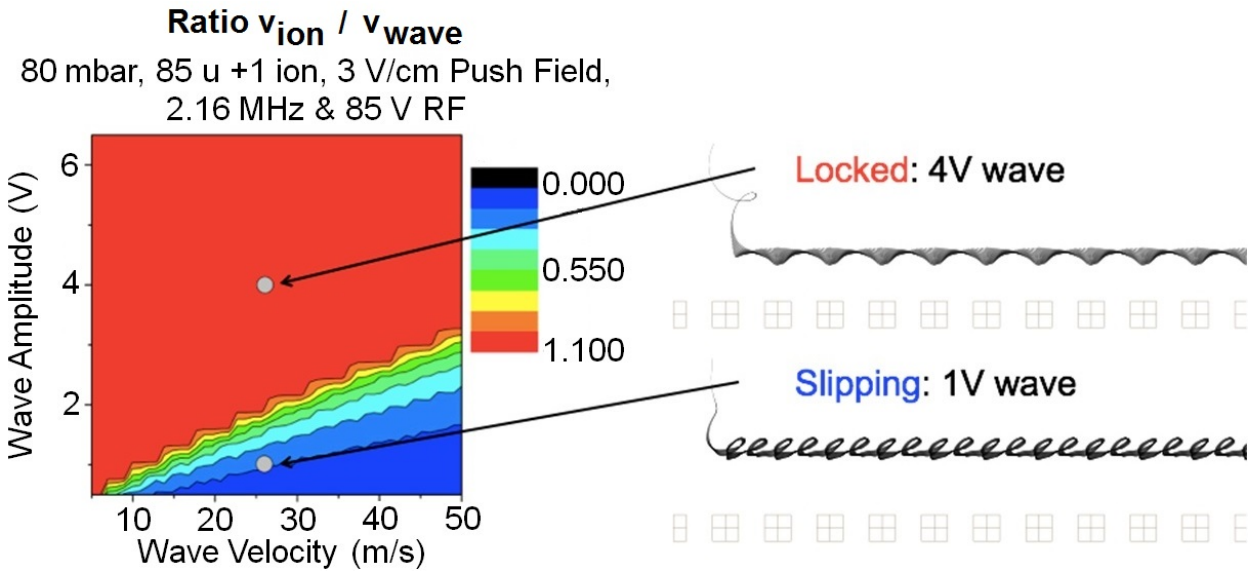

Figure 2.11: Left: The net ion velocity relative to the traveling wave velocity is shown as a function of the wave amplitude and wave velocity. Ions in the red region are traveling in the "locked" mode. The velocities were calculated with the IONSURF code [5]. Right: Examples of the "slipping" and "locked" mode ion trajectories are shown as black lines above the electrodes shown as brown squares.

potentials and the effect of the buffer gas on ion motion is described by simple Stokes or viscous damping. (Additional simulation examples and details are given in Chapter 3.) The general relationship between wave velocity and wave amplitude on the ion velocity is illustrated in the left panel of Figure 2.11. As the wave velocity increases, the wave amplitude required for the ions to achieve locked mode also increases. Results of simulations conducted using the electric field modeling software SimION [68] for two points in Figure 2.11 are shown on the right. In the lower part, the ions are in slipping mode, while in the upper part the ions are in locked mode. The simulated ion is seen to fall out of the traveling potential under the slipping mode conditions, and with the locked mode parameters the ion is transported forward with the same velocity as the wave. A goal of the RF carpet experiments is to validate the existence of these two modes of transport as a part of the overall goal of obtaining high efficiency and rapid extraction of ions.

2.4 Comparison of RF Carpet Transport Methods

RF carpet development was conducted previously at the NSCL as part of the thesis work of Pang [10]. The transport of rubidum ions using a DC gradient superimposed on the RF-generated repelling effective potential was investigated and the results are given in Ref. [10]. The use of the DC gradient is referred to as the "traditional" method of RF carpet transport due to the use of DC gradients to direct stopped ions to the exit region of all previous gas cells [1, 2, 3, 43, 44]. Implementing a DC field on top of the RF signal was found to be challenging due to the large overall bias needed to transport ions over large distances. The "ion surfing" method does not require a DC field, and it was proposed and investigated here as an alternative to the traditional method.

2.4.1 Advantages of Ion Surfing

Two inherent difficulties of ion transport with the traditional method are the large number of circuit components and the larger capacitance of a traditional method RF carpet as compared to an ion surfing carpet of identical size. First, a resistor chain is required to create the DC gradient. Small resistors are added to create a voltage divider, as shown for example in Figure 2.12, and the RF has to be capacitively coupled to each electrode. Second, traditional carpets often consist of two circuit board layers, which increases the capacitance of the system. The top layer electrodes supplied the DC field, and the electrodes are mirrored on the bottom layer to provide the RF field. In contrast, an ion surfing RF carpet requires only one layer.

The resonant RF frequency that can be applied to any RF carpet is determined by its capacitance, C, and inductance, L, as follows:

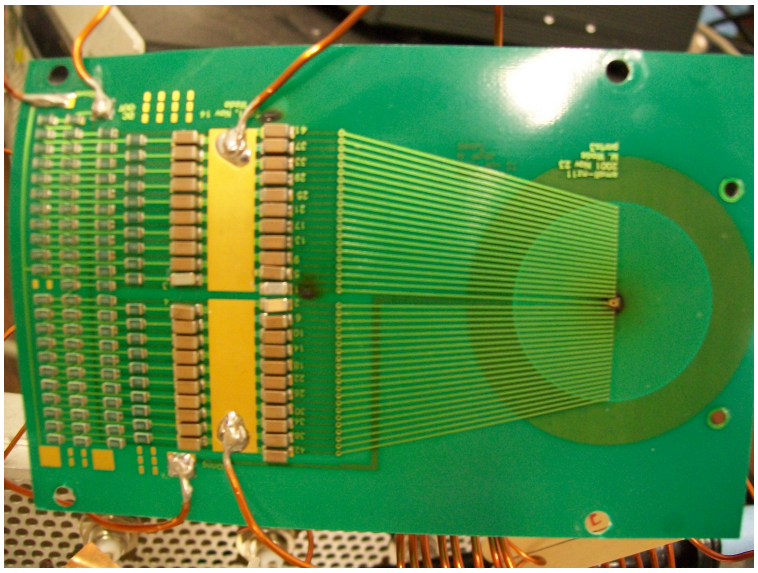

Figure 2.12: The bottom side of the small concentric circle carpet developed by Wada [3]. Small resistors were added by hand to create the potential gradient. The working electrodes are in the circular region to the right of the Figure on the opposite side of the circuit board, see also Figure 2.3 right.

$$\Omega = \frac{1}{\sqrt{LC}} \tag{2.9}$$

The addition of a second layer to traditional RF carpets increases the capacitance and reduces the resonant RF frequency for a given inductance. The large area carpets developed by Pang [10] needed to be sectioned to minimize the capacitance, with each section equipped with an individual RF circuit. In the ion surfing method, only one electrode layer is needed, and one RF signal can be applied to the entire (large) area carpet with one circuit. Examples of the relative complexity of the electronic circuits required for traditional and ion surfing methods of operation are shown in Figures 2.12 and 2.13.

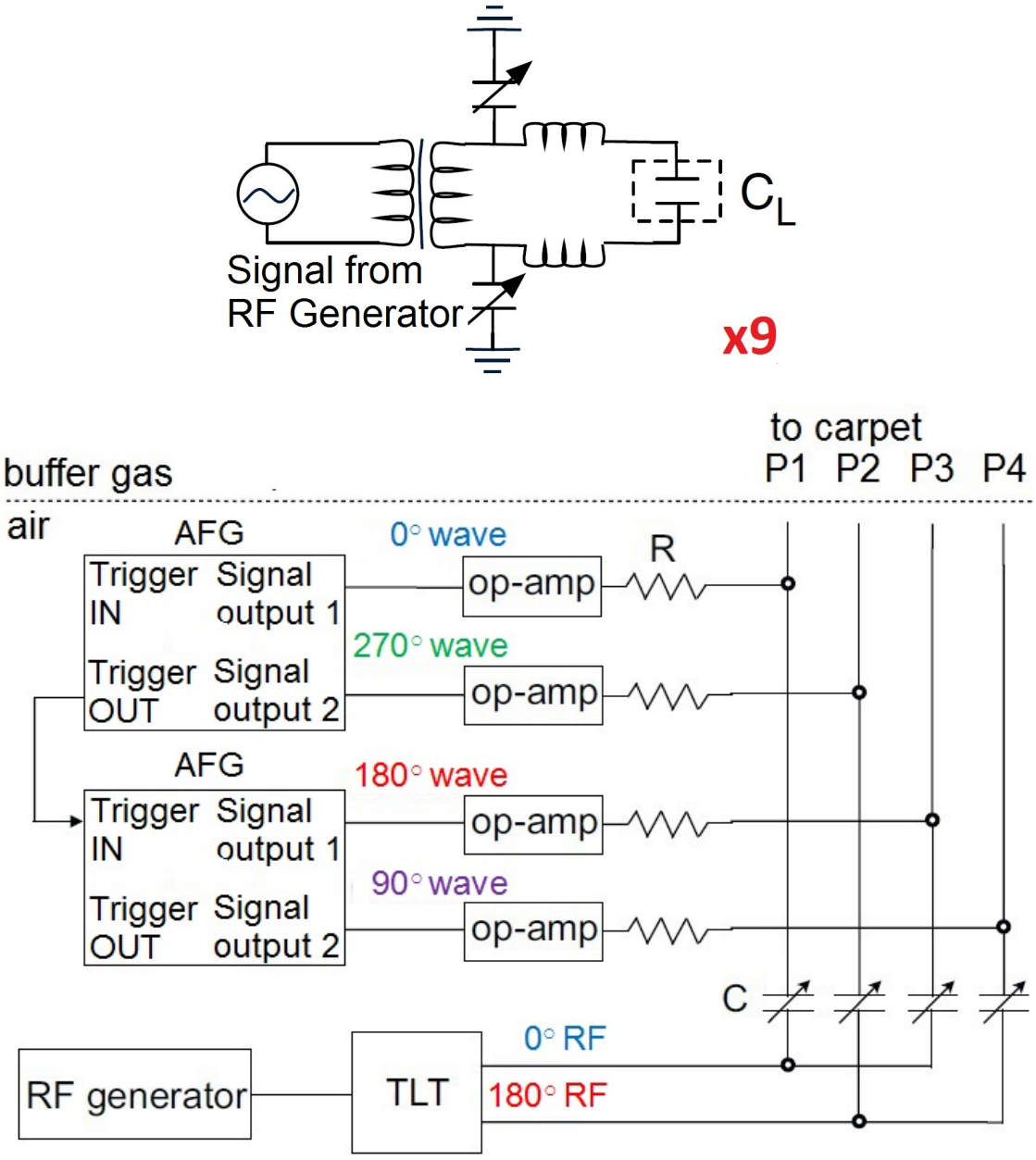

Figure 2.13: Above: A schematic of one part of the RF circuit created by Pang to drive a large area RF carpet [10]. C_L is the capacitive load of one of the 9 RF carpet sections. Each set of two variable capacitors was used to tune one section of the RF carpet. This circuit diagram does not include the resistor chain and DC signal. Component ranges: air-core inductors = 3 - 10 μH, variable capacitors = 15 - 150 pF, C_L = 0.7 - 10 nF Below: A schematic of the circuit used to provide the RF and traveling wave signals to a large area "ion surfing" RF carpet [12]. A transmission-line transformer (TLT) was used to match the impedances of the RF generator and the RF carpet. The RF signal was matched on each of the four wave phases by adjusting the variable capacitors. The resistors provided a buffer between the RF and the wave signals supplied by two arbitrary waveform generators (AFGs), and the operational amplifiers increased the wave amplitude. Component ranges: R = 2 - 10 kΩ, varaible capacitors 15 - 150 pF, C_L = 1 - 3 nF

2.4.2 Previous Transport Results of the DC Gradient Ion Transport Method

Rubidium ions were successfully transported with traditional RF carpets over distances up to 40 cm and at pressures from 53-146 mbar [10]. Additionally, transport efficiencies of greater than 80% and nearly 100% were achieved for pressures of up to 106 mbar and 80 mbar, respectively [10]. These results set the standard to which the ion surfing transport experimental and simulation results will be compared.

Chapter 3

Simulation of the Ion Surfing Method

Simulations of the ion surfing method were conducted using three different computer codes. Details of each simulation type are given in Section 3.1, as well as a comparison of the results of the three models. Section 3.2 introduces the wide parameter space and summarizes the expected (and later observed) effects of varying parameters on the performance of the carpet.

3.1 Details of the Simulation Models

A numerical code, IONSURF [5], was developed by Bollen for the initial investigation of the ion surfing method and used simplified analytical potentials. The commercial code SimION was later employed to simulate the potentials generated by a realistic RF carpet electrode system. Simulations at lower pressures ($p < 80$ mbar) and with the hard sphere collision model were also conducted within SimION; however, at higher pressures, the computation time increased substantially (for example, ∼10 minutes of computation time is necessary to simulate transporting a $^{85}Rb^{+}$ ion over a distance of 1 cm at 120 mbar pressure). For higher pressures, the IonCool code developed by Schwarz was utilized [69] due to its reduced

computation time (for example, the time needed to simulate transporting a $^{85}Rb^{+}$ ion over a distance of 1 cm at 120 mbar pressure is only ∼3 minutes). The IonCool code required the electric potentials determined using SimION to execute the simulation.

3.1.1 IONSURF: Simulations with Perfect Potentials

The IONSURF code numerically integrates an ion's equation of motion as it experiences the summed potentials of the ion surfing transport method using a Runge-Kutta algorithm [5]. The overall effective potential is given in Equation 3.1 - in that equation, the RF-generated effective potential and traveling wave potential decrease exponentially as the distance from the carpet surface increases.

$$V(x,y,t) = E_p \cdot y + V_{eff,max} \cdot e^{-2\pi\frac{y}{a}} + V_{wave} cos\left[\frac{2\pi}{\lambda}(v_{wave}t - x)\right] \cdot e^{-2\pi\frac{y}{\lambda}} \tag{3.1}$$

Recall that $\lambda = 4a$ in the present case so that

$$V(x,y,t) = E_p \cdot y + e^{-2\pi\frac{y}{a}}\left[V_{eff,max} + V_{wave} \cdot e^{-\frac{1}{4}} \cdot cos\frac{2\pi}{\lambda}(v_{wave}t - x)\right] \tag{3.2}$$

where a is the RF carpet pitch, E_p is the push field, V_{wave} is the amplitude of the traveling wave, λ is the wavelength, and v_{wave} is the traveling wave velocity. Equations 2.3 and 2.4, with the origin shifted by a/2 from mid-electrode to mid-gap (see Ref. [11]), are the analytic expressions used to compute the electic field for the $V_{eff,max}$ (see Section 2.1.1).

The effect of the buffer gas on ion motion is modeled as a viscous drag force:

$$\vec{F}_d = -D \cdot \vec{v} \tag{3.3}$$

where $\vec{F}_d$ is the drag force, $\vec{v}$ is the ion's undamped velocity, and D is the damping factor calculated by Equation 2.6. The use of a simple drag force describes the average behavior and is a computationally efficient alternative to using individual ion-atom collisions.

Using Equation 3.1 and the viscous drag force, the IONSURF code can be used to determine whether an ion will or will not be transported under the input conditions. If the ion can indeed be transported, the code can be used to calculate aspects of the ion's motion for a given set of operating conditions, including its velocity and minimum distance above the carpet. In the present work, the IONSURF code was a valuable tool for investigating the large experimental parameter space.

However, the perfect potentials of Equation 3.1 are not realized in RF carpet applications. For example, the traveling wave and RF potentials do not vary over the width of the electrode. The smooth, sinusoidal RF potential generated and used in the IONSURF simulations (black squares) compared to the potential calculated along an RF carpet surface by SimION (red circles) is shown in Figure 3.1. The flat-topped potentials generated by actual RF carpet electrodes are not accurately represented in the IONSURF code. Therefore, SimION was used to generate more realistic potentials for further simulations.

3.1.2 SimION Simulations

SimION is a commercial software program that simulates charged particle optics in a fixed mesh framework [68]. The effective potentials in the SimION simulations of the ion surfing method were calculated based on the RF carpet electrode and push plate geometry within the

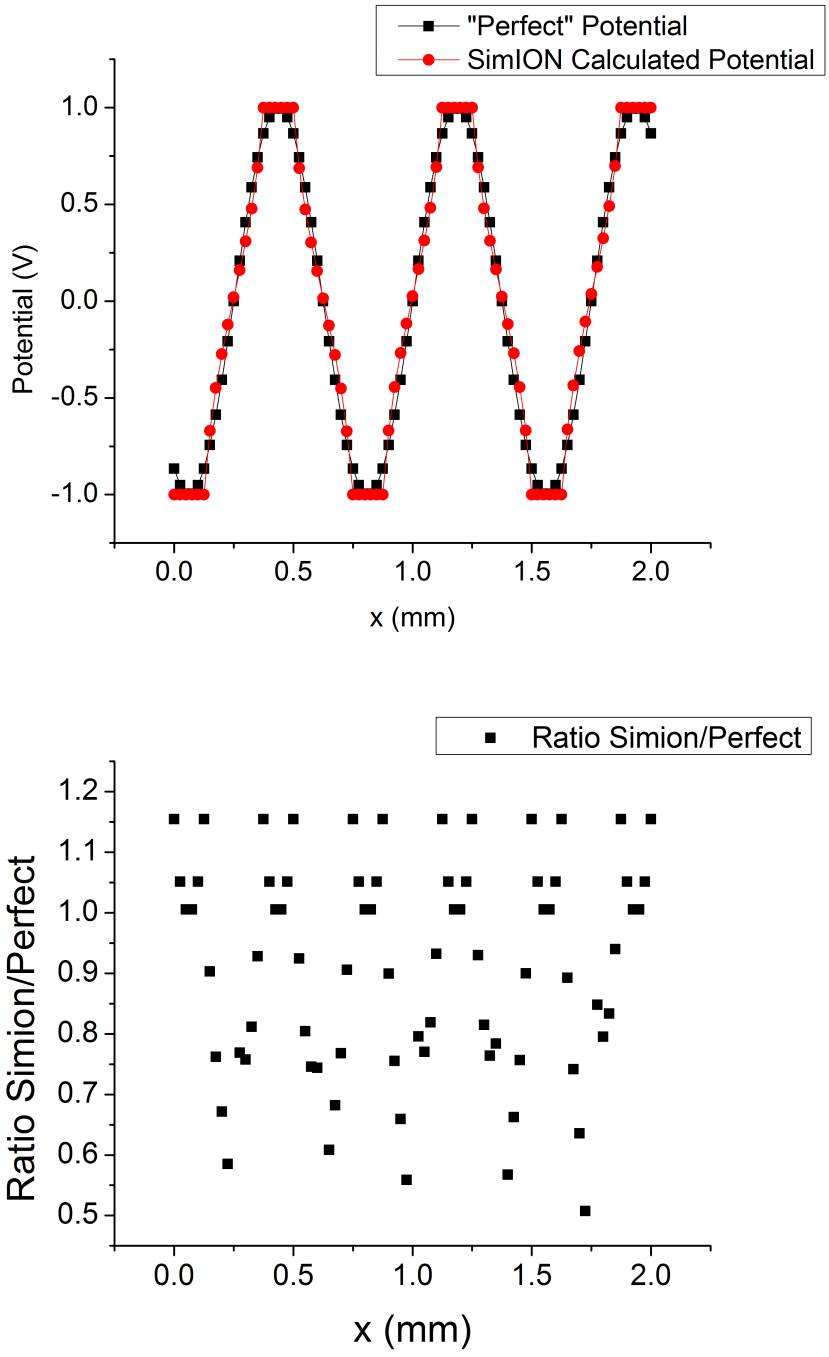

Figure 3.1: Above: A comparison of the RF potential used in the IONSURF code (black squares) to the potential along the carpet surface calculated from a RF carpet geometry by SimION (red circles). Lines have been added to guide the eye. The electrode width is 0.125 mm with a 0.25 mm gap. The potentials were calculated with an increment of 0.025 mm and maximum voltage of 1 V. Below: The ratio of the potential calculated in SimION to the "perfect" potential. Potentials up to 15% greater than the perfect potentials are present at the edges of the realistic carpet electrodes; conversely, the potentials in the gaps are smaller.

user-defined mesh. (See Appendix A for details concerning the grid unit size and trajectory quality.) User-supplied programming within SimION provided added functionality, including the application of time-dependent potentials to the electrodes and modification of the ion's motion to simulate the presence of buffer gas. The presence of the buffer gas was accounted for by either simple viscous damping or a hard sphere (HS) collision model. The optional HS collision model was included as part of the SimION package. The results from two different methods for incorporating the damping effect of the gas are discussed in the next section.

Due to the statistical nature of calculating the ion-buffer gas collisions, the HS model is expected to provide a more realistic approximation of the ions' motion through the gas, and to give a more accurate description of ion transport. However, as the pressure of the buffer gas increases, the number of collisions encountered by an ion as it travels through the buffer gas also increases, with an accompanying increase in computational time.

3.1.3 Surf2D Simulations

The IonCool code [69] was developed by Schwarz for the modeling of ion behavior in coolers and bunchers. Such devices are used, for example, to prepare ions for precision mass measurements [27]. A modified version of the code, Surf2D, was developed by Schwarz to model ion surfing. The code makes use of the more realistic electric potentials calculated with SimION. The time-dependent fields are programmed within the code, as are the ion-buffer gas collisions, as outlined in [69]. Surf2D simulations were computationally more efficient; and typical simulation times were reduced by $> 50\%$ over similar SimION simulations. The increased computational speed enabled the quick performance simulations without the results suffering in quality, as demonstrated in the following section and, later, in comparison

to experimental results.

3.1.4 Comparison of the Simulation Methods

Four sets of simulations were conducted with identical input parameters to compare the simulation methods described above. Two of the simulations were performed with the viscous drag models (IONSURF and SimION with viscous damping), and the other two were executed with the HS collision models (SimION HS and Surf2D). The selected input parameters matched those of an early experiment with the first ion surfing RF carpet prototype (0.5 mm pitch, 0.5 γ, 1.55 MHz RF frequency, 90.4 V RF amplitude, 26 m/s wave velocity, 40 mbar helium buffer gas pressure, Rb^+ ions). The calculated ion velocity as a function of wave amplitude for each of the four simulations is shown in Figure 3.2. Each model gives the same overall trend in ion velocity. Note that the HS simulation results have error bars due to the statistical nature of the ion-buffer gas collisions. All of the simulations indicate that the ions will reach the traveling wave velocity, or locked mode, of 26 m/s at wave amplitudes above 2.5 V. The simulations using the HS collision model predict that slightly higher traveling wave amplitudes are necessary in order to achieve the same ion velocity as compared to results based on the viscous damping models.

3.2 Simulation Results Across Ion Surfing Parameter Space

Due to the computational speed of the IONSURF method, it was used to explore the wide parameter space for the prototype RF carpet with the fixed pitch $a = 0.5$ mm and $\gamma = 0.5$.

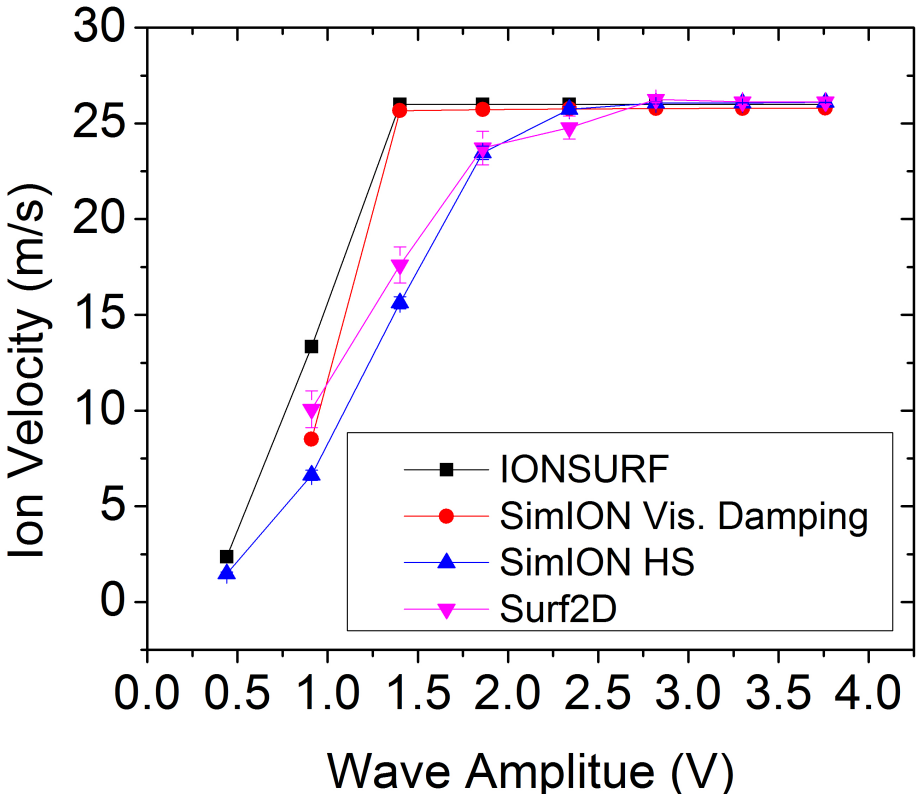

Figure 3.2: A comparison of the various simulation models for a $^{85}Rb^{+}$ traveling through 40 mbar of helium buffer gas. The remaining parameters used in the calculation are as follows: 10 V/cm push field, 1.55 MHz RF frequency, 90.4 V RF amplitude, 26 m/s (13 kHz) traveling wave velocity, 0.5 mm pitch, 0.5 γ. All the models generate the same trends in predicted ion velocity, with the hard sphere models requiring higher wave amplitudes in order to reach locked mode.

The prototype carpet had a larger pitch and smaller γ compared to the other carpets studied in this work. A sample of the simulation results is given in the following sections. In order to construct each plot with the IONSURF code, a 51 x 51 matrix was computed (that is, 51 evenly incremented values spanning the range of a given parameter were input into the calculation). A summary of the effects of varying each parameter is presented in Table 3.1 at the end of the section.

3.2.1 Traveling Wave Potential Frequency and Amplitude

The effect on the ion velocity with variation of both the wave velocity and amplitude is illustrated in Figure 3.3 (above). The amplitude necessary to achieve locked mode for a given wave velocity is apparent. The boundary between the linearly rising ion velocity with wave velocity in the top left half of Figure 3.3 (above) and the accelerating ion velocity with wave amplitude of the lower right half of Figure 3.3 (above) demarks this transitional amplitude between slipping and locked modes. As the wave velocity rises, the rate of the increase in ion velocity as the wave amplitude becomes greater also increases, which is shown by the decreasing space between the contour lines along the right edge. This relationship between wave velocity and wave amplitude is critical: to attain high wave velocities, high wave amplitudes are necessary.

There is a drawback to simply increasing the amplitude of the traveling wave. The reduction in the ions' distance above the RF carpet electrodes as the wave amplitude increases is shown in Figure 3.3 (below, another view of the data from the same calculations as the top part of the figure). Ions moving closer to the carpet surface are more likely to collide with an electrode and be lost. The IONSURF code does not account for individual ion-buffer

gas collisions that might direct the ions onto the carpet surface. The SimION and Surf2D simulation results that include HS collisions predict a general decrease in ion transport efficiency as the wave amplitude increases. Ergo, the maximum obtainable ion velocities will come at the cost of greater ion losses. The important trade-off between ion transport velocity and efficiency was closely examined in experimental tests of the ion surfing method.

3.2.2 RF Frequency and Amplitude

Ion velocity as a function of the RF variables and wave amplitude is shown in Figure 3.4. Due to its large impact on obtaining locked mode ion velocity and on the ion transport efficiency, the wave amplitude will be kept on the ordinate in the remaining figures of this chapter. Higher wave amplitudes are required to obtain locked mode (red region in all the remaining figures in this chapter) as the RF frequency is increased from 1 to 3 MHz, as shown in Figure 3.4 (above). The repelling force generated as a function of RF frequency was given in Equation 2.8 and shown to increase over this RF frequency range of 1-3 MHz (cf. Figure 2.5 above, red line). The increase in repelling potential moves the ions farther from the carpet surface, increasing the ion transport efficiency. (The RF frequency was found to be an important parameter; increasing the RF frequency greatly improved the ion efficiency for the experimental results.) However, a higher repelling force can cause a more shallow potential minimum, which necessitates a larger wave amplitude to hold the ions within a traveling potential pocket.

Increasing the RF amplitude has an effect on ion velocity similar to increasing the RF frequency as shown Figure 3.4 (below). Increasing the RF amplitude also results in a greater repelling force since the RF frequency, V, is in the denominator of the subtractive term in

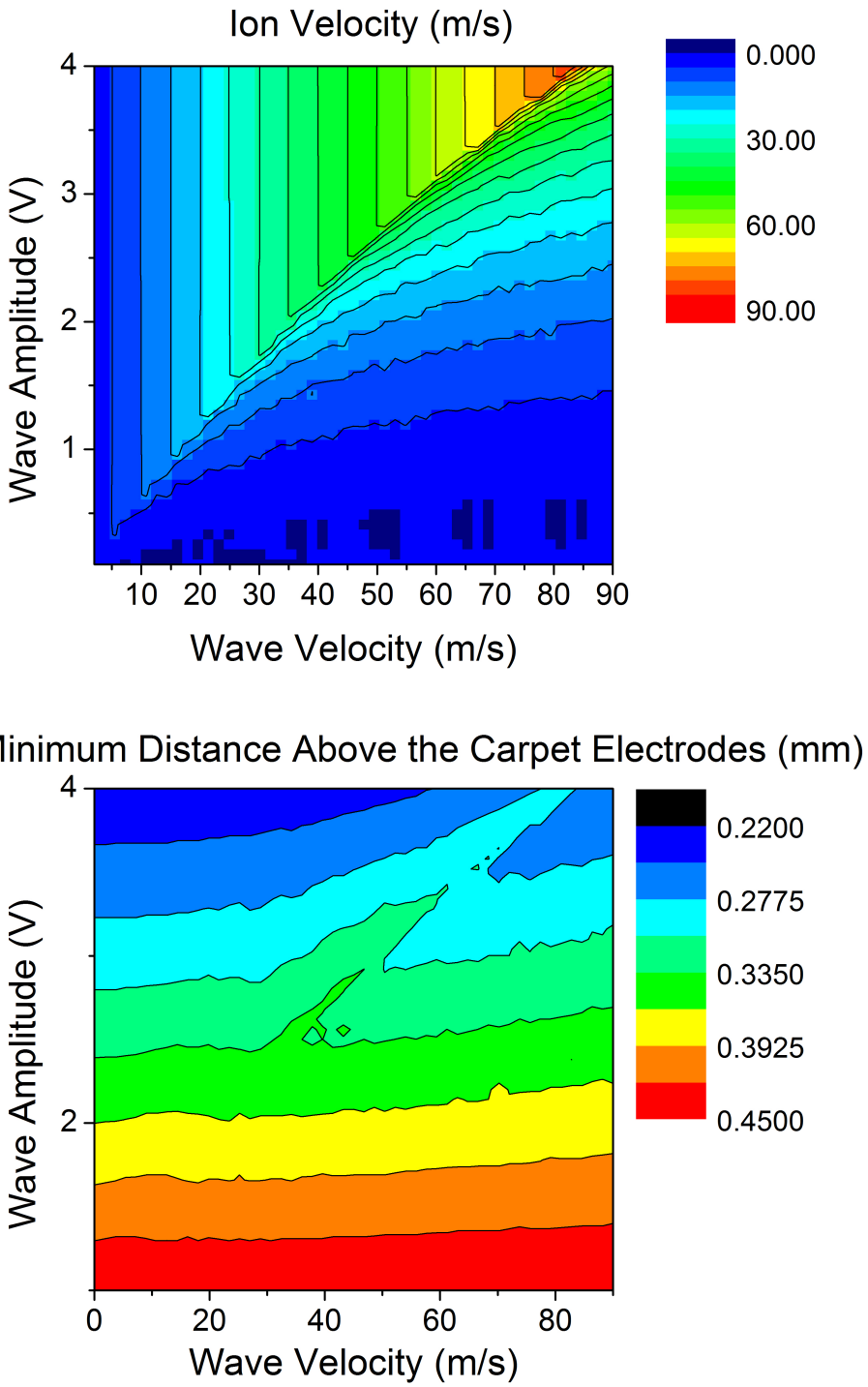

Figure 3.3: Above: A sample simulation result of the effect of wave amplitude and wave velocity on the ion velocity generated with the IONSURF code [5]. The parameters chosen are typical experimental values, listed as follows: $^{85}Rb^{+}$ ions, 80 mbar, 10 V/cm push field, 1.55 MHz RF, 93 V_{RF}. Below: The calculated minimum distance of the ions above the RF carpet electrodes for the same experimental parameters.

Equation 2.8. Again, a higher RF amplitude will push the ions farther from the RF carpet surface, so a larger wave amplitude is needed to contain the ions in the traveling potential well and to reach locked mode transport velocity, but the greater ion-to-carpet distance will yield a better efficiency.

3.2.3 Mass, Pressure, and Push Field

Similar to increasing the RF amplitude, an increase in the mass of the traveling ion requires a greater wave amplitude to achieve locked mode ion velocities. The proportional relationship between mass and repelling force is given in Equation 2.8, and the results from the simulations are shown in Figure 3.5. Since lighter ions are not as effectively repelled, they move at smaller average distances from the carpet surface and are correspondingly held more tightly in the larger traveling wave potential near the surface than heavier ions. But again, lighter ions are also more likely to be lost on the carpet electrodes. Lighter ions also experience a higher acceleration of the ion velocity with increasing wave amplitude.

Increasing the buffer gas pressure reduces the ion velocity, as shown in Figures 3.5 and 3.6, with a corresponding reduction in transport efficiency. The two pressures chosen for these simulations, 80 and 120 mbar, represent the upper and lower limits of the cyclotron gas stopper operating conditions. The additional ion losses and reduction in ion velocity can again be explained by Equation 2.8, where the maximum repelling field decreases as the pressure rises. The additional buffer gas atoms per unit volume cause a larger number of ion-buffer gas collisions (or a higher viscous drag force), increasing the probability of a collision diverting a traveling ion into a carpet electrode and hindering ion motion. Greater wave amplitudes are needed to contain the ions within the traveling potential due to the

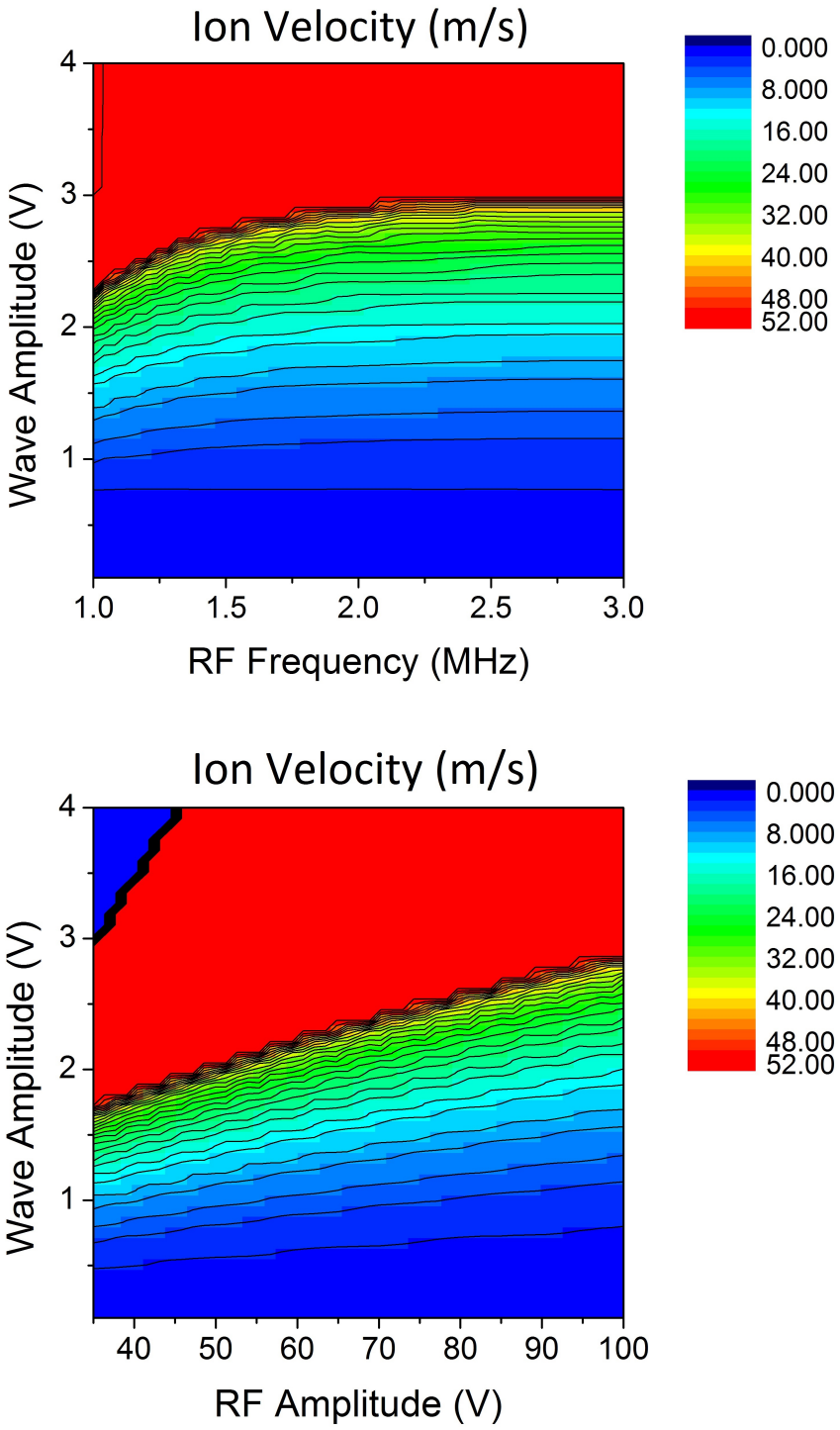

Figure 3.4: Selected simulation results of the effect of wave amplitude as a function of the RF parameters on the ion velocity generated with the IONSURF code [5]. The parameters chosen are typical experimental values, listed as follows: $^{85}Rb^{+}$ ions, 80 mbar, 10 V/cm push field, 52 m/s traveling wave. Above: Contours of ion velocity as a fuction of wave amplitude and RF frequency. The RF amplitude is 93 V. Below: Similarly, ion velocity as a function of wave amplitude and RF amplitude. The RF frequency is 1.55 MHz.

additional collisions, resulting in higher ion velocities as shown by comparing the simulation results in Figures 3.5 and 3.6.

Lastly, varying the push field results in the same overall trends as altering the wave amplitude. Increasing the push field helps to confine the ions in the traveling wave potential and leads to an increase in ion velocity, as shown in Figure 3.6 at the upper and lower operating pressures assumed for the cyclotron gas stopper. But there is a limit to the maximum push field thermal ions can withstand before the RF-generated repelling potential is overcome and the ions are forced onto the carpet surface.

3.3 Summary

A summary of the qualitative behavior of the ion motion as a function of ion surfing operating parameters is given in Table 3.1. The effect on ion transport efficiency and velocity is given under the condition of an increase in each of the seven operating parameters discussed in the previous section. The results from a number of experimental measurements of these variations are given in the next chapters. In general, good agreement was found with the general trends predicted from the simulations.

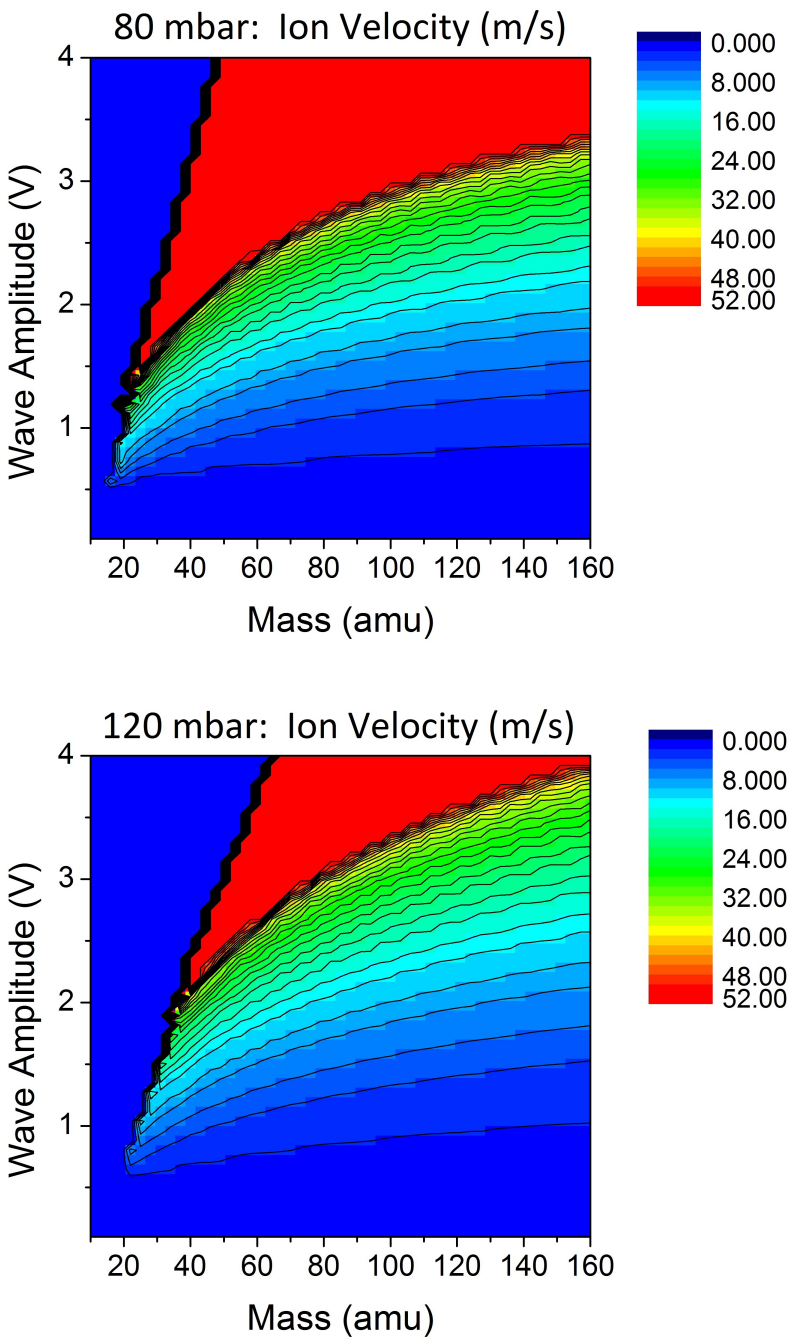

Figure 3.5: IONSURF simulation results of the effect of wave amplitude as a function of the singly-charged ion mass on the ion velocity for two buffer gas pressures [5]. The parameters chosen are typical experimental values, listed as follows: 10 V/cm push field, 1.55 MHz RF, 93 V_{RF}, 52 m/s traveling wave. 80 and 120 mbar pressure were selected to match the upper and lower limits of the cyclotron gas stopper operating conditions. Above: As ion mass increases, a higher wave amplitude is required to obtain locked mode (red region) ion velocities. Below: The increase in pressure also necessitates a higher wave amplitude for the ions to reach locked mode velocities.

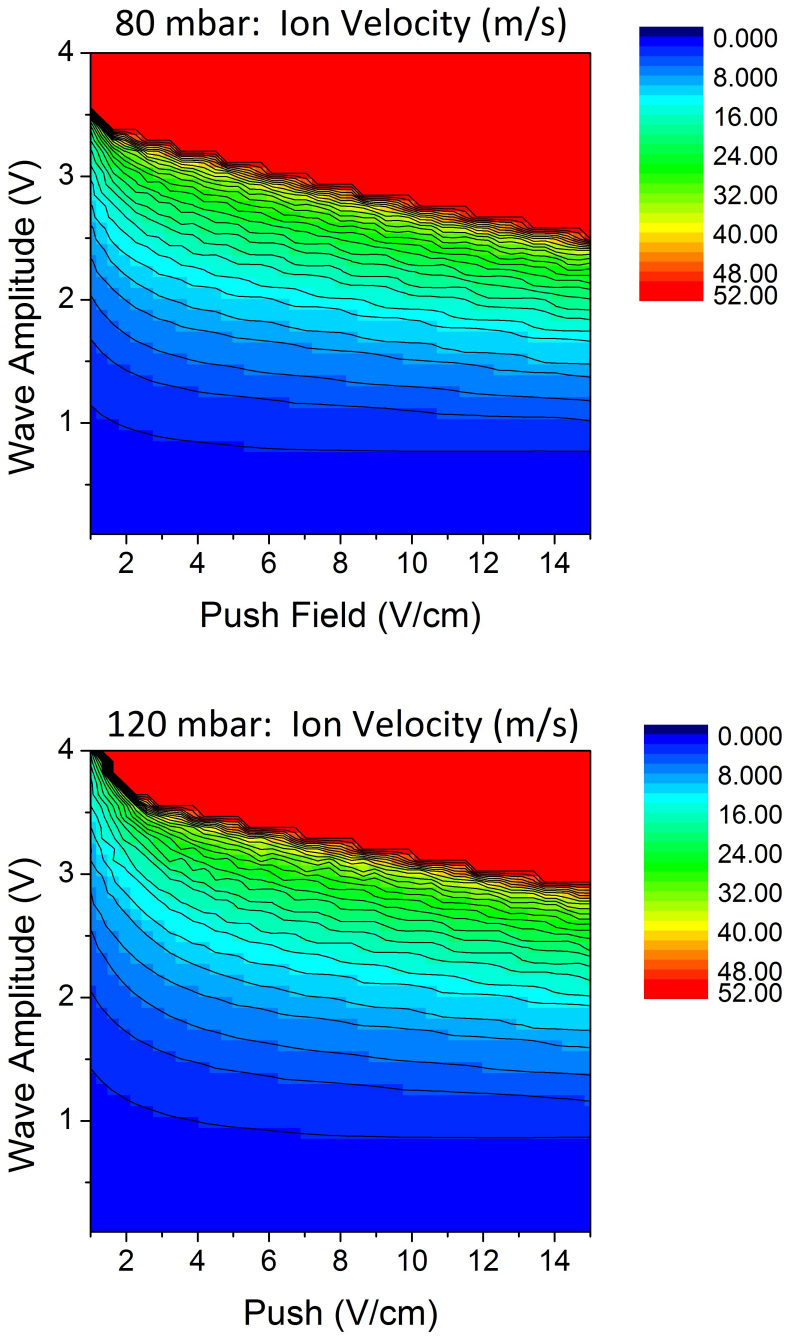

Figure 3.6: IONSURF simulation results of the effect of wave amplitude as a function of the push field on the ion velocity for two buffer gas pressures [5]. The parameters chosen are typical experimental values, listed as follows: $^{85}Rb^{+}$ ions, 1.55 MHz RF, 93 V_{RF}, 52 m/s traveling wave. 80 and 120 mbar pressure were selected to match the upper and lower limits of the cyclotron gas stopper operating conditions. Above: As the push field gains strength, a lower wave amplitude is required to achieve locked mode (red region) ion velocities. Below: The increase in pressure also necessitates a higher wave amplitude for the ions to attain locked mode velocities.

Table 3.1: Summary of the effect on ion velocity and transport efficiency as each parameter is increased, see the text. F_{RF} is measured by the maximum sustainable push field, see Equation 2.8.

Parameter	Effect on Transport Efficiency	Effect on Ion Velocity
Wave Velocity	Increase (slight)	Increase
Wave Amplitude	Decrease	Increase
RF Frequency (F_{RF} Increase)	Increase	Decrease
RF Frequency (F_{RF} Decrease)	Decrease	Increase
RF Amplitude	Increase	Decrease
Mass	Increase	Decrease
Pressure	Decrease	Decrease
Push Field	Decrease	Increase

Chapter 4

Measurement Procedures and Initial Work

Many measurements with various RF carpets were carried out during the course of this work. Section 4.1 describes the test set-up and equipment used for these measurements, and Section 4.2 outlines the procedures for the transport efficiency and velocity measurements. The design of the first RF carpet prototypes used to study the ion surfing method and selected experimental results from the studies are presented in Section 4.3.

4.1 RF Carpet Infrastructure

A test chamber was constructed for the previous RF carpet development work in order to conduct experiments under buffer gas conditions [10]. A RF circuit was designed and built for implementing the ion surfing method to RF carpets. The following subsections provide details about the essential experimental components of this work.

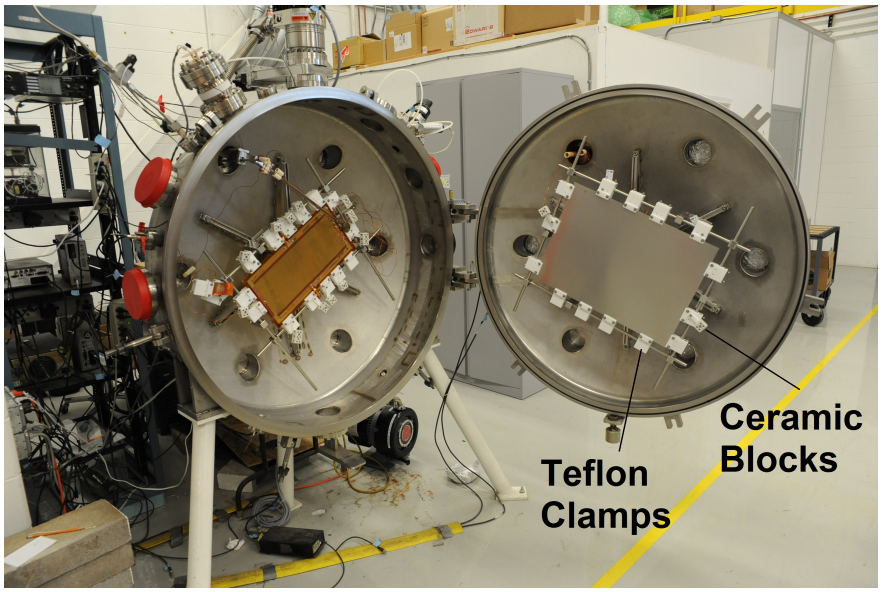

Figure 4.1: Photograph of the RF carpet test stand in the open position. A RF carpet is mounted in the adjustable frame on the left side of the chamber. A stainless steel plate, used to apply the push field, is opposite the RF carpet on the chamber door. The turbo pump is attached to the topmost opening, and the mechanical roughing pump is pictured to the lower right of the chamber. A pipe in the upper left corner connects to an ultrapure helium bottle (not pictured).

4.1.1 Test Chamber

The RF carpet test chamber shown in Figure 4.1 was developed by Bollen, Campbell, and Pang [10] for testing RF carpets planned for the cyclotron gas stopper. The chamber is 1.2 m in diameter and 45 cm wide. The geometry was selected to model the central region of the gas chamber of the cyclotron gas stopper. The many conflat flanges around the circumference of the chamber and on both the door and back wall provide viewports and feedthroughs. A Leybold turbomolecular pump (model TW290H or TW300W, both with 300 L/s pumping speed) with a mechanical scroll roughing pump was used to achieve a vacuum in the chamber of order 10^{-7} mbar. Due to the wide range of gas pressures expected in the chamber, several different vacuum gauges are needed to obtain accurate pressure readings. These gauges and their locations are listed in Ref [10]. The buffer gas used in all measurements for this

work was ultrapure helium gas (99.999% purity) purchased from Airgas. Additional physical features of the system are shown in Figure 4.1.

The RF carpets were mounted in the chamber on an adjustable frame. The flexible size of the frame allowed carpets of various dimensions to be successfully mounted in the chamber for testing. The white Teflon clamps and off-white ceramic blocks of the mounting frame are indicated in Figure 4.1. The blocks used to clamp the carpet into the frame are made of the insulating material Teflon to mitigate possible carpet-to-frame discharges. The frame is removable from the chamber, which allows easy installation of the RF carpets. The frame was placed on a flat surface, and the carpet was laid on the frame for easy mounting. The carpet surface would become slightly wrinkled in some areas during the mounting process, but the rise and fall of the carpet surface due to the wrinkles was large ($>$ 1mm) compared to the scale of the carpet traces ($<$ 1 mm). Thus, the ion motion is expected to be able to follow the slight slope of the carpet surface over a wrinkle. The ceramic terminal blocks were used to connect the wires from the carpet electrodes to the wires from the chamber feedthroughs. The connections from the carpet to the frame were electrically tested for continuity before the carpet was placed in the chamber, and the connections directly on the carpet did not have to be disconnected to remove the carpet from the chamber.

Rubidium and potassium ions from alkali aluminosilicate ion sources purchased from HeatWave Labs, Inc. [15] were used in the transport experiments. More information about the ion sources, including operation and verification of composition is provided in Appendix B. In Figure 4.2 is given a drawing of the cross section of the ion source (left) and a picture of the ion source and lens (right). The source (center) is enclosed within the lens, which has a diameter of 3.8 cm and provides focusing for the emitted ion beam. The visible side of the

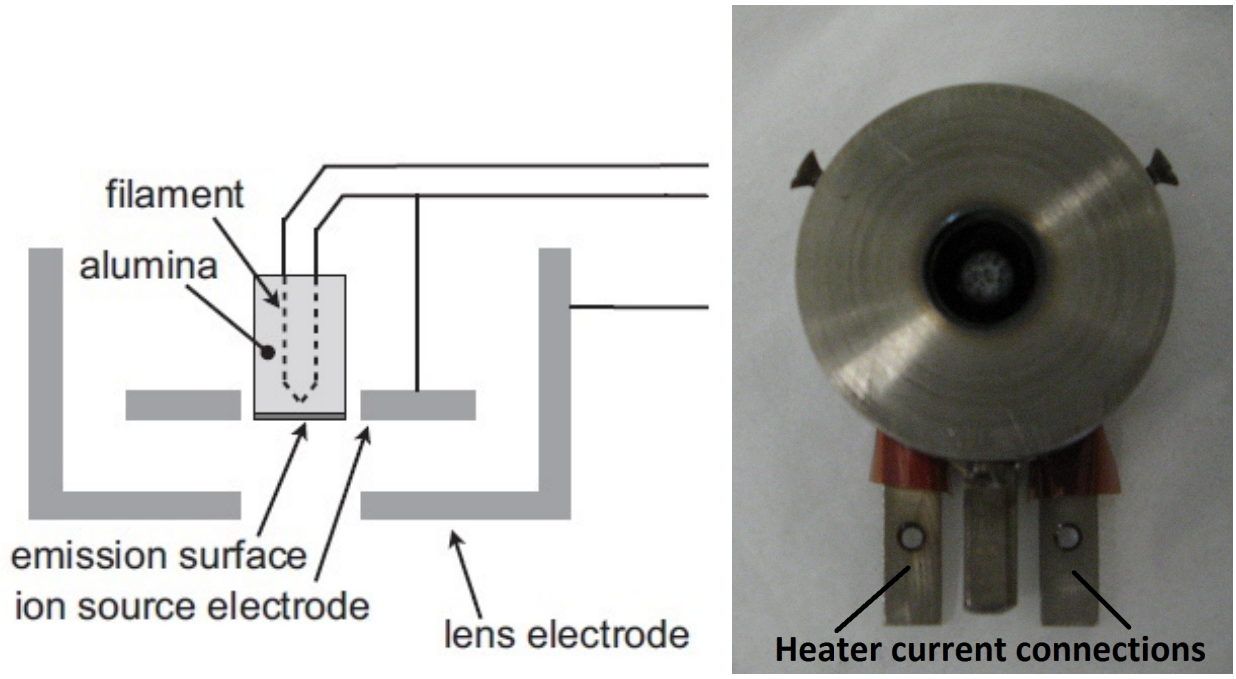

Figure 4.2: Left: Schematic of the cross section of the ion source and lens. Right: The ion source (center) within the focusing lens. The lens is 3.8 cm in diameter.

lens and source faces the carpet with a separation distance of ∼4.5 cm. Three connections extend from the circular lens; the two with holes and insulation indicated in Figure 4.2 (right) are used to deliver the heater current to the source. The central connection attaches to the end of an actuator arm. A schematic electronic diagram of the circuits used to apply bias voltages to both the lens and the ion source and the heater current to the ion source is shown in Figure 4.3.

The location of the ion source above the RF carpet must be known to deduce the fraction of ions transported as well as the ion velocity. The ion source is moved to different positions over the carpet using a radial actuator arm that can be operated from the outside of the chamber. The path of the source was a circular arc that had to be measured relative to the carpet in order to deduce the transport observables as a function of distance along the carpet. For all of the linear geometry carpet prototypes, pictures of the ion source were

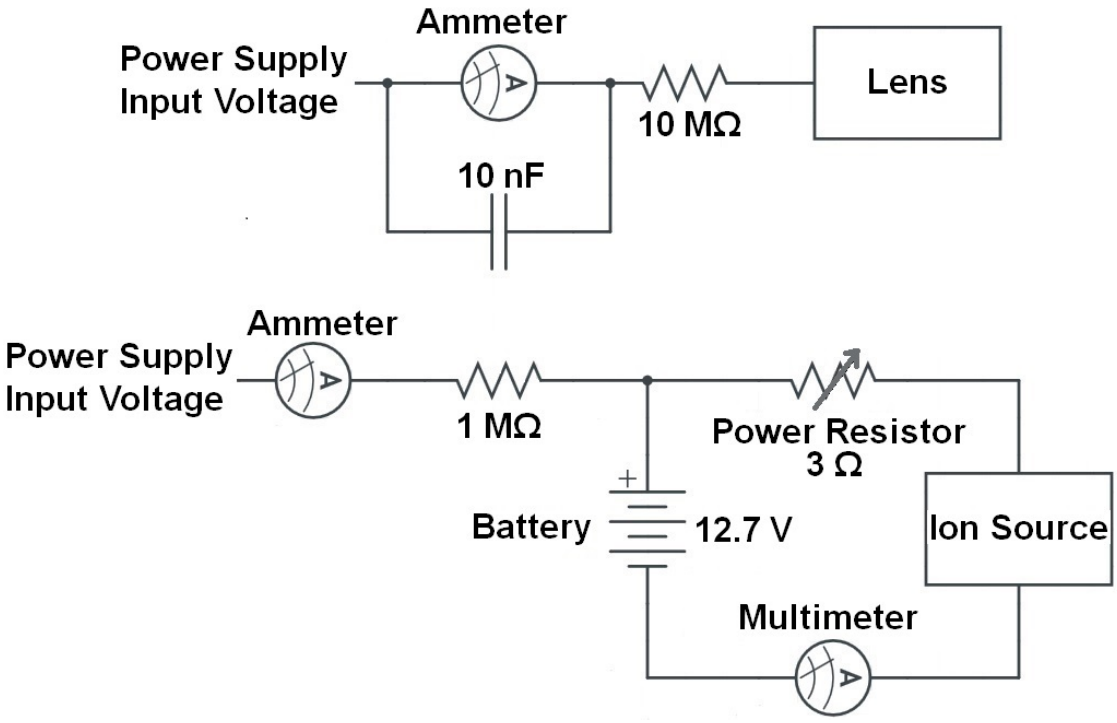

Figure 4.3: Top: Diagram of the circuit used to apply a bias voltage to the lens and to read the current collected on it. Bottom: Schematic of the circuit used to provide a heater current ($\sim$3 A) and bias voltage to the ion source.

taken at various locations over the carpet. The actuator arm has a linear position indicator, and the position number for each location was recorded along with the photograph image of the source. ImageJ software [70] was used to calculate the position of the ion source relative to the collection pads at the edge of the carpet from the photographs based on the ratio of the distance per pixel determined from carpet features of known size.

4.1.2 RF Circuitry and Electronics

A simple circuit was used to apply the traveling wave and RF signals to the RF carpets. A schematic of the circuit, which was used for the linear and circular prototypes presented in Chapters 5 and 6, is depicted in Figure 4.4. The circuit had a Q factor of $\sim$40. For the first two RF carpet prototypes, discussed below in Section 4.3, the variable capacitors and transmission-line transformer (TLT) [13] were not included. All RF carpets tested in this work had four traveling wave phases. For the initial prototypes, the RF signals on the four phases were phase and amplitude matched by adding fixed capacitors instead of the variable capacitors, and a simple ferrite core transformer was used instead of a TLT. The ferrite core transformer was replaced by the TLT in later tests to reduce the RF power lost to heat in the core. The RF carpets were driven at higher frequencies with the TLT and variable capacitors, and the increase in RF frequency (from $\sim$2 MHz to $>$ 6 MHz and as high as 8.5 MHz) was an essential improvement that led to increased ion transport efficiencies.

The replacement of the fixed-value capacitors with the variable capacitors reduced the difficulty of tuning the RF phases. This tuning, in turn, reduced the mismatch of the RF amplitudes. The RF signals on the oscilloscope for an excellent tune, with less than 2% mismatch of the RF amplitudes, of the linear prototype carpet (see Chapter 5) is shown in

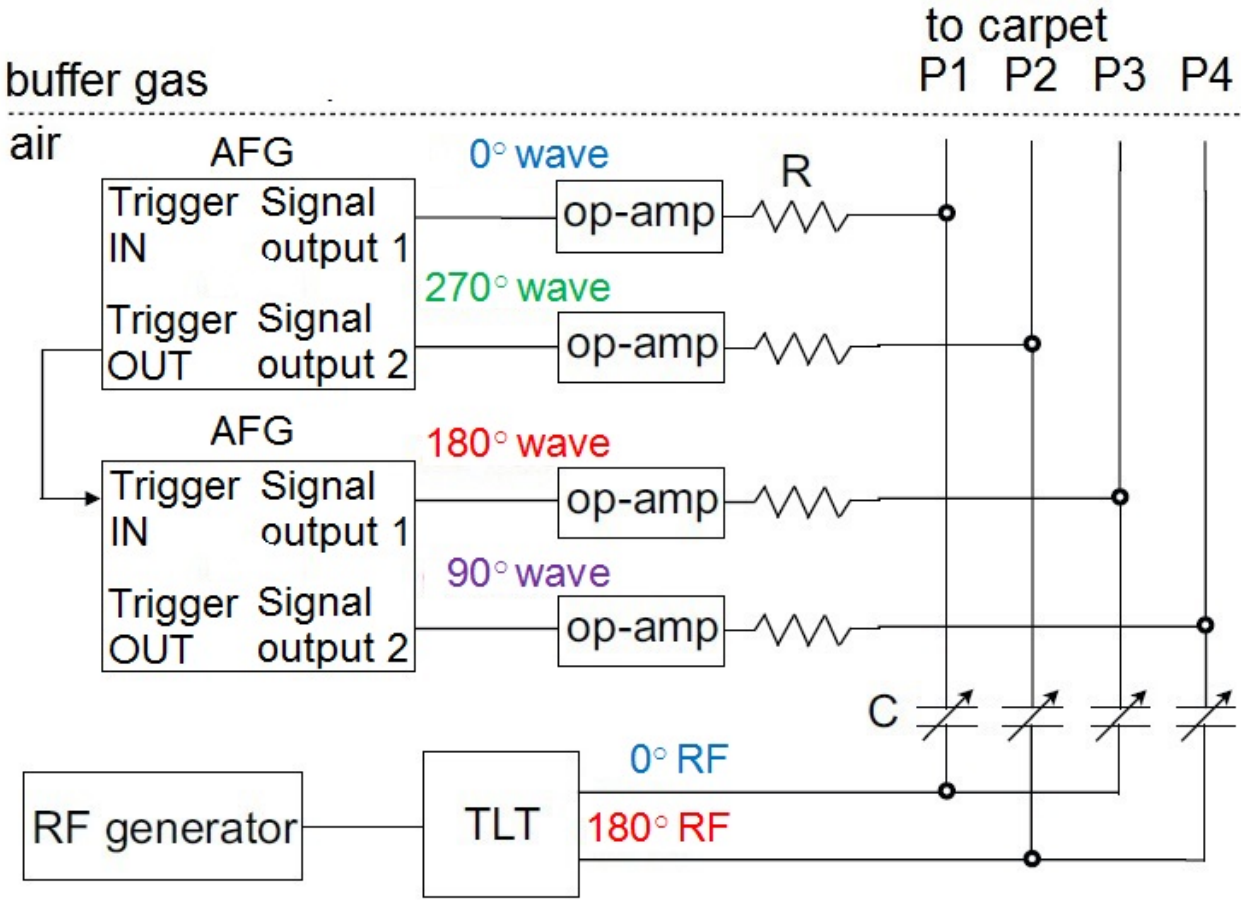

Figure 4.4: A schematic diagram of the circuit used to provide the RF and traveling wave signals to a RF carpet [12]. A transmission-line transformer (TLT) [13] was used to match the impedances of the RF generator and the RF carpet. The RF signal was matched on each of the four wave phases by adjusting a variable capacitor. The resistors provided a buffer between the RF and the wave signals supplied by two arbitrary waveform generators (AFGs), and the operational amplifiers increased the wave amplitude. Component ranges: R = 2 - 10 kΩ, varaible capacitors 15 - 150 pF, C_L = 1 - 3 nF [12]

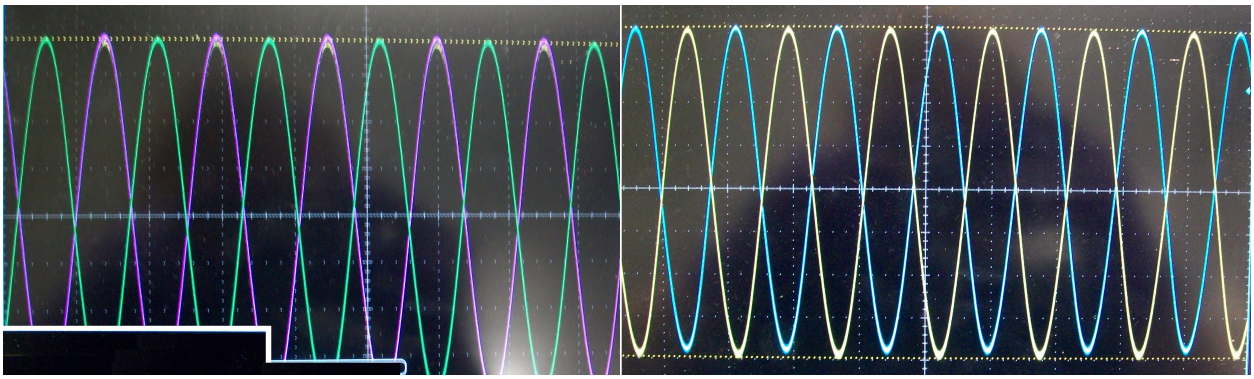

Figure 4.5: Left: The RF signals for phases 3 and 4 (purple and green, 156 and 154 V, respectively) are shown on the oscilloscope. Right: The RF signals for phases 1 and 2 (yellow and blue, 154 and 153 V, respectively), which were hidden behind the signals for phases 3 and 4. The RF amplitude agreement among the four phases is excellent, less than 2%.

Figure 4.5. Tuning the RF circuit initially involved the winding of small gauge wires around small alligator clips, which were attached to long, thick wires suspended above the carpet as shown in Figure 4.6 (left). The four clips were positioned so that each fine wire was only touching one carpet electrode, with each clip and wire in contact with a different phase. Probes were connected to the long wires, and the signals were monitored on an osilloscope. The frequency of the RF signal was varied to find the value of least reflected power (or most power delivered to the load). Once this resonance condition was found and the amplitudes of the four phases matched, the RF amplitudes both inside the chamber on the carpet and at the external feedthroughs outside the chamber were recorded. The ratio of the amplitudes on the carpet to that at the feedthrough was used to determine the RF amplitude on the RF carpet.

The fine wires and probes were removed before closing the chamber. After which, the frequency was adjusted ($\sim$0.1 MHz) to minimize the reflected power. The tuning procedure was modified for the linear prototype measurements (see Chapter 5) to avoid the small fre-

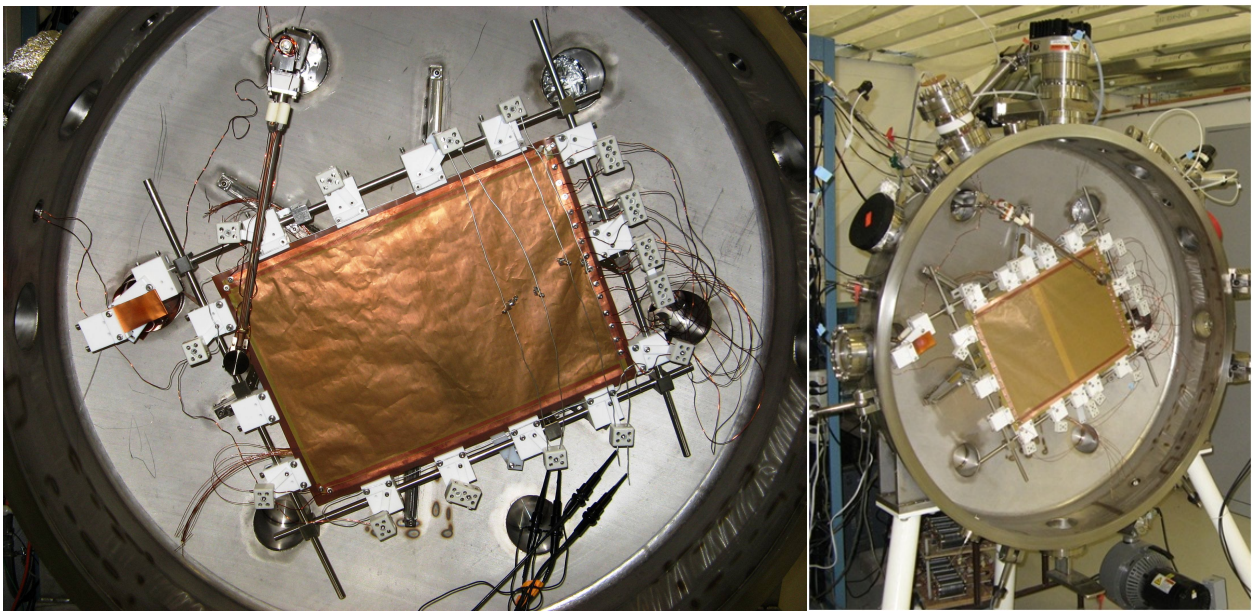

Figure 4.6: Left: The first large linear ion surfing RF carpet prototype. The long wires and alligator clips above the right side of the carpet were used to tune the RF frequency and amplitude. The oscilloscope probes are attached at the end of the long wires suspended above the carpet surface. Right: The RF carpet ion jumping prototypes. The change in color of the carpet in the center indicates the area of overlap.

quency shift when the tuning probes were removed. The oscilloscope probes were attached directly to the RF carpet electrodes at the carpet-to-frame connections, and the four electrodes were tuned as before by adjusting the RF frequency and capacitance. The probes were then removed, the RF frequency re-tuned, and the RF amplitudes recorded (after further tuning if necessary) by measuring one phase at a time along the carpet traces and bus bar. A bus bar is a copper strip along the edge of the carpet that connects to all the traces of one phase. The RF signal was also monitored by measuring the RF picked up by a small inductor placed within a few cm of the carpet surface or by an unused carpet region for the later semi-circular protoype. Unlike the power delivered to the circuit, both the RF pickup amplitude and RF amplitude were found to vary roughly linearly with the RF gain as shown in Figure 4.7.

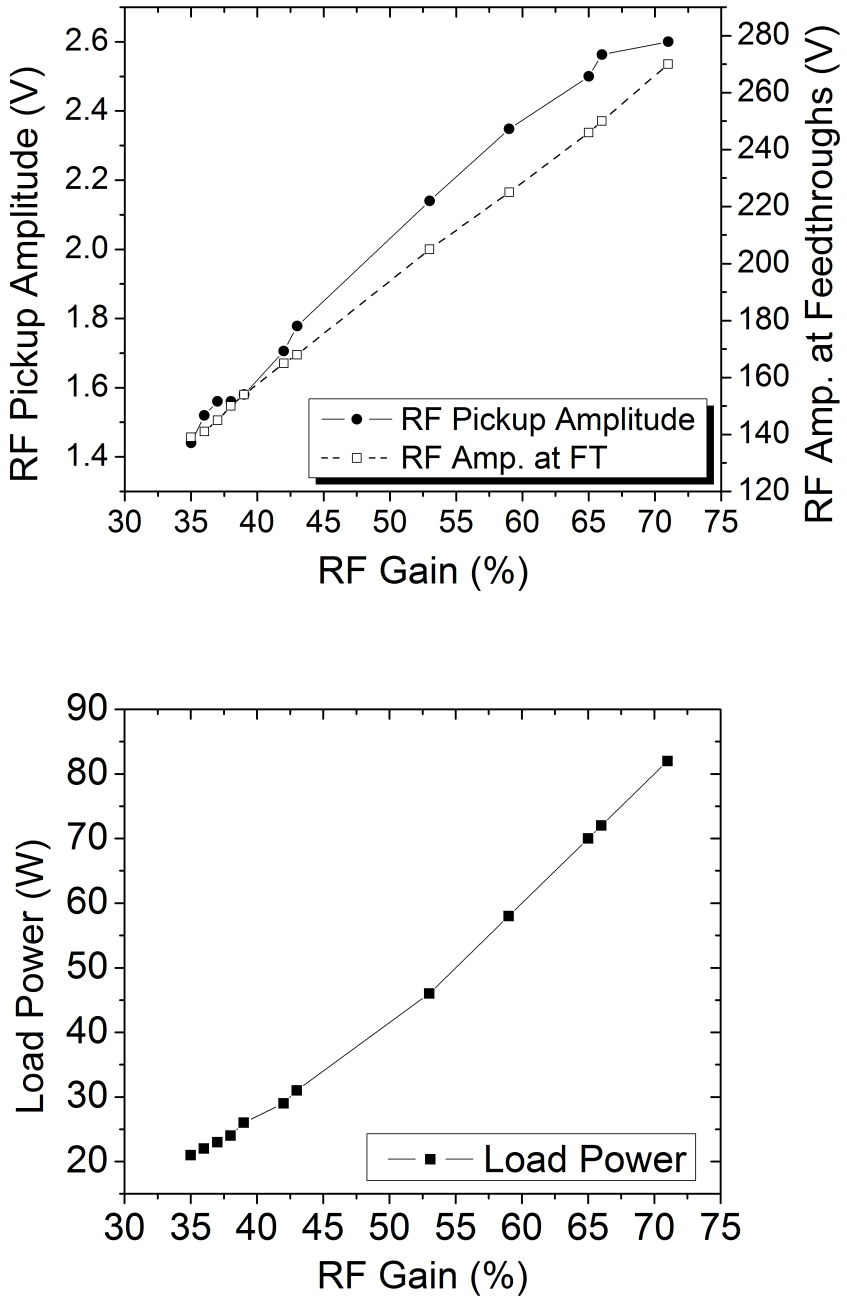

Figure 4.7: Above: The RF pickup (closed circles) and amplitude (open squares) at the chamber feedthroughs increase roughly linearly as the gain of the RF generator also increases. Below: The power delivered to the carpet and circuit increases nonlinearly with RF amplifier gain at low values of gain.

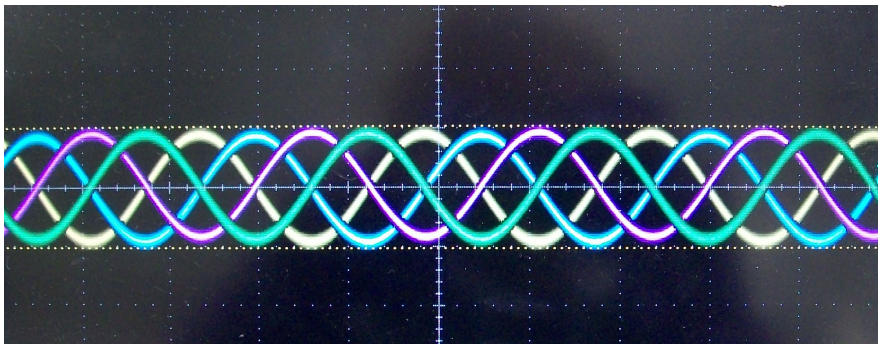

Figure 4.8: The four traveling wave phase signals observed on an oscilloscope.

Two time-synced Tektronix Model 3102 dual-channel arbitrary waveform generators (AFGs) supplied the traveling wave signals, which were amplified by AC817 op amps, as shown in Figure 4.4. The op amps placed in series with the 2 kΩ resistors prevented the RF signal from reflecting back into the wave signal generators. The wave amplitudes were matched by monitoring the signals at the chamber feedthroughs with an oscilloscope and modifying the output amplitude from the AFG. The traveling wave amplitude was the same on the carpet as at the chamber feedthroughs. The phases of the traveling wave on the carpet electrodes did not change significantly from those of the input signals to the carpet, and the amplitudes were matched to within 5%. An example of the four wave signals as captured from an oscilloscope trace are given in Figure 4.8. The electronics utilized in the ion surfing experiments and their purposes are listed in Table 4.1.

4.2 Measurement Procedures

The overall goal of this work was to experimentally demonstrate ion surfing as a viable method for transporting thermal ions quickly and efficiently through helium buffer gas. Thus, two types of measurements were conducted to determine the performance of the system:

Table 4.1: List of equipment used in the ion surfing RF carpet experiments.

Item	Use
Power Supplies	
Spectrum Solutions, Inc. 9-Channel 500 V	Apply bias voltages
SRS Model PS 350 5000V 25 W HV	Apply voltage to push plate
Diehard 950 Portable Battery	Supply heater current to ion source
Arbitrary Waveform Generators (AFGs)	
Agilent 33120A	Switching signal for velocity meas.
Tektronix Model 3102 Dual Channel (x2)	Provide traveling wave signal
RF Generator	
T&C Power Conversion, Inc. AG Series	Provide RF signal
Measurement tools	
Agilent Tech. DSO1004A 4-Channel Oscilloscope	Measure RF and traveling wave
Tektronix TDS 3032B 2-Channel Oscillosope	Save signals for velocity meas.
Keithley 6514 System Electrometer	Measure ion source current
Keithley 6485 Picoammeter (x2)	Measure lens and collection currents

ion transport efficiency and ion velocity. The procedures for the efficiency and velocity measurements [12] are detailed in Sections 4.2.1 and 4.2.2, respectively.

4.2.1 Efficiency Measurements

Three currents must be measured to determine the ion transport efficiency: the ion current leaving the source, I_{source}, the ion current hitting the lens, I_{lens}, and the ion current reaching the collection pads, I_{coll}. The number of ions reaching the carpet was quantified by I_{carpet}:

$$I_{carpet} = I_{source} - I_{lens} \tag{4.1}$$

and the transport efficiency, η, was defined as:

$$\eta = \frac{I_{coll}}{I_{carpet}} \tag{4.2}$$

Often, the fraction of ions transported over a given distance, f_{trans}, is reported because

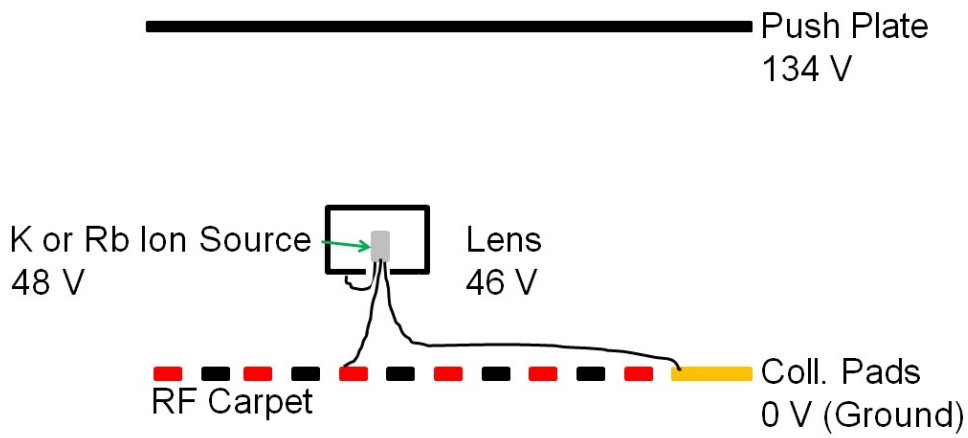

Figure 4.9: A schematic of the efficiency measurement method. The thin black lines represent typical ion trajectories. The voltages shown are the typical values needed to create 1 nA of ion beam at 80 mbar and 10 V/cm push field.

any initial ion losses (for example, due to space charge under the source) will cancel out. f_{trans} is defined as follows:

$$f_{trans} = \frac{\eta_{far}}{\eta_{near}} \tag{4.3}$$

where η_{near} is the transport efficiency over some short distance, and η_{far} is the transport efficiency over a longer distance. A schematic diagram of the efficiency measurements with typical voltages applied to the carpet, push plate, and source is shown in Figure 4.9.

4.2.2 Velocity Measurements

The ion transport velocity was deduced by measuring the transport time of the ions for different distances of the ion source relative to the collection pads. For the initial prototype carpets, the transport time at three different distances was measured. For the linear and circular prototypes, the transport times for 7 and 5 distances were measured, respectively. A switching signal (often of 1 Hz) was applied to pulse the ouput of the ion source, and was also

used to trigger the oscilloscope (voltage change at time = 0 s). When the ion source voltage was greater than the lens voltage, ions exited the ion source. When the ion source voltage was several volts less than the lens signal, the ions were repelled back into the source and no current was emitted. Typical voltages applied to the carpet, push plate, and ion source for ion velocity measurements at 80 mbar and a 10 V/cm push field are shown in Figure 4.10. The ion current that reached the collection pads was measured on the oscilloscope with the analogue output of the collection pad picoammeter. Two of the typical ion current signals after the voltage was switched are shown in Figure 4.11 (above). The plateau of the signal indicates the end of the distribution of ions that reached the collection pads from the ion source because the picoammeter output is inverted relative to the actual current. The distances of the ion source for the two signals in Figure 4.11 (above) are indicated and, as expected, the ions require more time to traverse the longer distance. To determine the ion velocity, the midpoint of the signal rise was determined from the fit of a Fermi-Dirac function plus a noise term:

$$V_{scope} = \frac{a-b}{1+e^{\frac{t-t_0}{d}}} + c \cdot \sin(377\mathrm{t} + \phi_0) + \mathrm{b} \tag{4.4}$$

where t is the time and V_{scope} the signal voltage. V_{scope} is shown on the ordinate in Figure 4.11 (above) and t is along the abscissa. The frequency of the noise was 60 Hz (377 rad/s). The midpoint of the rise, t_0, is taken as the ion transport time. Additional constants fit to the equation are scaling factors a and c, ordinate-intercept b, phase shift ϕ_0, and the slope of the signal rise d. The resulting transport times are plotted versus the transport distances, as shown in Figure 4.11 (below). The y-intercept is the time required for the ions to drop to the carpet, t_{drop}, and the data can be fit to the linear function:

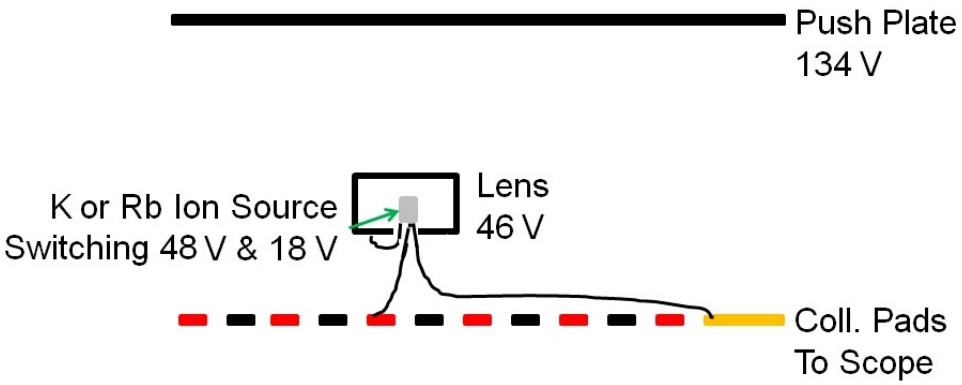

Figure 4.10: A cartoon of the velocity measurement method. The black lines represent typical ion trajectories. The voltages shown are the typical ion switching values for a 10 V/cm push field at 80 mbar. Unlike the efficiency measurements, the current collected by the collection pads is viewed on an oscilloscope.

$$v_{ions} = \frac{x}{t_0 - t_{drop}} \tag{4.5}$$

where v_{ions} is the ion velocity and the slope of the line, x is the ion transport distance, and t_0 is the ion transport time. The uncertainty of the velocity is taken from from the least-squares fit.

4.3 First Linear Prototypes and Select Results

The following section provides a summary of the tests performed with the first two ion surfing RF carpet prototypes. All of the RF carpets tested in this work were obtained commercially [71] and were produced by depositing copper onto 1 mil thick Kapton substrate. Both prototypes discussed in this section had a linear geometry and are pictured in Figure 4.6. The first RF carpet was 40.5 cm x 56.5 cm in size with a pitch of 0.5 mm and a γ of 0.5 and was designed by Pang [10]. An objective of the second set of RF carpet tests was to jump the ions from one carpet to another in order to investigate transporting ions over distances

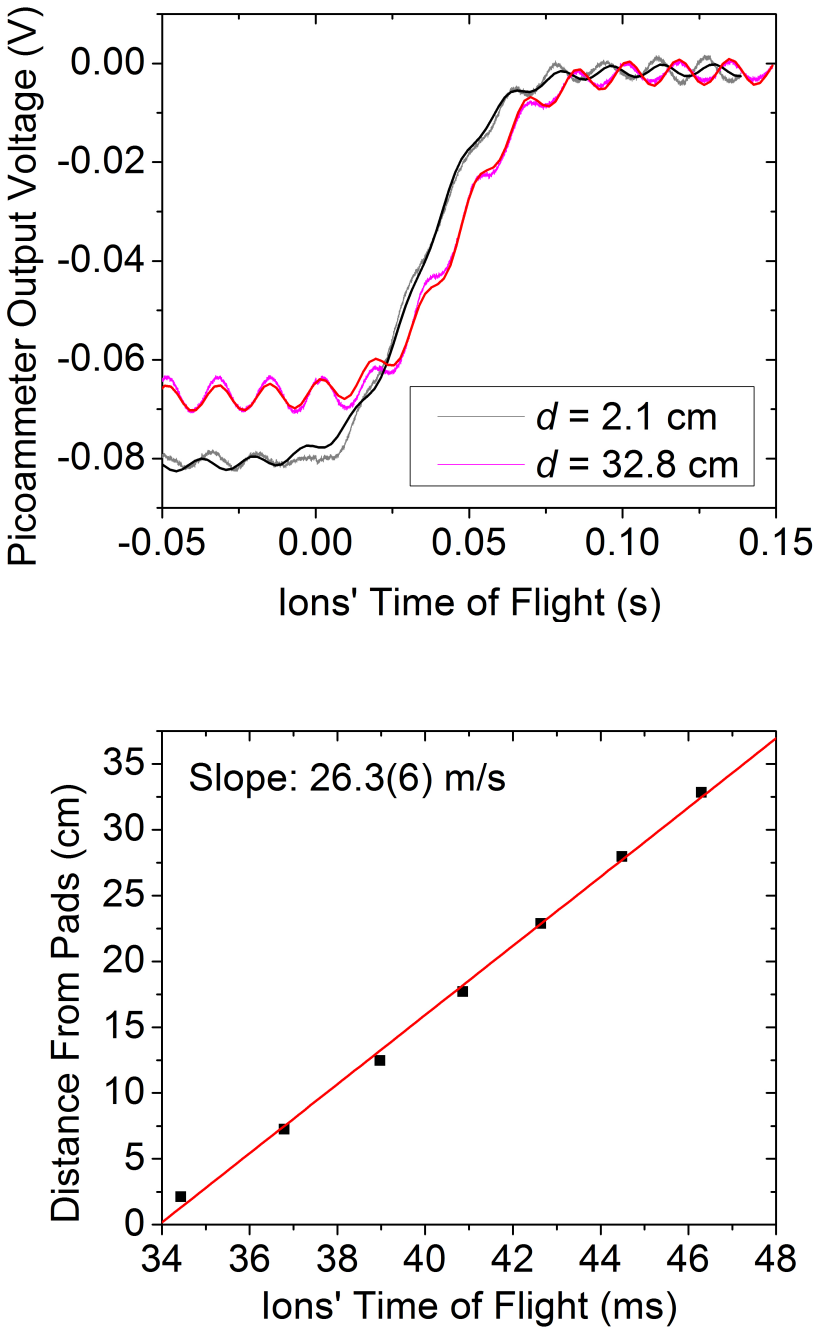

Figure 4.11: Above: Two signals from the inverted output of the picoammeter connected to the collection pads. At 0.00 s the ion source voltage was switched. A Fermi-Dirac function with a 60 Hz sinusoidal noise profile (dashed line) was fitted to each signal in order to determine the time of the midpoint of the rise. Below: Example of distance versus time data for seven points along the linear surfing prototype (see Chapter 5). The typical error value was 0.02 ms and is not visible on the graph. The slope of the fitted line is the ion velocity [12].

longer than the current manufacturing limits. The second carpet dimensions were 41.5 cm x 28.5 cm, and two carpets were mounted in the frame as shown in Figure 4.6 (right). These carpets had the same pitch as the first test carpet, 0.5 mm, but a γ of 0.75, which was at the manufacturing limit of trace width.

4.3.1 Results from the $\gamma = 0.5$ Carpet

The first efficiency and velocity measurements were conducted for the prototype carpet with $\gamma = 0.5$ and a = 0.5 mm. The most important result was observation of the effect of the RF frequency on ion transport efficiency as shown in Figure 4.12 (above). The efficiency measurements were completed at three different frequencies: 1.03, 1.55, and 2.16 MHz. The range of RF frequencies was the largest of any of the carpets tested in this work. As shown in Figure 4.12, increasing both the RF amplitude and frequency increased the transport efficiency, as predicted. However, ion velocities only reached 22 m/s, and the transport efficiency was found to decrease at the wave amplitudes required for the highest ion velocities. The maximum RF amplitude was set slightly below the discharge limit; therefore, further increase of the RF amplitude was not possible. The results led to the conclusion that additional circuit development was needed to operate a carpet in resonance for higher RF frequencies to repel the ions farther from the carpet surface, which would in turn increase the transport efficiencies.

4.3.2 Results from the $\gamma = 0.75$ Carpet

The best results from the tests of jumping ions from one carpet to another are shown in Figure 4.13. Initially, the carpets were separated by a vertical distance of 0.635 cm, as

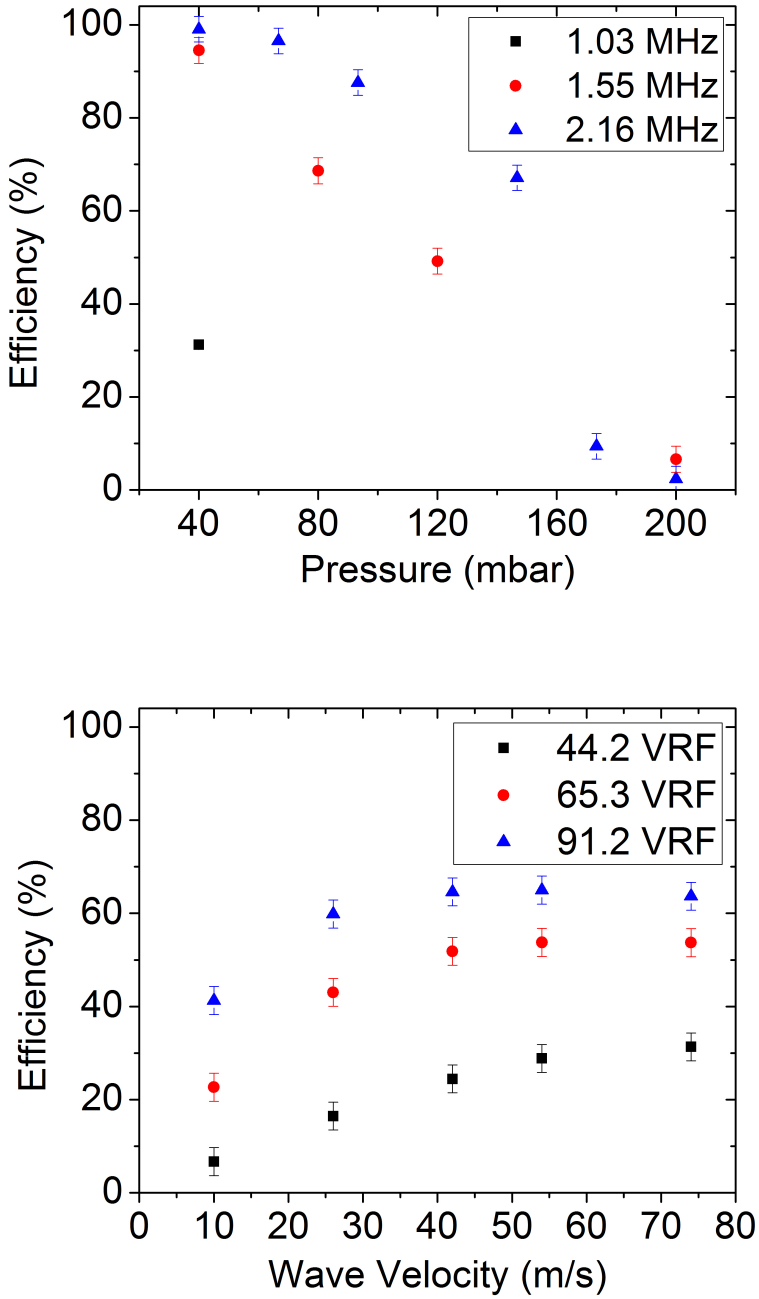

Figure 4.12: Above: The effect of increasing the RF frequency on ion transport efficiency over 20 cm as a function of buffer gas pressure. The common parameters for the three data sets are Rb^+ ions, 3 V/cm push and ~90 (84-96) V RF amplitude. The wave amplitudes and velocities varied from 0.5 to 2 V and 13 to 26 m/s, respectively. The best experimental results were chosen. Below: Transport efficiency over 20 cm versus wave velocity for three RF amplitudes. The error is estimated to be 3%. The remaining parameters are Rb^+ ions, 10 V/cm push field, 40 mbar buffer gas pressure, 1.55 MHz RF frequency, and 1.9 V amplitude traveling wave.

shown in Figure 4.14. The ions started on carpet 1, traveled 30 cm and then had to jump across to carpet 2. Ions were successfully transported from the first carpet to the second at 40 mbar, but the transport efficiency decreased drastically at the boundary between the carpets at 120 mbar, as shown in Figure 4.13 (left). To improve the efficiency, the carpets were taped together to minimize the distance between the carpets, and the results are shown in Figure 4.13 (right). Although the transport efficiency does decrease in the region of carpet overlap (20-25 cm in Figure 4.13 right), increasing the RF frequency decreased the ion losses. This relationship could be investigated further for applications requiring ion transport over distances longer than the manufacturing limit of RF carpets. However, as discussed later, a semi-circular carpet design was developed in this work that did not require the ions to move across carpet joints.

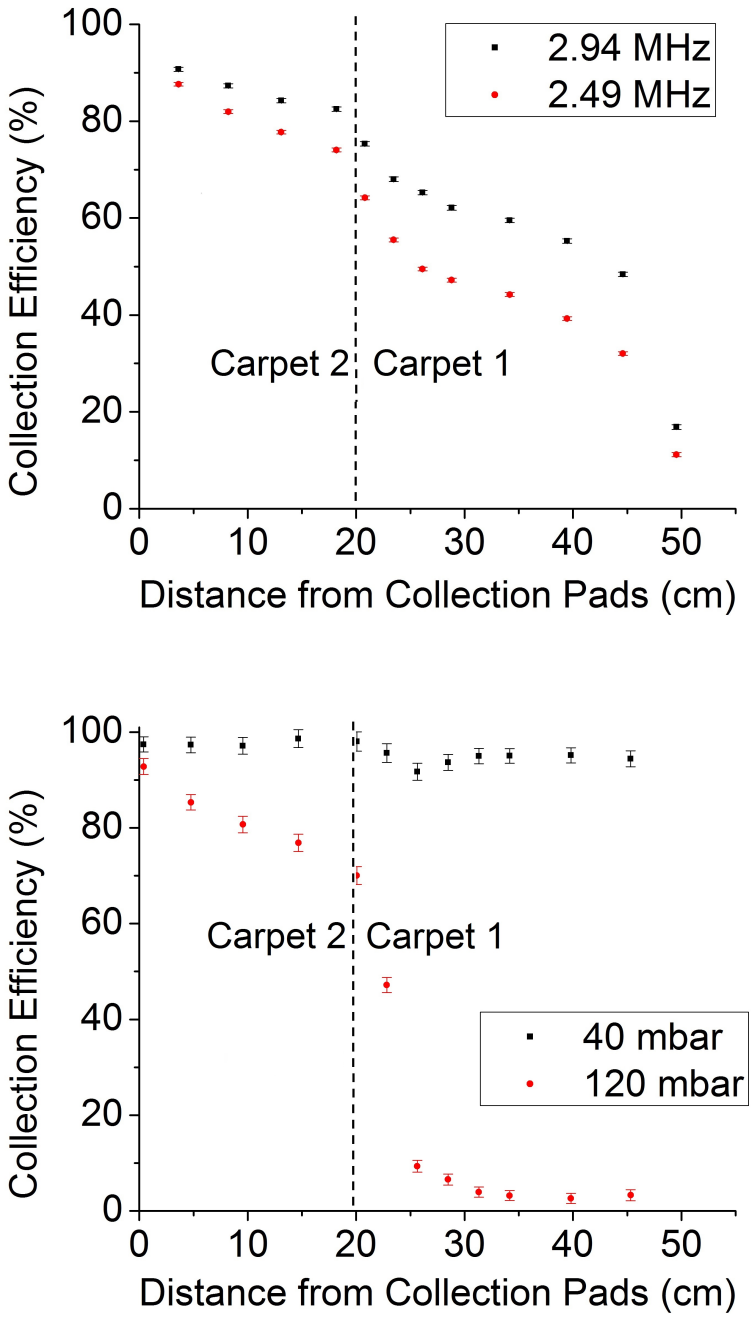

Figure 4.13: Efficiency plotted as a function of transport distance for Rb^+ ions at two different carpet separation distances. The location of the boundary between the carpets is indicated on both graphs. Above: Efficiency results at two different pressures for a carpet separtion distance of 0.635 cm. Other parameters are as follows: 3 V/cm push field, 3.17 MHz RF frequency, 84 V RF amplitude, 26 m/s and 3 V amplitude traveling wave. Below: Transport efficiency results for two different RF frequencies when the carpet separation was minimal. Other parameters are as follows: 3 V/cm push field, 120 mbar, 80 V Rf amplitude, and 3 V amplitude 26 m/s traveling wave.

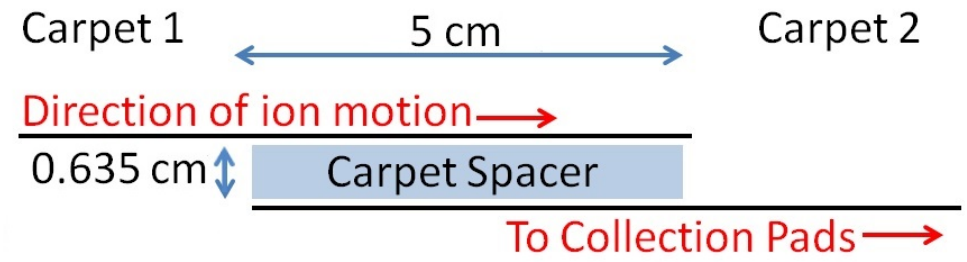

Figure 4.14: A cartoon of the cross section of the overlap region of the carpets used in the initial ion jumping experiments. The carpets are indicated by solid lines, and the carpet thickness is not drawn to scale (actual thickness: 0.0254 mm). The ions jump from Carpet 1 to Carpet 2.

Chapter 5

Linear Prototype Measurements

A large linear prototype RF carpet was designed with trace and space widths at the manufacturing limits of Innovative Circuits, Inc. [71], the company that provided most of the previous RF carpet prototypes both for the surfing and traditional methods [10]. This carpet is pictured in Figure 5.1 and the inset provides a close-up image of the 0.125 mm traces and 0.25 mm gaps (a = 0.375 mm, $\gamma = 0.67$). The carpet size is 27 cm by 47 cm, with the carpet traces covering an area of 15 cm by 40.5 cm.

5.1 Experimental Results

Many transport efficiency and velocity measurements were conducted with the carpet. A summary of this series of measurements, including selected results, was recently published in Ref [12]. The carpet was tuned to the RF frequency of ∼6.6 MHz for the majority of the measurements, and the frequency was varied little during the measurements. From a comparison of the calculations shown in Figure 2.5, this carpet operated at a frequency of 6.6 MHz produces a greater repelling force than the previously tested carpets discussed

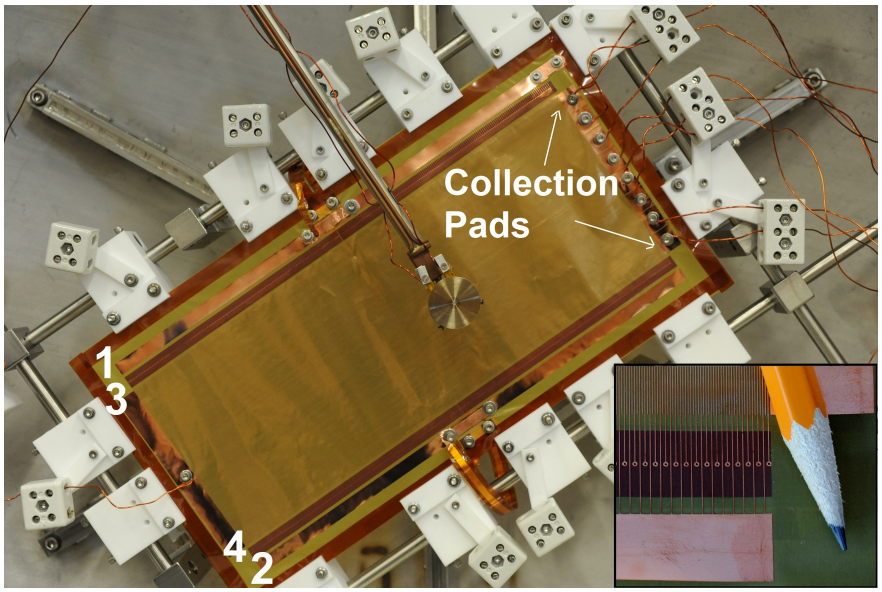

Figure 5.1: The linear prototype ion surfing RF carpet mounted in the test chamber. The ion source is above the center of the carpet. The four bus bars that supply the RF and wave signals for each phase are numbered by wave phase, and the 8 collection pads are labeled. The inset shows a close-up of the ion traces and spaces (0.125 mm and 0.25 mm wide, respectively) with a pencil shown for scale. The circular ends of the traces are the vias that connect to the bus bar on the back of the carpet.

in Section 4.3. The larger repelling force was found to significantly improve ion transport efficiency. Therefore, future RF carpets with $a = 0.375$ mm and $\gamma = 0.67$ will be tuned to high RF frequencies (> 6 MHz) if possible. The RF amplitude was kept near the discharge limit for most tests, approximately 75 V with less than 20% mismatch among the phases (often, less than 5% mismatch). The push, pressure, and wave parameters were varied and the transport efficiency and velocity for Rb^+ and K^+ ions were deduced. The presentation of the results is divided by ion mass in the following sections. Unless otherwise indicated, the ion source voltage was adjusted so that 1 nA of ion current was incident on the carpet during the measurements.

5.1.1 Rubidium Ion Transport Results

The ion current collected on each of the eight collection pads indicated in Figure 5.1 could be read individually or as a group on a picoammeter. The ability to measure the current on each individual collection pad made it possible to deduce the distribution of the ions across the carpet surface. The ions diffused laterally during transport, and some ions may be lost at the edges of the carpet. If the distribution of the ions was found to be greater than the width of the carpet, the ion transport efficiency would need to be adjusted to compensate for such losses. An example of a measurement of the ion current distribution on the collection pads is shown in Figure 5.2. The ions traveled 30 cm, and the data in the figure represents one of the broader distributions observed, where the large width was attributed to the slow speed of the ions. The ion velocity under the conditions of the measurement is approximately 10 m/s, as deduced from the data in Figure 5.3 (left). The ion velocity for the distribution shown in Figure 5.2 is likely less than 10 m/s due to the lower push field. Even so, the majority of the ions were found to remain on the surface of the carpet.

An early measurement of the collection efficiencies versus distance for Rb^+ ions is shown in Figure 5.4. Although the transport efficiency is excellent ($> 80\%$), the overall efficiency decreases at the higher wave amplitude. Also at the higher wave amplitude, the efficiency is observed to decrease slightly as the transport distance increases. The Rb^+ ions were transported under 120 mbar of helium buffer gas pressure, which is near the upper limit of the planned operating range of the cyclotron gas stopper. For a transport distance of $\sim$35 cm, the transport efficiency is above 80% for both wave amplitudes, representing a significant improvement when compared to the overall efficiency (stopping plus collection efficiency) of a linear gas cell.

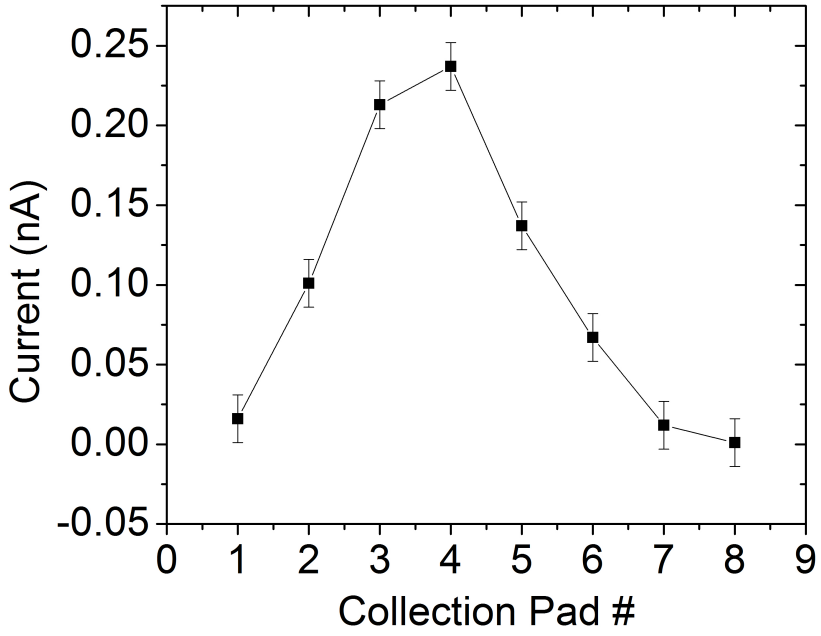

Figure 5.2: Example of the distribuition of the Rb^+ ion current over the 8 collection pads. The summed current is 0.784 nA, and, based upon other results, the ion velocity is less than 10 m/s. The uncertainty is estimated to be 0.015 nA. Parameters: 30 cm transport distance, 120 mbar, 3 V/cm push field, 7.6 MHz RF frequency, 70 V RF amplitude, 60 m/s and 2 V amplitude traveling wave.

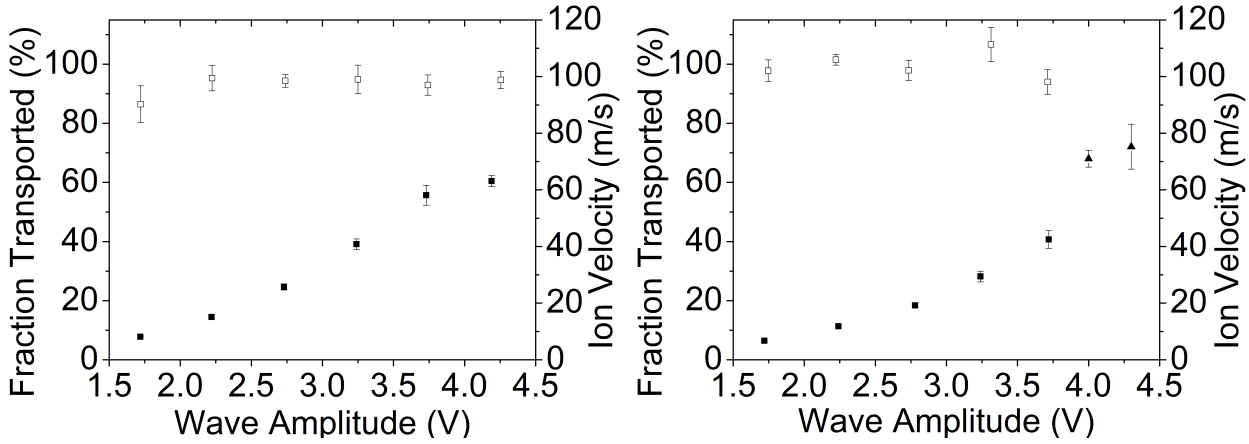

Figure 5.3: Ion velocity (solid squares) and fraction transported (open squares) over 25.7 cm results for Rb^+ ions at two wave velocities. Common parameters: a = 0.375 mm, γ = 0.67, 120 mbar, 45 V/cm push field, 6.69 MHz RF frequency, 66 V RF amplitude. Left: Experimental results for 60 m/s velocity. Right: Similar results for 75 m/s wave velocity.

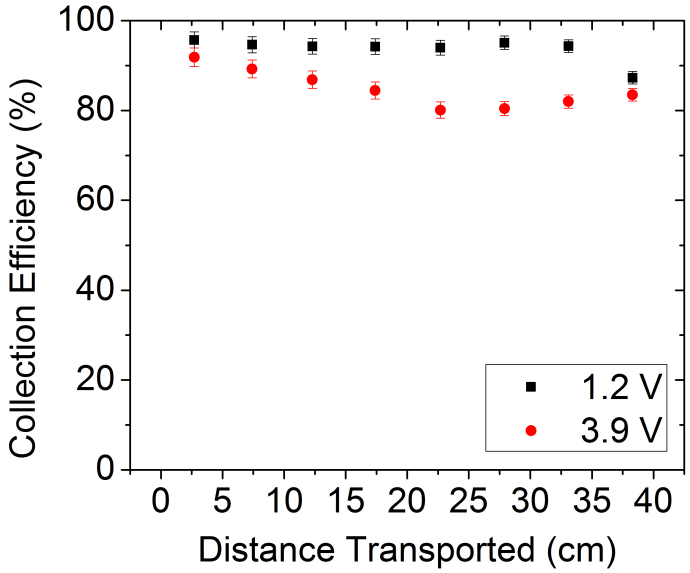

Figure 5.4: Collection efficiency as a function of transport distance for Rb^+ ions at two wave amplitudes with the linear prototype carpet. Parameters: a = 0.375 mm, γ = 0.67, 120 mbar, 6.51 MHz RF frequency, 81 V RF amplitude, 12 V/cm push field and 15 m/s wave velocity.

The ion velocities and the fraction of the ions transported over 25.7 cm as a function of wave amplitude at higher wave velocities, for a buffer gas pressure of 120 mbar, are shown in Figure 5.3. As expected, a larger wave amplitude is required to obtain locked mode at a wave velocity of 75 m/s (Figure 5.3 right) than at 60 m/s (left). Note that these measurements were taken with a low buffer resistance of R = 1 kΩ (see Figure 4.4). The high wave amplitudes were attainable due to the decreased resistance. Unfortunately, the resistors were unable to dissipate the substantial heat generated during operation with the RF signal, and each resistor was replaced by three 10 W power resistors in parallel with a total resistance of 2 kΩ. In later experiments at 120 mbar, a wave amplitude large enough for 75 m/s ion transport velocity was not achievable. The excellent transport efficiency for the high ion transport velocities attainable at 120 mbar is also shown in the figure. The collection efficiency as a function of distance is shown in Figure 5.5 for the same set of

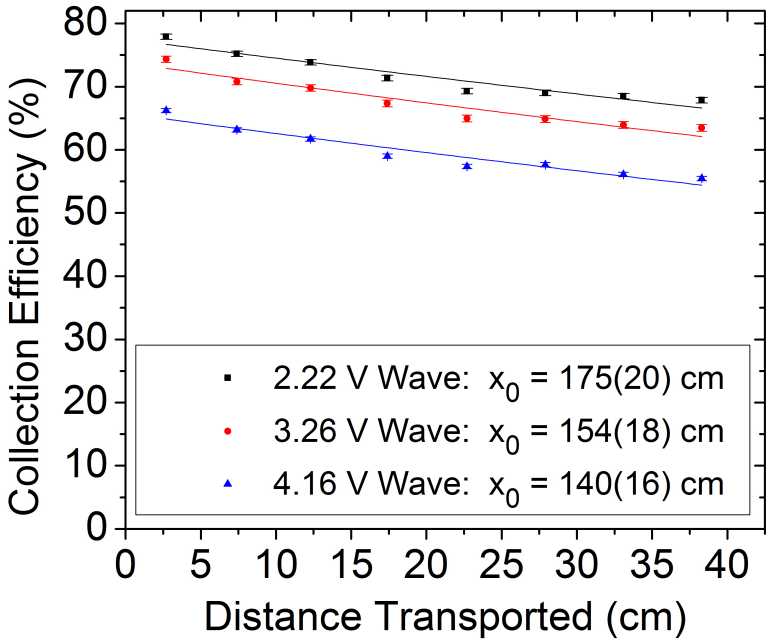

Figure 5.5: Collection efficiency as a function of the distance traveled by Rb^+ ions at three different wave amplitudes. The solid lines represent the best fit of Equation 5.1 to the data, and the half distances, x_0, are listed on the graph. Parameters: a = 0.375 mm, $\gamma = 0.67$, 120 mbar, 45 V/cm push field, 6.69 MHz RF frequency, 66 V RF amplitude, and 60 m/s wave velocity.

conditions as Figure 5.3 (left). The distance over which half the ions are lost, or the "half distance," can be determined by fitting the following equation to the data:

$$\eta_{coll}(x) = 2^{\frac{-x}{x_0}} \tag{5.1}$$

where η_{coll} is the collection efficiency (see Equation 4.2), x is the distance traveled by the ions, and x_0 is the half distance. The half distance decreases with increasing wave amplitude, as shown in Figure 5.5, which is expected since the transport efficiency decreases with increasing wave amplitude. The deduced large half distances serve as another indicator of the excellent transport efficiency possible for Rb^+ ions at 120 mbar. A comparison of Figures 5.3 (left) and 5.5 demonstrates two measures of efficiency: collection efficiency and fraction transported. In Figure 5.5, the efficiency for ions deposited onto the carpet near the collection pads is not 100%, because some ions are forced into the carpet surface by the space charge immediately under the source. The current reaching the carpet, I_{carpet}, was not reduced to less than 1 nA since the uncertainty of each current measurement was as large as ~0.01 nA. The initial losses are greater at the higher wave amplitudes since the ions can migrate closer to the carpet surface in deeper wave pockets. The "fraction transported" does not reflect these initial losses and provides a better accounting of the ion transport efficiency over the carpet.

The deduced ion velocities are compared to Surf2D simulation results in Figure 5.6 for two sets of conditions. The differing parameters include both buffer gas pressures of interest, 80 and 120 mbar. The experimental trends are well reproduced by the simulations. The greater slope of the rise of the ion velocities at the faster wave velocity is also observed in both the Surf2D simulation results and the experimental results. Based on the good

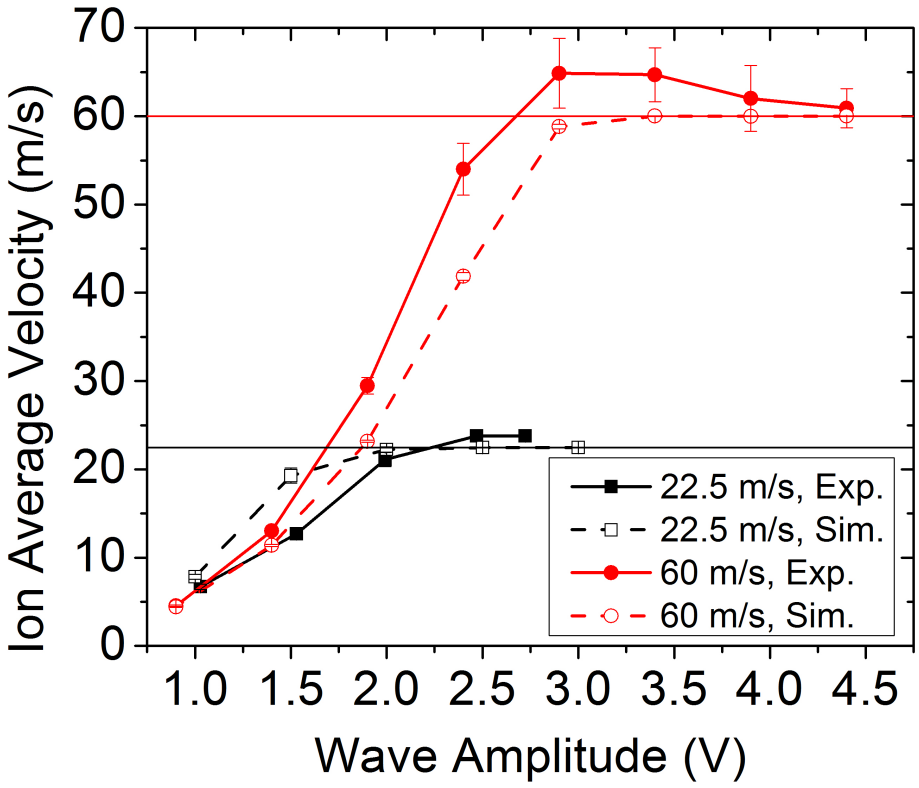

Figure 5.6: Comparison of experimental results (solid lines) to Surf2D simulation results (dashed lines) for Rb^+ ions at two different sets of parameters with the linear prototype carpet. Black squares: 120 mbar, 6.51 MHz RF frequency, 76 V RF amplitude, 45 V/cm push field and 22.5 m/s wave velocity. Red circles: 80 mbar, 6.69 MHz RF frequency, 74 V RF amplitude, 30 V/cm push field and 60 m/s wave velocity [12].

agreement in Figure 5.6, Surf2D was used to simulate other ion surfing conditions that were unable to be physically tested.

The measured effect of both push field and pressure on ion velocity is shown in Figure 5.7. Increasing the buffer gas pressure by a factor of 3 (40 mbar, black squares to 120 mbar, red circles) decreases the ion velocity in the expected way (see Figure 3.6). Increasing the push field by a factor of ∼2 (20 V/cm, red circles, to 45 V/cm, green triangles) increases the ion velocity, again as predicted. This effect is noticeable at the lower wave amplitudes where the higher push field raises the ion velocity ∼2 m/s closer to the locked mode of 15 m/s. Note that the data point at the highest wave amplitude for 45 V/cm, 120 mbar has a large uncertainty due to the low efficiency and correspondingly diminished signal. However, increasing either the push field or the buffer gas pressure has less of an effect on the ion velocity than the wave amplitude. In order to achieve fast ion transport, a high wave velocity and large amplitude are necessary.

The fastest ion velocity results with the requirement that the half distance be greater than 0.5 m are shown in Figure 5.8. For these measurements, the ion losses over 20 cm were limited to a maxiumum of 20%. All of the ion velocity values deduced at 80 and 120 mbar that had a push field of less than or equal to 35 V/cm represent a weighted average of at least three measurements. The wave velocities used to obtain the results are represented by dashed lines in Figure 5.8. The wave amplitudes were adjusted to obtain the required half distance, and the RF amplitude was decreased from the common value of ∼75 V for all the measurements at 80 and 120 mbar in order to increase the ion velocity. The half distance limit of 0.5 m is larger than the ∼0.35 m that ions with mass = 85 u will need to travel to reach the center of the cyclotron gas stopper. Therefore, the practical lower limit

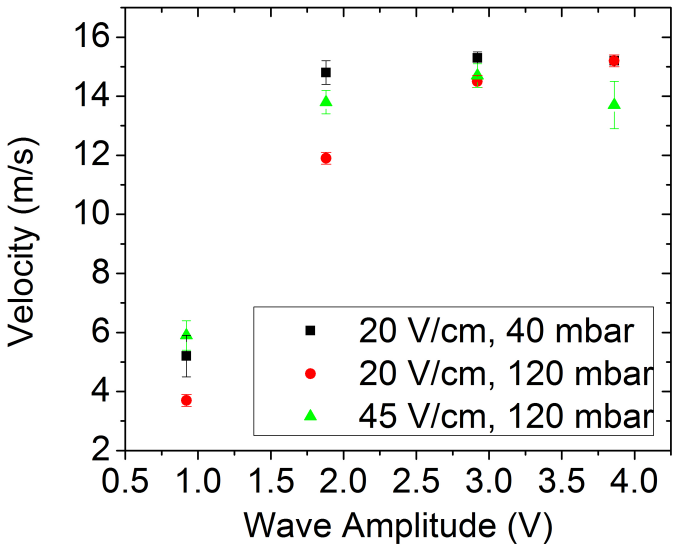

Figure 5.7: Effect of push field and buffer gas pressure on the ion transport velocity of Rb^+ ions. Parameters: a = 0.375 mm, $\gamma = 0.67$, 6.51 MHz RF frequency, 76 V RF amplitude, 15 m/s wave velocity. Although the changes in push field and pressure affect the ion velocity as predicted, altering either variable does not effect the ion velocity as strongly as the wave amplitude.

of efficiency for the ion velocities shown in the figure under the device's operating conditions is ∼65%. Ion velocities as high as 75 m/s can be reached at the lower cyclotron gas stopper operating pressure of 80 mbar, resulting in a transport time of about 5 ms. The equivalent DC field needed to transport ions at this velocity by the traditional RF carpet method can be estimated using the simple equation:

$$K = \frac{v_{ion}}{E} \tag{5.2}$$

where K is the ion mobility (see Equation 2.7), v_{ion} is the ion velocity, and E is the electric (drag) field. In order for transport velocities of 75 m/s to be obtained at 80 mbar, a DC gradient of 27.4 V/cm or a total of 1370 V over 50 cm would be needed. Typical DC gradients in helium gas are ∼10 V/cm due to the difficulty in maintaining the high static

fields without discharge. At 120 mbar, the 50 m/s ion transport velocity achieved by the ion surfing method would also require approximately 27.4 V/cm drag field in the traditional method. At an ion velocity of 50 m/s, the transport time over 0.35 m would be 7 ms. The short extraction times predicted for the cyclotron gas stopper are significantly less than those of linear gas cells. For example, the first generation NSCL gas cell had an average extraction time of approximately 125 ms [18]. The faster extraction times will result in reduced ion losses of short-lived nuclei due to radioactive decay.

The rubidium ions were also found to be transported efficiently at higher helium gas pressures of 160 and 200 mbar, but the ion velocities decreased considerably as the pressure increased. None the less, ion transport times of 50 ms can be achieved for 50 cm at 160 mbar (recognizing here that the ions would stop at a greater radius in higher pressure buffer gas).

5.1.2 Potassium Ion Transport Results

The collection efficiency versus distance observed for K^+ ions is shown in Figure 5.9. Ions with mass = 40 u are expected to stop ∼20 cm from the cyclotron gas stopper axis, so a wave amplitude between 3.5 and 4.5 V (at 80 mbar, 20 V/cm push field, and 60 m/s wave velocity) should be capable of transporting the ions at high velocity (as show by Figure 5.12) without substantial losses. Even at the high wave amplitude of 4.5 V, the half distance was found to be greater than the predicted distance that mass ∼40 u ions will have to travel to reach the central axis of the cyclotron gas stopper. The initial losses of K^+ ions were found to be less under the set of conditions in Figure 5.9 as compared to those seen for Rb^+ ions in Figure 5.5, likely due to the reduced push field and buffer gas pressure.

Similar trends for the potassium ions as for rubidium ions were observed as the pressure

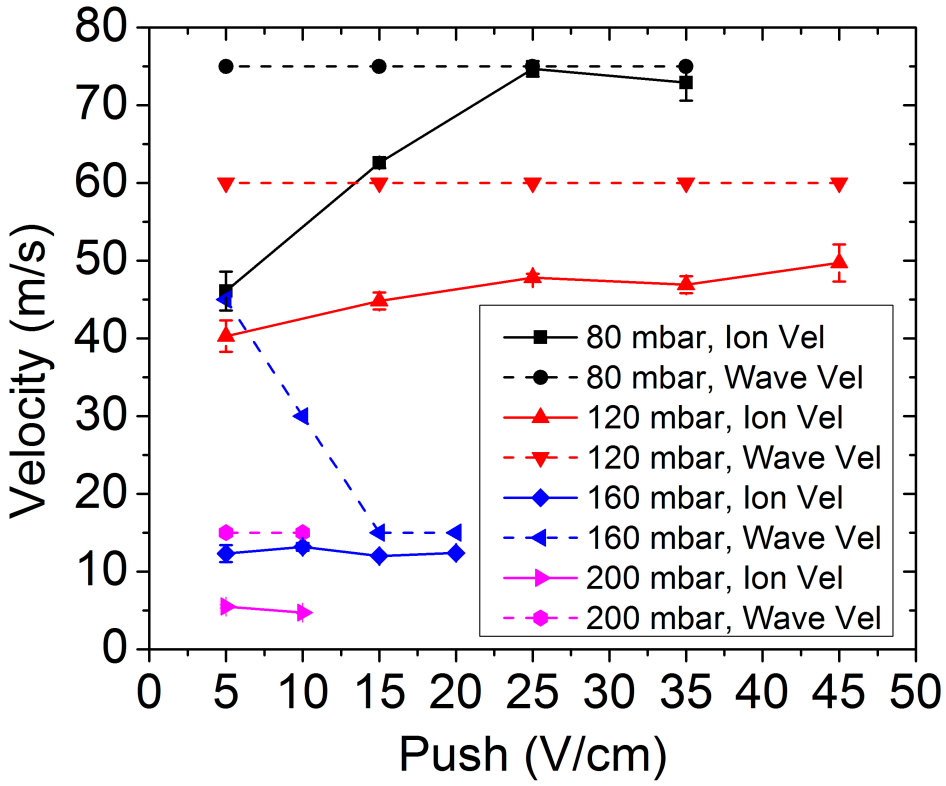

Figure 5.8: The maximum transport velocities for a half distance greater than 0.5 m for Rb^+ ions at four helium buffer gas pressures (solid lines). The dashed lines indicate the corresponding wave velocities for the maximum ion transport velocity measurements.

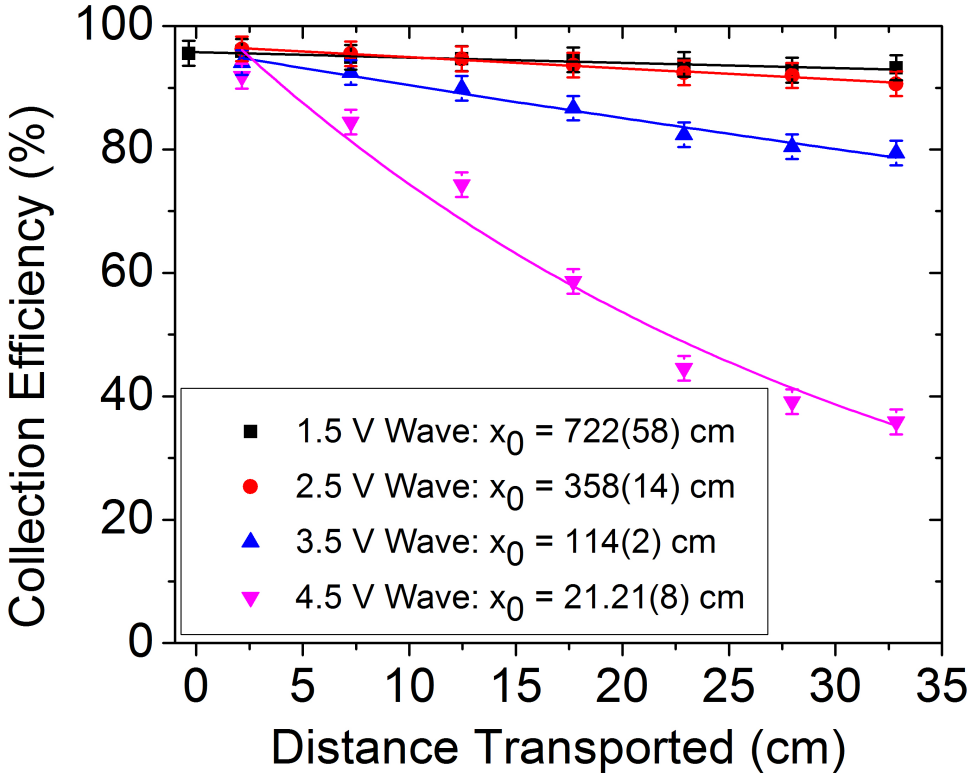

Figure 5.9: Collection efficiency as a function of the distance traveled by K^+ ions at four different wave amplitudes. The solid lines represent the best fit of Equation 5.1 to the data, and the half distances, x_0, are listed on the graph. Parameters: a = 0.375 mm, $\gamma = 0.67$, 80 mbar, 20 V/cm Push, 6.8 MHz RF frequency, 75 V RF amplitude, 60 m/s wave velocity [12].

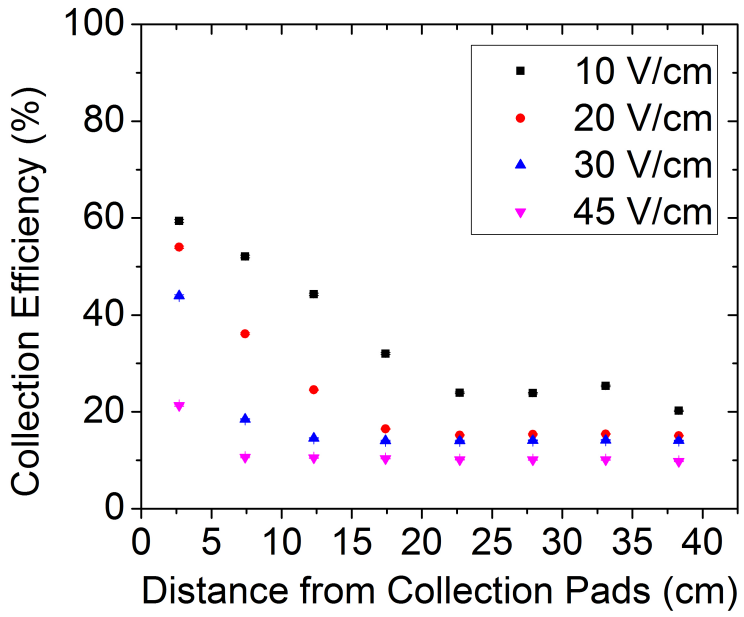

Figure 5.10: Experimental collection efficiency results for K^+ ions at four push field strengths. Parameters: a = 0.375 mm, $\gamma = 0.67$, 120 mbar, 6.73 MHz RF frequency, 71 V RF amplitude, 60 m/s and 4.3 V amplitude traveling wave.

and push field were independently increased. The decrease in transport efficiency with increasing push field for K^+ ions at 120 mbar is shown in Figure 5.10. This pressure is again at the upper range of the cyclotron gas stopper operating conditions. Low push fields will be necessary to transport light ions efficiently unless the RF frequency is increased so that the repelling force also increases. The opposite effect of increasing the push field on ion transport velocity in that the velocity increases, especially for higher wave velocities, is shown in Figure 5.11. At 22.5 m/s wave velocity, increasing the push field by a factor of 4 (black squares to black circles) only slightly increased the ion transport velocity. But at 60 m/s, the increase in push field nearly doubled the ion transport velocity at the highest wave amplitude. For light ions, the push field has a strong effect on both the ion transport velocity and efficiency, but unfortunately improving one aspect of the ion transport comes at a cost to the other.

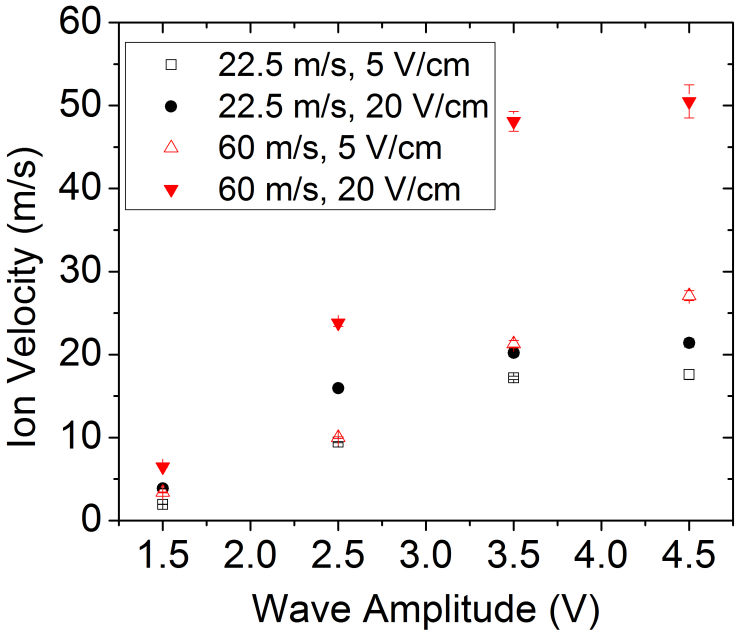

Figure 5.11: Experimental results for K^+ ion transport velocites at two different wave velocities and push fields. Parameters: a = 0.375 mm, $\gamma = 0.67$, 80 mbar, 6.8 MHz RF frequency, 75 V RF amplitude.

The maximum K^+ ion velocities observed with a half distance of 0.5 m or greater are displayed in Figure 5.12. All of the velocity values deduced for 80 mbar and at a push fields greater than or equal to 10 V/cm are from a weighted average of at least two measurements. The wave velocities used to obtain the results are indicated in Figure 5.12 by the dashed lines. The wave amplitudes were adjusted to obtain the required half distance, and the RF amplitudes were not decreased. Again, excellent transport velocities as high as 50 m/s were observed at the lower pressure of 80 mbar. As a reminder, at 50 m/s, mass ~40 u ions are predicted to stop 20 cm from the center of the cyclotron gas stopper and will require ~4 ms to be transported to the exit. At the higher pressure of 120 mbar, the transport velocity is much slower, only 10 m/s, but the transport time would still be relatively short, ~20 ms. The lower extraction times coupled with the greater stopping efficiency of the cyclotron

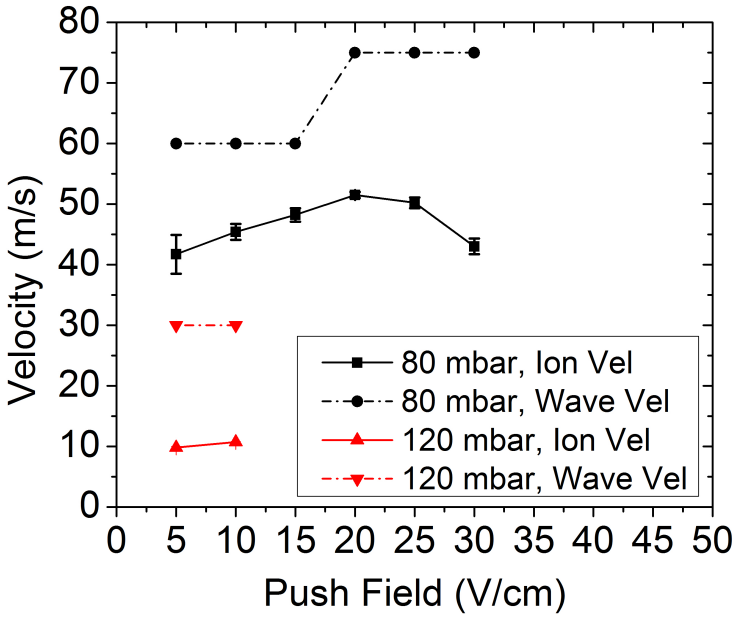

Figure 5.12: The maximum transport velocities for a half distance greater than 0.5 m for K^+ ions at two helium buffer gas pressures (solid lines). The dashed lines indicate the corresponding wave velocities for the maximum ion transport velocity measurements.

gas stopper should increase the overall yield of lighter-mass radioactive ions delivered to precision experiments and the reaccelerator compared to that from linear gas cells.

5.2 Comparison of Best Results

The maximum transport velocities with a half distance greater than 0.5 m were found to be lower for the lighter masses than those for heavier masses due to a larger contribution of the slipping mode. The data shown in Figure 5.13 verifies that the maximum transport velocities for Rb^+ are greater than that for K^+ ions. The maximum ion transport velocity decreases with ion mass because lower wave amplitudes are able to efficiently transport lighter ions. However, these measurements demonstrate the transport of the ions at much higher velocities with the ion surfing method than with the traditional method. Given a

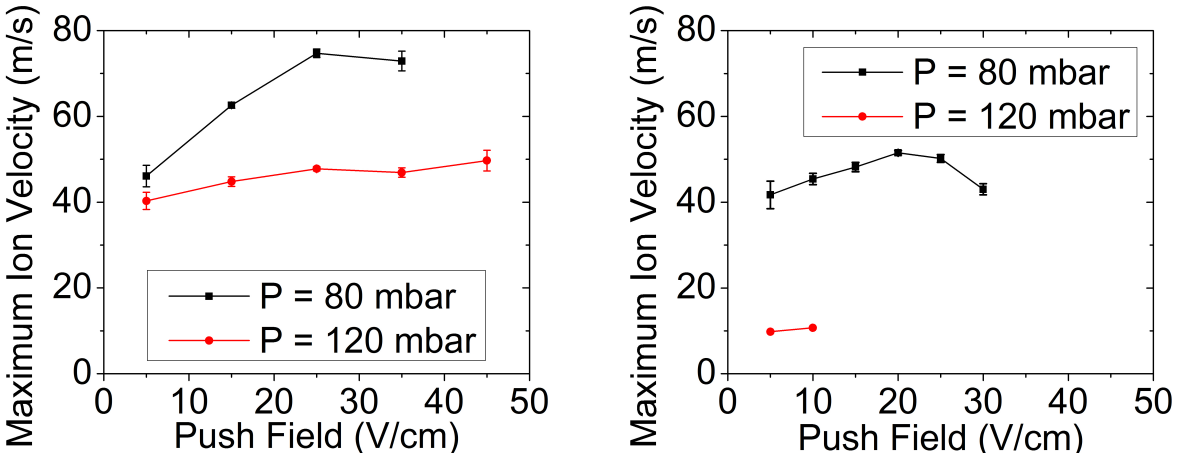

Figure 5.13: Maximum ion transport velocities with a half distance greater than 0.5 m as a function of push field. Left: Experimental results of Rb^+ ions at buffer gas pressues of 80 and 120 mbar. Right: Experimental results of K^+ ions at the same buffer gas pressures [12].

DC drag field of 10 V/cm, the ion velocites are calculated to be 27 m/s and 18 m/s for 80 mbar and 120 mbar, respectively. As shown in 5.13, ion transport velocites of 50-75 m/s are obtainable for Rb^+ ions within that pressure range, and K^+ ions can be transported at ~50 m/s at 80 mbar. Combined with the advantages of a simpler circuit, the ion surfing method appears to be the better method for a number of reasons for ion transport. However, the carpet prototype discussed in this chapter had a linear geometry. Measurements with a semi-circular geometry RF carpet are needed to show that these results can be extended to a carpet shape suitable for the cylindrical symmetry of the cyclotron gas stopper. Such a prototype was built and tested, and the results are presented in the following chapter.

Chapter 6

Circular Prototype Measurements

The final set of ion transport measurements were conducted with the semi-circular RF carpet prototype, shown in Figure 6.1. The semi-circular shape was chosen to model the geometry of the cylindrical cyclotron gas stopper. This chapter presents the results of ion transport efficiency and velocity measurements performed with this carpet as well as ion-jumping experiments in which the ions were collected on a collection pad below the center of the radial carpet.

6.1 Carpet Details

The carpet was 47 cm by 42 cm in size with the same pitch and γ as the linear prototype RF carpet tested in Chapter 5 (a = 0.375 mm, $\gamma = 0.67$). The inner radius was 2.5 cm. Similar to the previous carpets, the semi-circle carpet was manufactured by Innovative Circuits, Inc. [71]. The carpet traces were divided into two sections, an inner section of radius = 29 cm and an outer section that extends from r = 29 cm to 40 cm. Splitting the carpet into two sections would allow the carpet to be driven with two RF circuits, each connected to approximately

half of the total capacitance. During the design process, the capacitance of the carpet was calculated with the program FastFieldSolvers [72] and the result was relatively large (∼5 nF). The measured capacitance of each section was in fact found to be large (2.6 nF inner segment, 2.26 nF outer segment), and only the inner section of the carpet was driven with the existing RF circuit, and a high (> 6 MHz) RF frequency was achievable. The decision was made to reduce the area of the final RF carpets for the cyclotron gas stopper from a quarter circle with a radius 40 cm to a one-sixth circle of radius 47 cm for construction and support considerations and to also reduce the capacitance. Therefore, the outer region of the carpet was not needed to test ion transport from one RF circuit region to another, and only the inner region region was used for the measurement results presented in the following sections.

6.2 Experimental Results

As before, the position of the ion source relative to the collection pad was determined from photographs of the ion source taken at various locations over the carpet. The photographs were printed, and the scale of each photograph was calculated from carpet features of known size. The scale was then used to compute the ion source to collection pad distance. The set of data for the ion source position was fit as a function of the actuator setting.

The initial velocity measurements for seven positions along the carpet yielded the non-linear results as shown in Figure 6.2. All measurements were taken with 1 nA of ion current incident on the carpet unless otherwise specified. A linear fit to these data was not reasonable. The variation of the ion velocity across the carpet is likely due to the change in the RF amplitude along the length of the carpet. The RF amplitude varied nonlinearly from 53

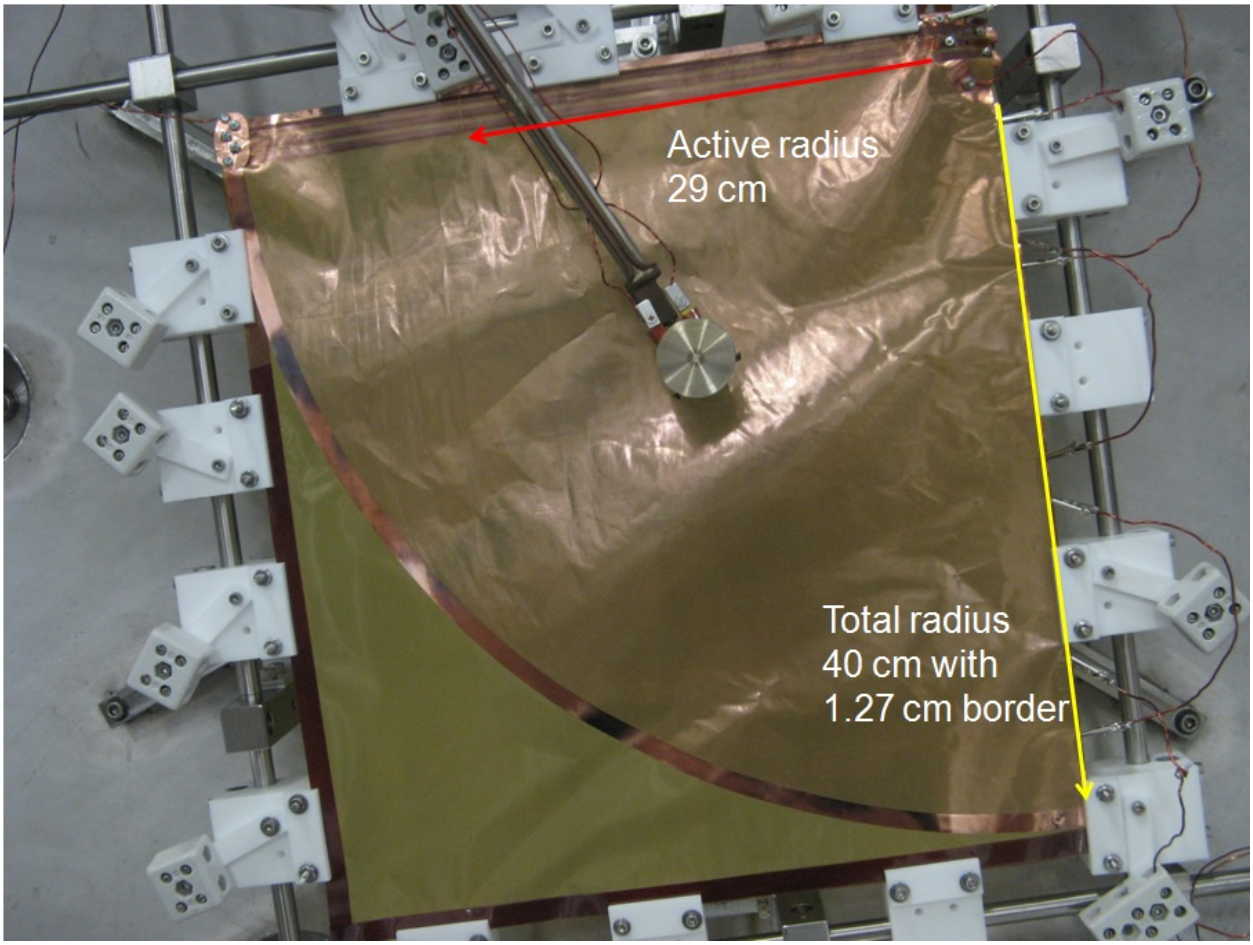

Figure 6.1: Photograph of the semi-circular RF carpet prototype mounted in the test chamber. The four bus bars that supply the RF and wave signals for each phase are visible along the upper edge. The radius of the inner, "active" area and the total radius of the carpet are indicated.

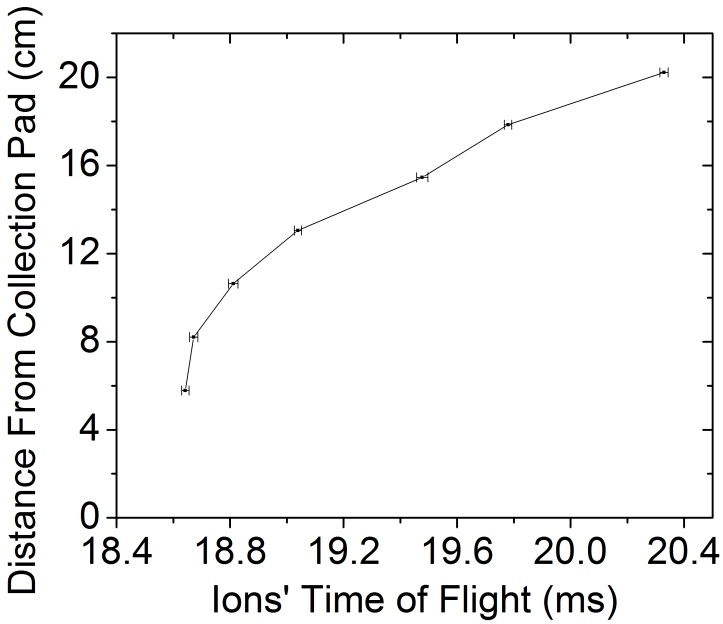

Figure 6.2: Transport distance as a function of the ions' time of flight for Rb^+ ions at 80 mbar buffer gas pressure, 25 V/cm push field, 8.38 MHz and 65 amplitude RF signals, and 4.99 V amplitude and 90 m/s traveling wave.

V to 70 V (a change of 32%) as the radius of the carpet increased, with a RF amplitude of ∼65 V at half the radius. The RF amplitude was shown to affect the ion velocity with the linear carpets where the ion velocity increased with decreasing RF amplitude. The results of ion velocity simulations conducted with the Surf2D code for nearly identical conditions did exhibit the trend of increasing ion velocity with decreasing RF amplitude shown in Figure 6.3. Thus it was decided to perform velocity measurements at five source positions at radii greater than 10.6 cm, in the linear region of Figure 6.2. The central value of 65 V will be considered as the RF amplitude in the following experimental results, and a uniform RF amplitude was set to 65 V in simulations.

The reproducibility of the velocity measurements was checked by repeating a series of measurements on two different days. A sample of the results is shown in Figure 6.4. The second set of measurements was taken three days after the first set under nearly identical

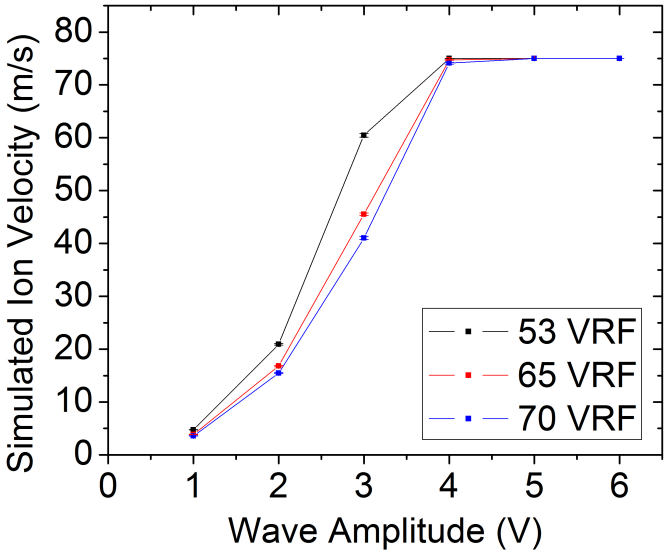

Figure 6.3: Surf2D simulation results of ion velocity at three RF amplitudes corresponding to the values at the beginning, middle, and end of the RF carpet. Parameters are identical to those of Figure 6.2 except the wave velocity is the slightly lower value of 75 m/s. The motion of forty ions were simulated for each data point, and the error bars calculated from the standard deviation of the ion velocity are small and not easily visible.

conditions. A small difference in the wave amplitude was noted between the two measurements and was due to retuning of the wave amplitudes. The reproducibility of the results was found to be good, especially at the lower wave amplitudes. The weighted average was taken of the differences in ion velocity for each pair of similar wave amplitudes, and the average difference was small, less than 2 m/s.

The results presented in this chapter cover K^+ ion transport. No Rb^+ experimental results are included due to large fluctuations observed in the ion source current and noise from the source switching signal during the series of Rb^+ measurements. The fluctuations in the ion source current and noise induced by the switching signal were fixed prior to the K^+ experiments. The Rb^+ measurements were not repeated because the test chamber was needed to develop other cyclotron gas stopper equipment.

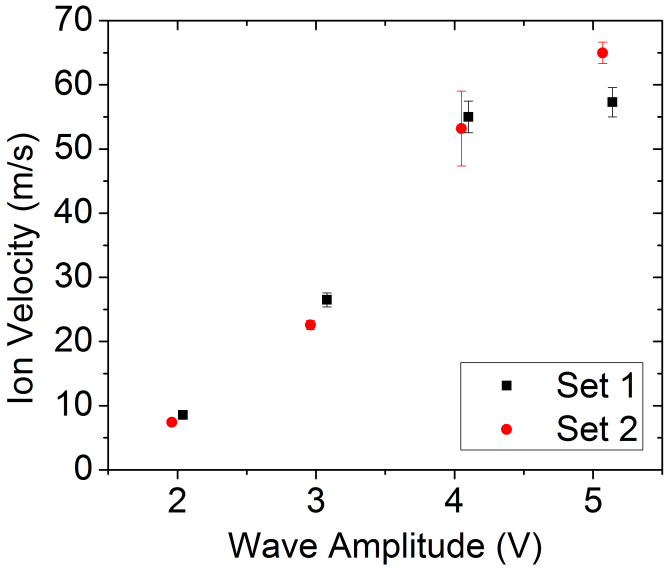

Figure 6.4: Experimental results of wave amplitude scans of ion velocity taken on two different days (Set 1 on 8/24/2012, Set 2 on 8/27/2012). Parameters: a = 0.375 mm, $\gamma = 0.67$, Rb^+ ions, 80 mbar buffer gas pressure, 5 V/cm push field, 8.38 MHz and 60 V amplitude RF, and 75 m/s wave velocity.

6.2.1 Potassium Ion Transport Results

The collection efficiency as a function of distance for K^+ ions is shown in Figure 6.5 under conditions that were similar to those for the measurements taken with the linear prototype carpet (see Figure 5.9). Although the Rf frequency and amplitude were different for the two sets of measurements, similar transport efficiences are expected as a function of wave amplitude as shown in Figure 6.6. The half distances were determined from a fit of Equation 5.1 to each data set, and the results are compared to those from the linear prototype results in Table 6.1.

The experimental linear carpet transport efficiency results were found to be better than the semi-circular prototype results by at least a factor of three. The Surf2D simulation results for the fraction of ions transported over 10 cm for the experimental conditions of

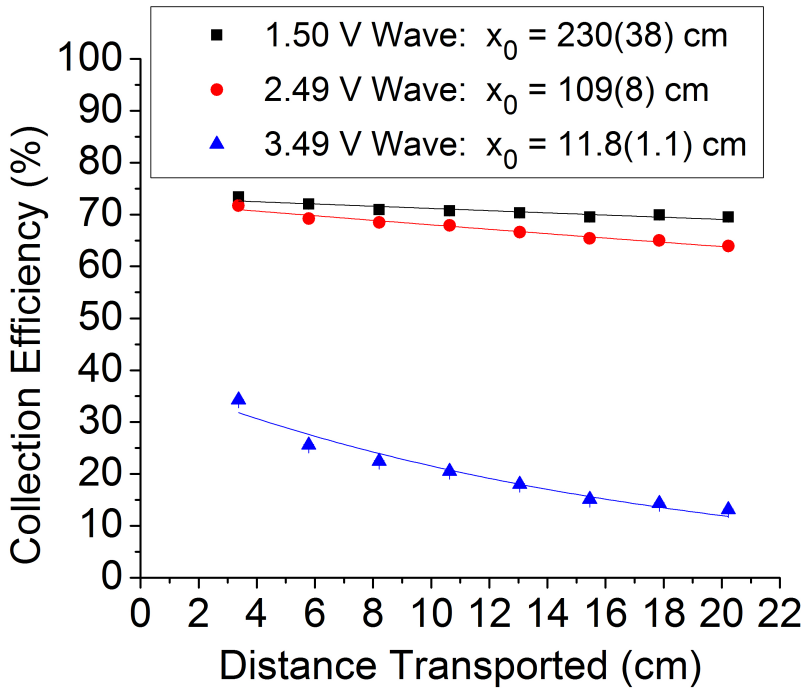

Figure 6.5: Collection efficiency as a function of the distance traveled by K^+ ions at three different wave amplitudes. The solid lines represent the best fit of Equation 5.1 to the data, and the half distances, x_0, are listed on the graph. Parameters: a = 0.375 mm, = 0.67, 80 mbar, 20 V/cm push field, 8.47 MHz RF frequency, 65 V RF amplitude, and 60 m/s wave velocity.

Table 6.1: Comparison of the half distances for the transport of K^+ ions by the linear and semi-circular carpet protoypes under similar conditions. The uncertainty obtained from the fit is indicated in parenthesis. Constant parameters: a = 0.375 mm, $\gamma = 0.67$, 80 mbar buffer gas pressure, 20 V/cm push field, 60 m/s wave velocity.

Wave Amplitude	Half Distance Linear Prototype 6.8 MHz, 75 V RF	Half Distance Semi-Circular Prototype 8.47 MHz, 65 Vrf	Half Distance Ratio Circular/Linear
1.5 V	722(58) cm	230(38) cm	0.32
2.5 V	358(14) cm	109(8) cm	0.30
3.5 V	114(2) cm	11.8(1.1) cm	0.10
4.5 V	21.21(8) cm	-	

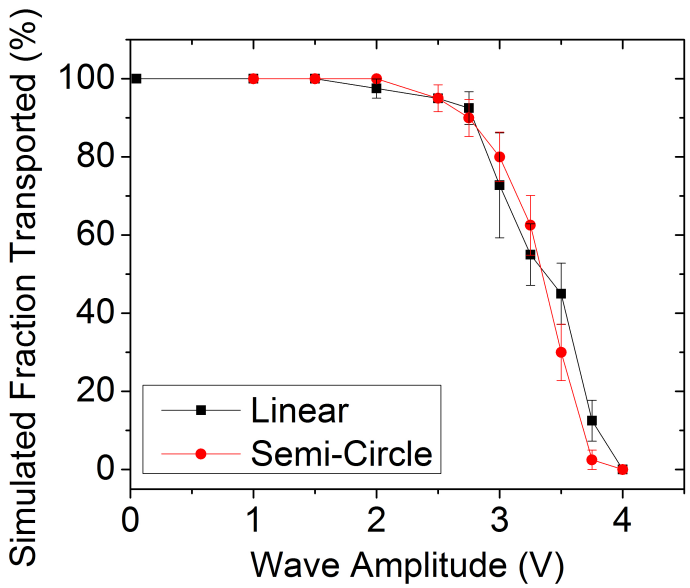

Figure 6.6: Comparison of Surf2D simulation results of the fraction of K^+ ions transported 10 cm for the parameters of the linear and semi-circular carpet measurements shown in Figures 5.9 and 6.5, respectively. Constant parameters: a = 0.375 mm, $\gamma = 0.67$, 80 mbar buffer gas pressure, 20 V/cm push field, 60 m/s wave velocity. RF variables: 6.8 MHz and 75 V for the linear carpet, 8.47 MHz and 65 V for the semi-circular prototype.

both Figure 5.9 and 6.5 are shown in Figure 6.6. The excellent simulated transport results at 1.5 and 2.5 V agree with the experimental results for both carpet prototypes. At 3.5 V wave amplitude, the simulation results over-predict the rate of ion losses for both prototypes (∼60% of ions lost over 10 cm in the simulation results, as compared to ∼10% ion losses in the experimental results). These results will have to be taken into consideration when predicting the performance of the RF carpets for the cyclotron gas stopper since the simulated transport efficiencies may not agree with experimental results, particularly at high wave amplitudes where ion losses are significant.

The maximum ion velocities obtainable for a given wave velocity and with a half distance greater than 0.5 m are shown as a function of push field in Figure 6.7. The wave amplitudes necessary to obtain the ion veloicities are shown in Figure 6.8. The maximum obtainable

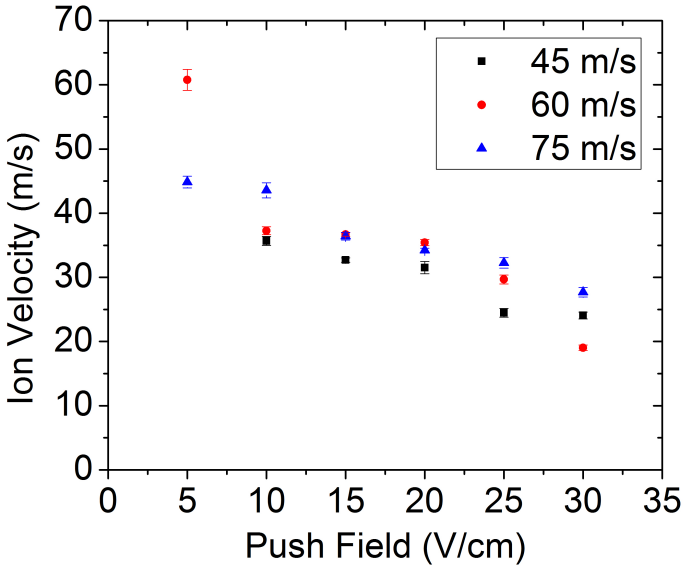

Figure 6.7: Experimental results for the maximum ion velocities obtainable for a given wave velocity with a half distance greater than 0.5 m shown as a function of push field. The wave amplitudes for the data are shown in Figure 6.8. Additional parameters: a = 0.375 mm, γ = 0.67, K^+ ions, 80 mbar buffer gas pressure, 8.47 MHz and 65 V

ion velocity appears to saturate at the higher wave velocities. As the push field is increased, the maximum obtainable ion velocities decrease. At push field magnitudes of 10 V/cm or higher, the ions do not achieve locked mode transport velocity, and increasing the wave velocity does not result in significant gains in transport time. Locked mode ion velocity was observed only at the lowest push field value of 5 V/cm.

Recall that the ions are forced closer to the carpet surface as the push field is increased. To maintain transport efficiencies with a half distance greater than 0.5 m, the wave amplitude must be decreased so that the ions are carried across the carpet surface in a shallower wave pocket. This trend is observed for all of the wave velocities shown in Figure 6.8, and the decrease in wave amplitude for the 60 and 75 m/s data follows a roughly linear trend.

The highest maximum velocity at each push field shown in Figure 6.7 and the corresponding wave velocity are shown in Figure 6.9. The data from the 120 mbar experiments

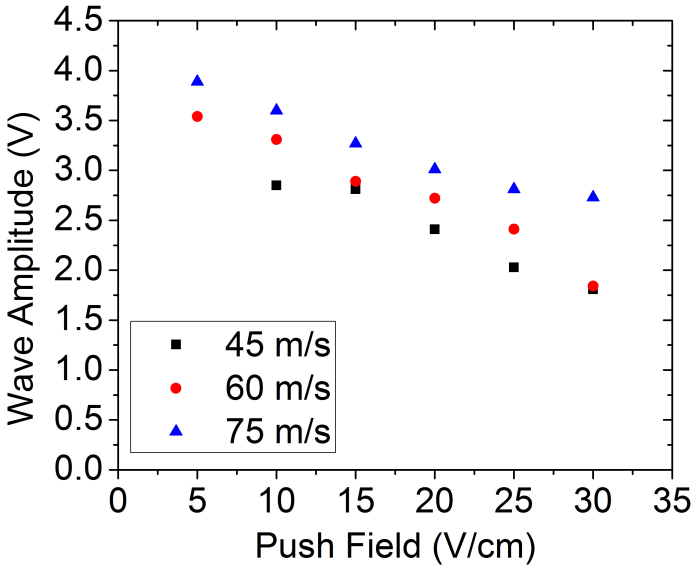

Figure 6.8: Wave amplitudes used to obtain the maximum velocities shown in Figure 6.7.

are also included. The experimental results were compared to Surf2D simulation results shown in Figure 6.10. During the experiments, the lower limit of the fraction of the ions transported was set to ~90% for a distance of 10 cm. The left axis of each set of simulation results corresponds to the fraction of the ions transported over 10 cm (solid black squares) and the ion velocity is shown along the right axis (open blue triangles).

For the maximum velocity at 80 mbar and 5 V/cm, good agreement was observed of the experimental value of 60 m/s shown in Figure 6.9 to the simulated ion velocity of 56 m/s at 90% of ions transported over 10 cm shown in Figure 6.10 (top). However, the simulated ion velocity at the efficiency limit is greater than the experimental value for most of the data (80 mbar, 10-25 V/cm values and both 120 mbar maximum velocities). An example of the overestimation is shown in Figure 6.10 (middle). The simulation model predicts an ion velocity of 40-45 m/s, yet the experimental value is only 35 m/s. The simulation results for the experimental conditions of the highest ion velocity at 30 V/cm are displayed

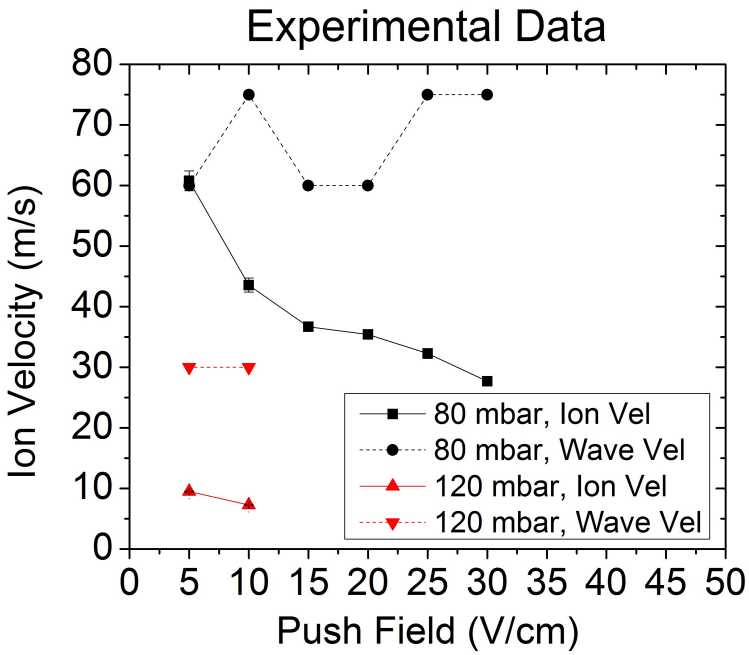

Figure 6.9: The maximum ion transport velocities with a half distance greater than 0.5 m (∼90% transport over 10 cm) for K^+ ions. The dashed lines indicate the corresponding wave velocities.

in Figure 6.10 (bottom). At the highest push field, the deduced velocity of 28 m/s is greater than the ion velocity taken from the simulations, 9.5 m/s. Unfortunately, the Surf2D simulation results did not consistently agree with the experimental data, and the observed trends were not reproduced. One possible explanation for the discrepancy is that a lower wave amplitude was required in order for the ions to be transported successfully over the lower (53 V minimum) RF amplitude region of the carpet, which caused a lower ion velocity. The simulation results also predict that lower wave amplitudes are necessary to obtain 90% transport efficiency over 10 cm as compared to the wave amplitudes of the experimental results. This implies that the ion-buffer gas interaction may need to be adjusted in the simulations to reduce collisions. Experimental tests will have to be performed to determine the optimum operating conditions of any future RF carpets, including those designed for the cyclotron gas stopper.

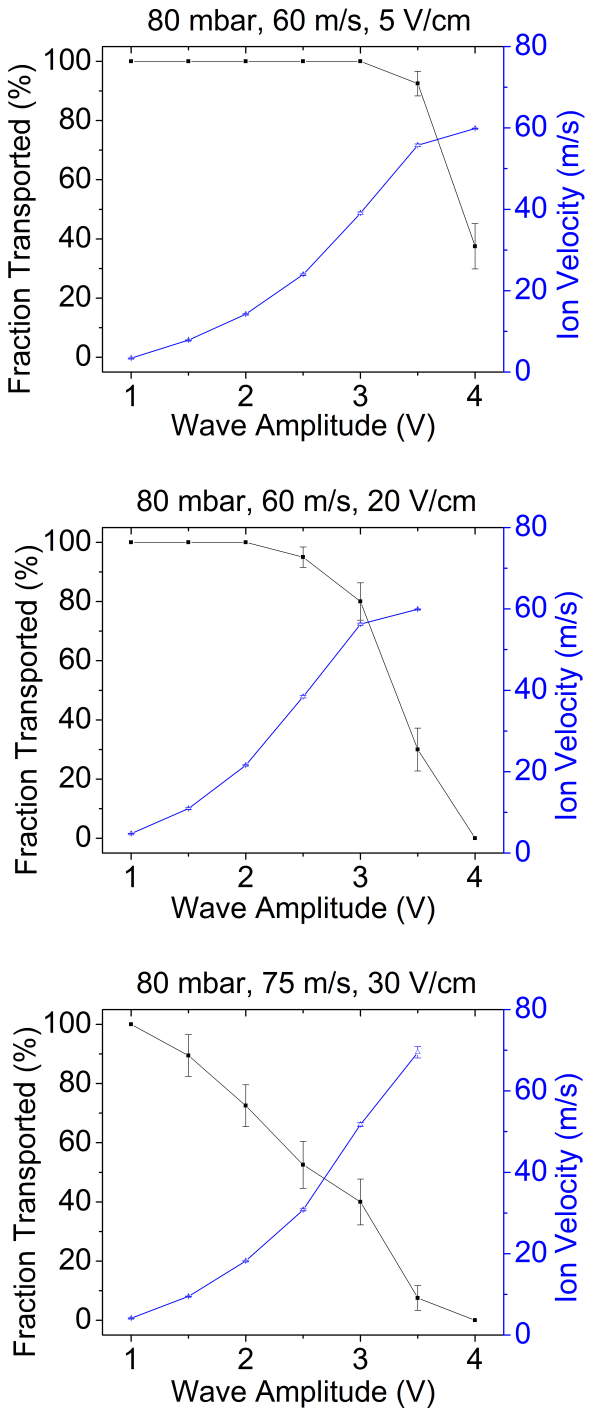

Figure 6.10: Surf2D ion transport efficiency results over 10 cm (black squares) and velocity results (blue triangles) as a function of wave amplitude. Experimental conditions are simulated as indicated, and the approximate maximum ion velocity can be determined for a given efficiency. Common parameters: a = 0.375 mm, $\gamma = 0.67$, 8.47 MHz and 65 V. The wave amplitudes for the experimental results are shown in Figure 6.8.

6.2.2 Comparison of Linear and Semi-Circular Prototype Best Results

The aforementioned best K^+ ion experimental results for the ion velocity with a given efficiency are compared in Figure 6.11 with the results under similar conditions for the linear prototype in Chapter 5. Almost all of the maximum ion velocities with a half distance greater than 0.5 m for the linear carpet are larger in magnitude than those deduced for the semi-circular carpet. As previously discussed in Section 6.2.1, the semi-circular carpet has shorter half distances, and lower transport efficiency, than the linear prototype. A lower wave amplitude was required to combat the ion losses, and the lower ion velocities of the semi-circular carpet results are a consequence of meeting the efficiency limit. Since smaller amplitudes are also needed as the push field increases, the observed decrease in ion velocity with push field is expected. An exception to the superiority of the linear carpet results occurs at 5 V/cm and 80 mbar. The highest ion velocity of all the K^+ ion measurements, 60 m/s, was observed at 80 mbar.

The maximum ion velocities achieved at 120 mbar are similar for both carpets, and the wave velocities needed to reach the maximum ion velocity for operating pressures of 80 and 120 mbar are identical (red points in Figure 6.11). The semi-circular prototype transport times for a distance of 20 cm are ∼3-7 ms at 80 mbar and ∼20 ms at 120 mbar. Once again, the transport times are excellent, and a large reduction in extraction times for the cyclotron gas stopper as compared to previous and current beam thermalization devices should be possible.

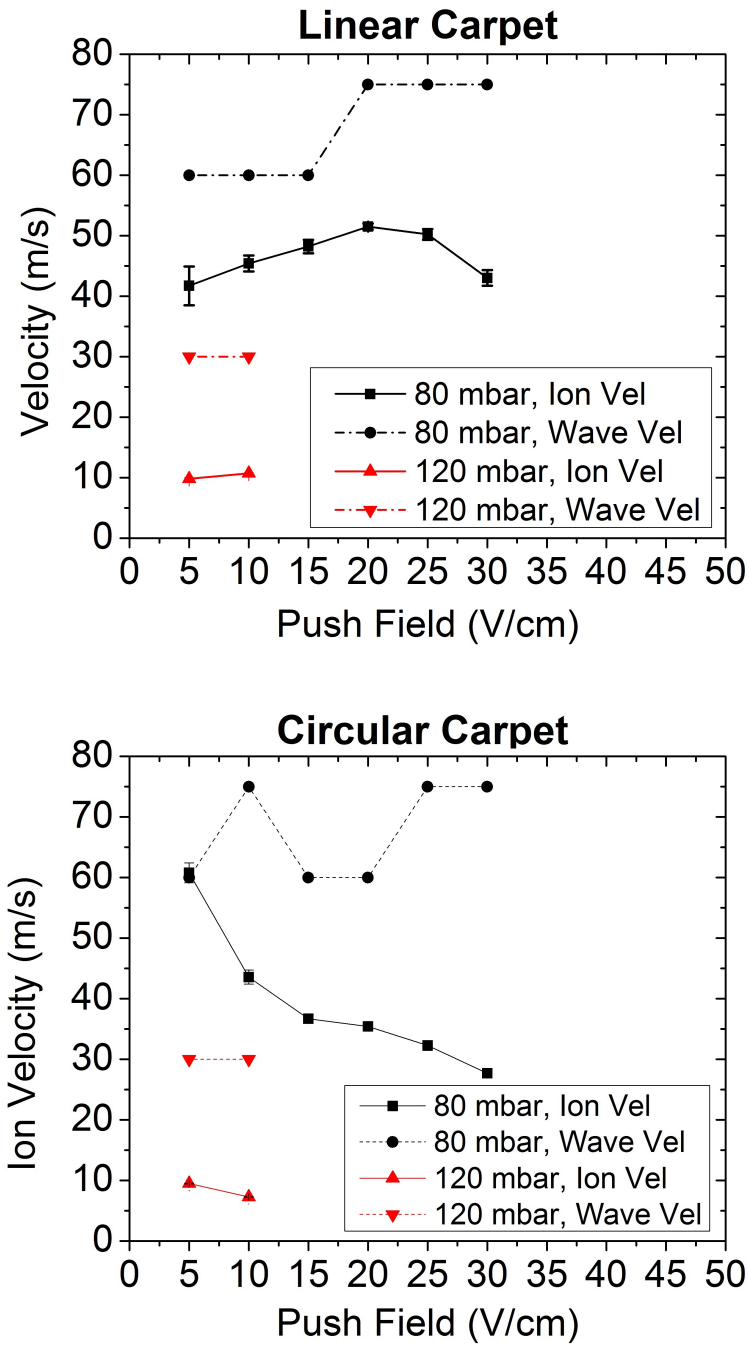

Figure 6.11: Comparison of the maximum ion velocities obtainable with a half distance greater than 0.5 m. Above: Best results for K^+ ions (see Figure 5.12). Below: The analogous semi-circular prototype results (see Figure 6.9.)

6.3 Rubidium Ion-Jumping Results

The capacitance of a circular geometry RF carpet changes dramatically as the radius decreases due to the decreasing size of the electrodes. A small RF carpet with a rigid substrate will be placed in the center of the cyclotron gas stopper a short distance below the large area Kapton-substrate RF carpets studied in this work. Ion jumping from an upper carpet to a smaller carpet was done by Pang with drag field RF carpets [10]. This section summarizes the test results for Rb^+ ions jumping from the semi-circular carpet to a single collection pad below the carpet.

To deduce the jumping efficiency, the following procedure was employed. First, the collection pad used in the previous experiments was removed and replaced with a copper collection pad placed 1.2 cm below the carpet, as shown in Figure 6.12. The ion source was positioned equidistant (12.95 cm) from the edge of the carpet nearest the collection pad and the outer segment. Both the outer segment and collection pad were connected to picoammeters, and a bias voltage was applied to the collection pad. The efficiency of the ion transport was measured, but now with the collection pad placed below the carpet. The wave velocity was then reversed, and the efficiency was measured with the outer carpet segment acting as a collection pad. The jumping efficiency was taken as the ratio of the 12.95 cm transport efficiency inward to that of the 12.95 cm transport efficiency outward. A sketch of the experimental setup is shown in Figure 6.12. Each efficiency measurement was repeated two times for various operating conditions discussed in detail below.

The buffer gas pressure, push field, and pull field were varied for these measurements. The pull field is the difference in voltage between the carpet (at ground) and the collection pad divided by the separation of 1.2 cm. A wave velocity of 75 m/s was chosen since this

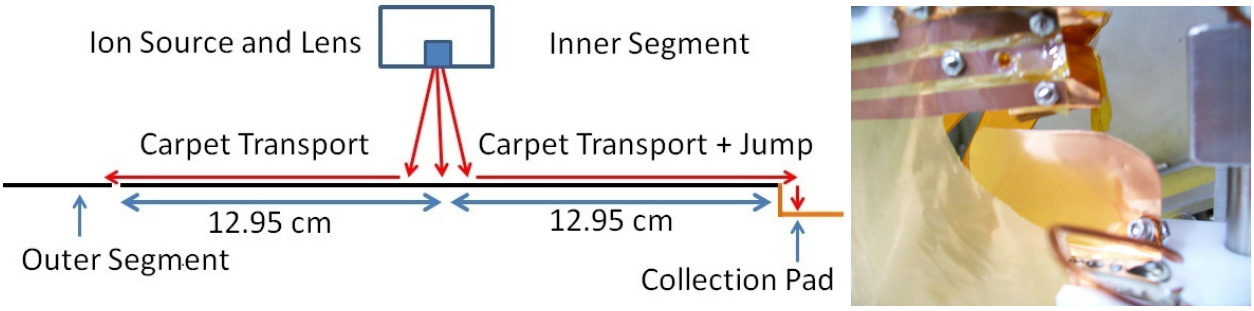

Figure 6.12: Left: Cartoon of the cross section of the semi-circular prototype during ion jumping measurements. The carpets are indicated by black lines and the collection pad by orange lines. The source is located over the midpoint of the inner segment. The collection pad is 1.2 cm below the large carpet. Right: Photograph of the jumping region and collection pad.

value had some of the best velocity and efficiency results previously discussed. A wave amplitude of 1.2 V was used to optimize transport efficiency, and any observed losses could be attributed to the ion jumping.

The ion jumping results at 80 mbar buffer gas pressure are shown in Figure 6.13 (above) as a function of the pull field for various push fields. At a push field of 5 V/cm and pull field of 10 V/cm, nearly all of the ions were successfully transported from the carpet to the collection pad. At the higher push fields of 15 and 25 V/cm, the jump efficiency appears to saturate at 80%. As the push field increased, higher pull fields were required to reach the saturated efficiency. The 20% ion loss likely occurs on the last carpet electrodes since the RF field is asymmetric at the last electrode. The effective potential at the last electrodes should decrease due to the field asymmetry, and the higher push fields appear to be strong enough to overcome the repelling force and cause significant ion losses. In order to combat these ion losses, the RF voltage could be decreased over the last few electrodes.

Similar results are shown for 120 mbar gas pressure in Figure 6.13 (below). The lowest push field of 5 V/cm yielded the best results, near 90% jumping efficiency. Similar to the

results at 80 mbar, the efficiency is near the maximum value at a pull field of 10 V/cm. The efficiency reached a maximum of $\sim$65% at the higher magnitude push fields, and again increased pull fields were required to realize a given efficiency. The results at both buffer gas pressures demonstrate that a low push field may be desirable for the center of the cyclotron gas stopper in order to optimize the jumping efficiency.

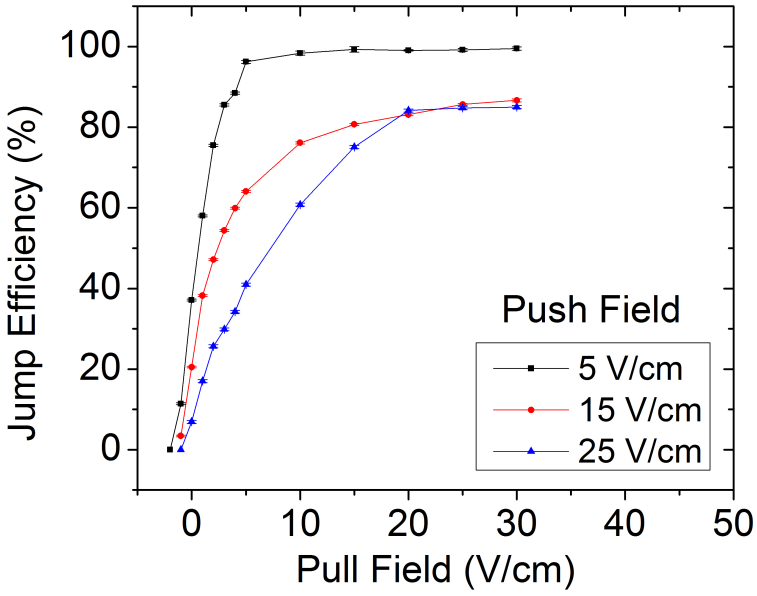

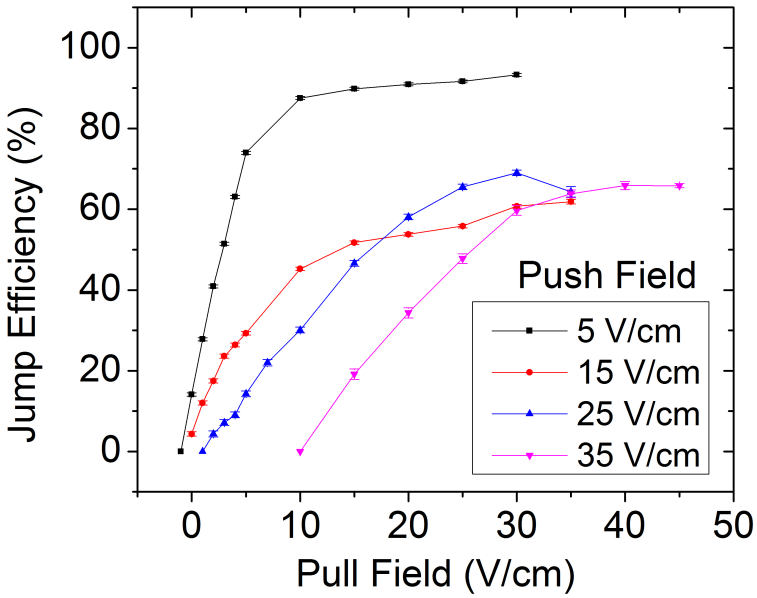

Figure 6.13: Jumping efficiency as a function of pull field for Rb^+ ions. Above: Experimental results at 80 mbar and 3 different push fields. Below: Similar results at 120 mbar and four different push fields. Common parameters: a = 0.375 mm, $\gamma = 0.67$, 8.47 MHz RF frequency, 65 V RF amplitude, 75 m/s and 1.2 V amplitude traveling wave.

Chapter 7

Outlook and Conclusions

The status of the design and fabrication of the RF carpets for the cyclotron gas stopper (CGS), including the circuit and mounting frame, is presented in the first section of this chapter. The second section concludes this dissertation with a short summary of the ion transport results and suggestions for additional improvements and tests that could further improve the ion surfing method of transporting ions with RF carpets.

7.1 Proposed RF Carpet Design for the Cyclotron Gas Stopper

The designs of the RF carpets and their related equipment to be used with the CGS are in the final stages in 2013. The following sections are used to discuss the implications of the prototype RF carpet tests represented here on the design and fabrication of the RF carpets, mounting frame, and ion surfing circuit for the CGS.

7.1.1 RF Carpet

The RF carpets that will be used in the CGS have been ordered from Flexible Circuit Technologies [73]. Due to the difficulty of driving two segments of the semi-circular prototype at a relatively high RF frequency (> 6 MHz, see Section 6.1), the decision was made to cover the circular, $\sim$1 m diameter ion transport area with six RF carpets with a radius of 47 cm instead of the previously proposed and tested quarter circle carpets with a radius of 40 cm. The capacitance of one of the one-sixth circle carpets was calculated to be 2 nF, and a summary of the capacitance calculation and carpet design details is provided in Appendix C. The capacitance of the inner segment of the semi-circular prototype discussed in Chapter 6 was 2.6 nF; therefore, the carpets designed for the CGS should be able to be tuned to a higher frequency (> 8.5 MHz) than those in the present work if necessary.

The six carpet segments also match the symmetry of the six sectors of the pole steel of the CGS magnet. The pole steel is pictured in Figure 7.1 to give an impression of the geometry. The pitch of the CGS RF carpets in the ion transport region will be 0.467 mm with a γ of 0.73. In order to allow more space for the small carpet near the central exit of the CGS, the traces of the carpet at the border with the ion transport region will angle away from the exit region so that the substrate can be removed, as shown in Figure 7.2. The carpet pitch in the region of the angled traces is at the manufacturing limits of 0.125 mm trace width and 0.25 mm gap, and the traces remain 0.125 mm wide in the ion transport region but the gap increases to 0.342 mm. The calculated repelling force as a function of frequency for the CGS carpet pitch and γ was shown earlier in Figure 2.5 (below). The maximum repelling force is predicted to occur in the RF frequency range of 6-7 MHz.

The current design of the small central carpet is shown in Figure 7.3. The material type

Figure 7.1: Left: Photograph of the six sector magnet pole steel during assembly. Right: Photograph of the pole steel inside the vertical magnet yoke of the cyclotron gas stopper.

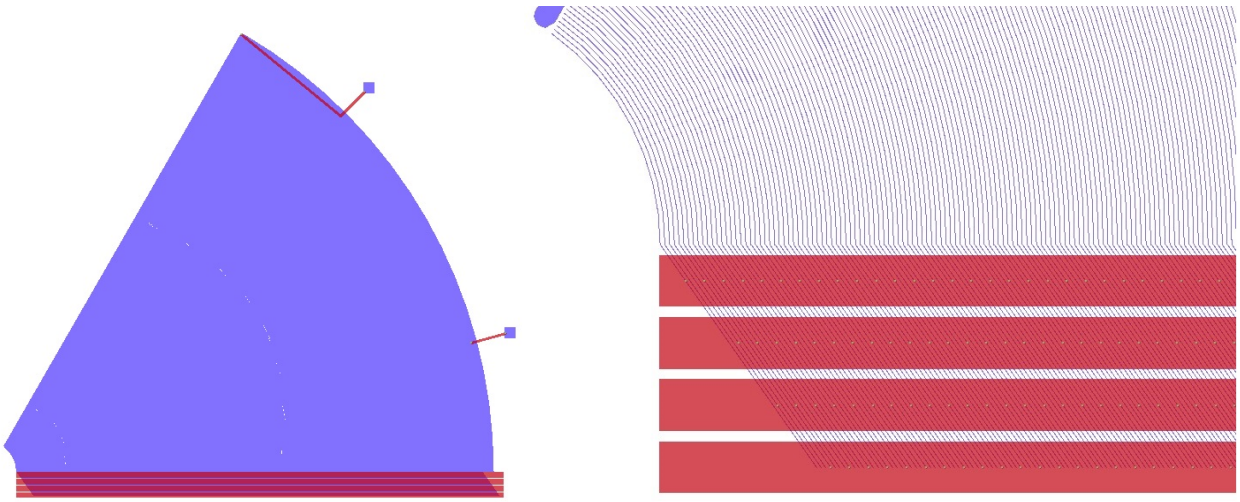

Figure 7.2: Design of the one-sixth circle RF carpets. The top layer is blue, the bottom layer is red, and the vias connecting the two layers appear as small white dots. Left: The full view of the RF carpet. A thin border exists along the top edge of the carpet, and a bumper is along the curved edge. The lower bus bars (in red) are 43.8 cm in length. Right: Close-up of the traces near the inner edge of the carpet and the beginning of the angled section of the traces. The bus bars are 0.51 cm wide.

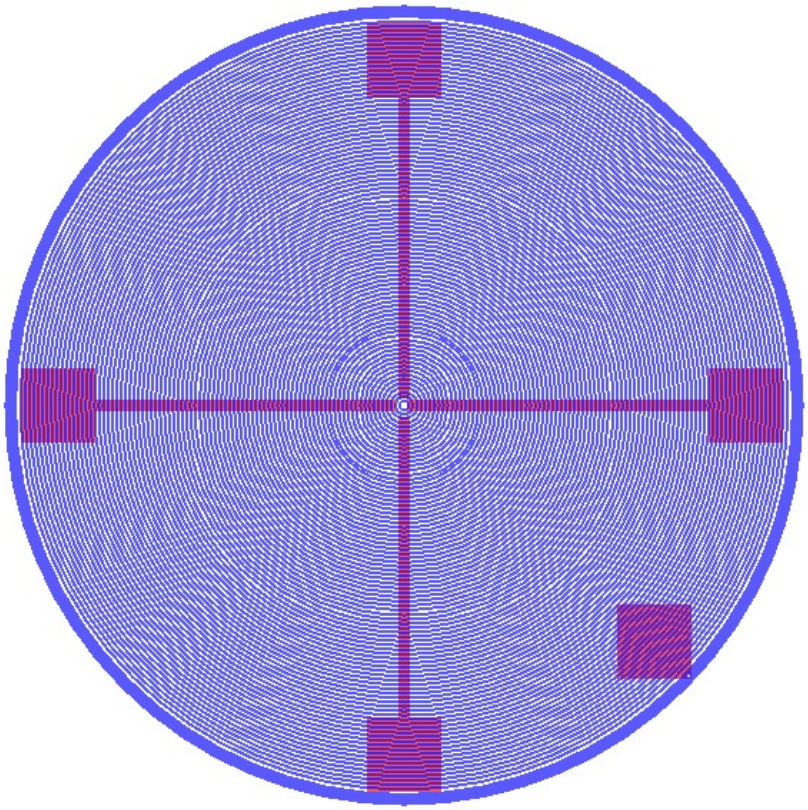

Figure 7.3: Design of the small RF carpet. The top layer is blue, the bottom layer is red, and the vias connecting the two layers appear as white dots. The diameter is 5.49 cm with an exit hole of 0.5 mm. The carpet pitch is 0.3 mm with $\gamma = 0.5$. The border around the carpet can serve as a bumper or as a collection pad.

and thickness of the substrate is still under consideration because the small carpet will form the boundary between the relatively high pressure of the buffer gas chamber ($\sim$ 100 mbar) and the lower pressure ($\sim$ 10 mbar) in the extraction region. The central hole will be 0.5 mm in diameter, and the total carpet radius will be 2.74 cm. The carpet pitch will be 0.3 mm with a γ of 0.5. The repelling force of the small carpet, as compared to the repelling force of the other carpets of this work, is again shown in Figure 2.5.

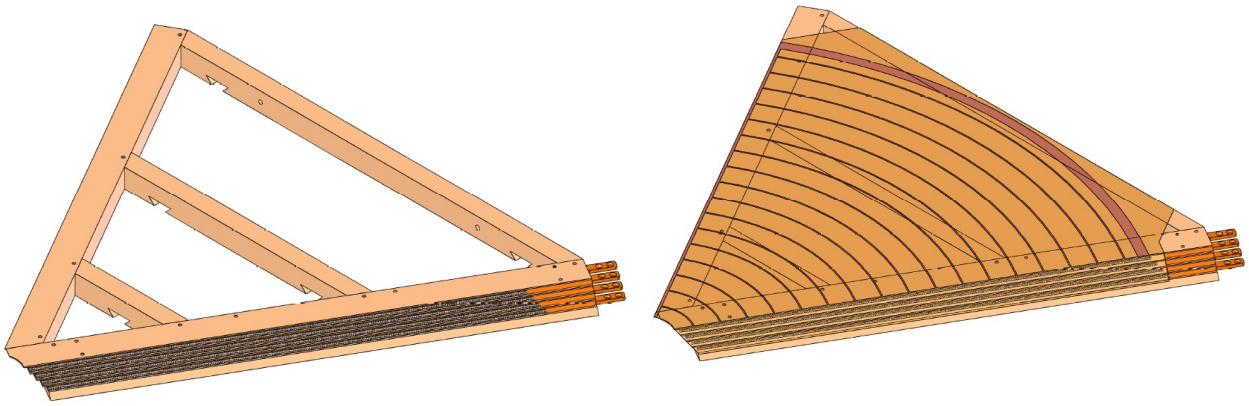

Figure 7.4: Mechanical drawings of the RF carpet mounting frame for the cyclotron gas stopper [14]. Left: One of six identical segments of the mounting frame. Right: The frame with an RF carpet attached to the top.

7.1.2 Mounting Frame

A six segment mounting frame was recently designed, and one section of the frame is shown in Figure 7.4 (left) without the RF carpet present. The frame with an RF carpet is shown in Figure 7.4 (right), and the straight lines under the curved traces indicate the position of the frame cross bars. Along the edge of the frame, the electrical bus bars on the carpet will come into contact with the solid bus bars of the frame. The constant contact of the bus bars along the length of the carpet will minimize changes in RF amplitude like those discovered during the semi-circular carpet prototype measurements (see Chapter 6). The Kapton-only (no copper traces) edge of one carpet will contact the region of the angled traces of the second carpet, and at the junction of the two carpets the edges will be clamped together. At the next junction of two frame pieces the second carpet's excess Kapton will be paired with the third RF carpet's region of angled traces, and so on, until the ring is complete.

7.1.3 Circuit

The circuit design for the CGS RF carpets is also nearing completion. Each of the six RF carpet sections will have its own RF generator. The wave signal will be supplied to all six RF carpets with one dual-channel arbitrary function generator (AFG). The two AFG output signals will be offset by 90 degrees, and each signal will be split with one signal going through a 180 degree phase shift before reaching the carpet.

Unlike the circuit used for the prototype tests, the transformer and variable capacitors will be located inside the helium gas volume of the CGS. Two circuits will be located in each pole steel valley, where the valleys are the thinner sections shown in Figure 7.1. The transformer cores will be open instead of ferrite. The variable capacitance will be achieved by adjusting the length of thin, coiled copper foil. Preamplifiers may be added to increase the maximum wave amplitude of the driven circuit.

7.2 Summary and Outlook

The ion surfing method [5] was shown to be a successful method for transporting ions in helium buffer gas. Transport efficiencies of near 100% over 30 cm were obtained for Rb^+ and K^+ ions at 80 mbar and for Rb^+ ions at 120 mbar. The ion velocities deduced for both ion species at 80 mbar and for Rb^+ at 120 mbar are higher than those determined using the drag field method. The ability to quickly transport ions through the buffer gas to the exit region of the CGS will result in fewer ion losses due to the radioactive decay of short-lived nuclei. At 80 mbar and a transport distance corresponding to the stopping radius of 0.35 m, Rb^+ ions were observed with velocities of at least 75 m/s, and were transported with an efficiency of $\sim$70%. For K^+ ions at 80 mbar and a transport distance matching the simulated

stopping radius of 0.2 m, ∼80% transport efficiency and 60 m/s ion velocity were achieved simultaneously. At the higher pressure of 120 mbar, Rb^+ ions were still observed to travel at velocities of ∼50 m/s, without a loss of transport efficiency. At 120 mbar, K^+ ions must trade speed for efficiency, but the transport times for a typical stopping radius distance and ∼80% transport efficiency are still only tens of milliseconds. These results, combined with the easier implementation of the method, prove that ion surfing is the prefered method for ion transport for the cyclotron gas cell.

In addition to the efficiency and velocity results, a wide parameter space was explored in simulations and the effects of changing each variable were found to qualitatively agree with experimental data. Important observations were the verification of both locked and slipping modes, the rise of wave amplitude required to attain locked mode with increasing wave velocity, and the strong mass-dependent effect of varying the pressure. The Surf2D code was found to reproduce the ion velocity results reasonably well. Finally, valuable experience and lessons learned were gained in circuit and carpet design, measurement procedures, and troubleshooting.

Potential future improvements to the ion surfing method include the development of methods to increase the available range of wave amplitudes (especially at higher wave velocities), investigation of smaller values of pitch as the manufacturing limits become smaller, and measurements with a wider range of ion masses. Unfortunately this work was not able to include sodium ion measurements due to a failure of the ion source (see Appendix B), but sodium ion tests with the CGS carpets are planned in the near future. The CGS is currently being assembled as shown in Figure 7.5, and within the next few years the advantages of ion surfing will benefit all experiments at the NSCL requiring thermalized radioactive isotopes.

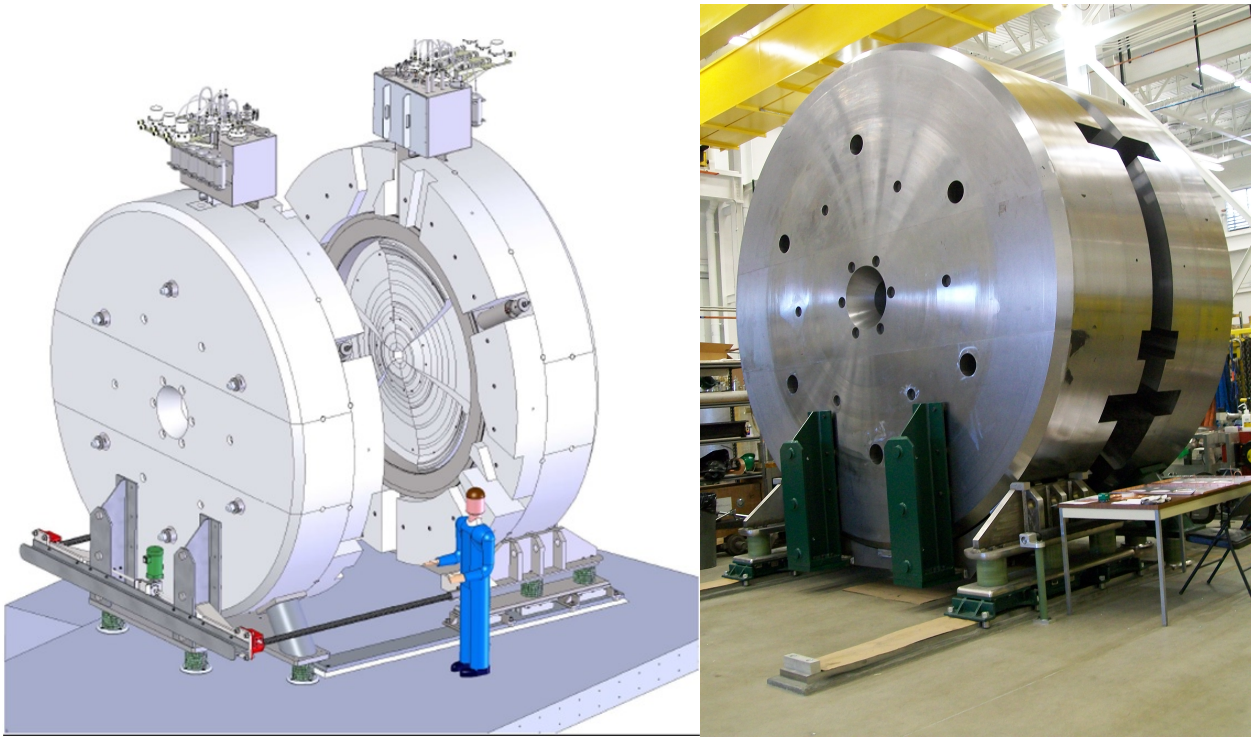

Figure 7.5: Left: Schematic of the cyclotron gas cell. Right: The cyclotron magnet yoke as of April 2013.

APPENDICES

Appendix A

Simulation Details

This appendix summarizes the studies conducted with SimION simulations to optimize the various operating parameters of the RF carpet. The effect of the grid unit size, calculation time step (which is determined by the trajectory quality), and exponential damping factor are presented in the following sections.

New SimION features available in version 8.1 should benefit simulations of RF carpets. One such feature is an adjustable grid unit size. The repelling potential created by the RF field exponentially decreases as the distance from the carpet electrodes increases. Smaller grid unit sizes near the carpet electrodes will allow better modeling of this potiential. Dielectrics can now be simulated, thus the carpet substrate itself could be added to the simulations by adding 1 mil of dielectric with a dielectric constant = 3.4 directly below the carpet electrodes. A relatively new development, fast scalable potential array (PA) files, was implemented in the ion surfing SimION simulations. Instead of calculating the field map and creating a PA file for each electrode, one potential can be mapped onto several electrodes, and this potential is contained in one PA file (for example, one PA file contained the RF signal potential, another

the push field potential, etc.). Less potenlial array files are read during a simulation, and the calculation time can be shortened by a factor of 10 to 40 depending on the reduction in number of PA files.

A.1 Grid Unit

Initial SimION simulations with hard sphere collisions were performed of the ion motion for drag field RF carpets. In order to ascertain that the grid unit size of these simulations was adequately small, a series of simulations was performed in which the maximum push field required to force ions into the carpet surface was determined under identical conditions for different values of grid unit size. The push field limit as a function of buffer gas pressure is shown in Figure A.1. The parameters are listed in the caption. At high pressure (p > 130 mbar) the grid unit size appears to have little effect. At the lower pressures, especially in the region of 25-80 mbar, the grid unit size can affect the calculated push field limit by over 10 V/cm. As a result of these simulations, a maximum grid unit size of 0.05 mm was chosen for all subsequent simulations. A grid unit of 0.0125 mm was used in the field maps solved by SimION for the Surf2D simulations, which resulted in 0.125 mm wide electrodes 10 x 2 grid units in size.

A.2 Exponential Damping Factor and Trajectory Quality

A time-dependent damping factor, F_t, can be included in SimION simulations that model the buffer gas with a viscous drag force. The factor is defined as:

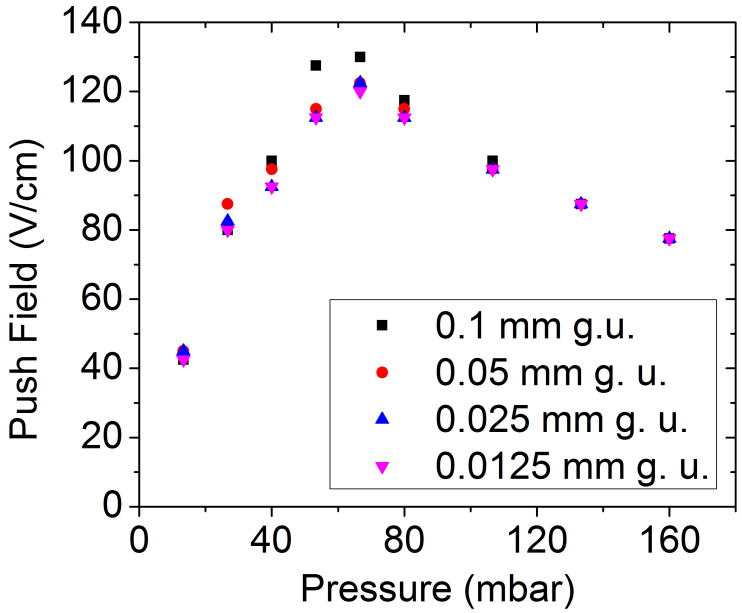

Figure A.1: The push field limit as a function of buffer gas pressure for various values of grid unit size. Parameters: a = 0.4 mm, $\gamma = 0.5$, 85 u singly-charged ions, 80 V RF amplitude, 2 MHz RF frequency, 3 V/cm drag field, 10 V/cm push field, and 20 ions flown at each data point.

$$F_t = \frac{1 - e^{-Dt_{step}}}{Dt_{step}} \tag{A.1}$$

where D is the damping factor calculated by Equation 2.6 and t_{step} is the calculation time step of the simulation. The time-dependent factor is used to determine the corrected acceleration, a_{corr}, of the simulated ion motion as follows:

$$a_{corr} = F(a - Dv) \tag{A.2}$$

The effect of the presence of this factor on the range of ion distances above the carpet was investigated at 200 mbar for several masses and values of trajectory quality (TQ). The TQ controls the time step of the simulations, and the time step decreases as the TQ increases.

The results are shown in Figure A.2. The minimum distance above the carpet surface correlates to the transport efficiency since as the distance decreases an ion is more likely to hit a carpet electrode. At the lower values of TQ (10 and 20), the calculated distance above the carpet is greater for the simulations conducted with the exponential damping factor. The simulated distance with the exponential damping factor converges as TQ increases to the distance without the factor. Since the exponential damping factor has little effect at the higher (and better) TQs, and its effect at the lower TQs is small (less than 0.05 mm change in distance above the carpet electrodes), the factor was omitted from subsequent viscous drag simulations.

The time step at which the Surf2D simulations would check for an ion-buffer gas atom collison was set by the user. In order to determine the value of this parameter, SimION simulations were conducted at various values of TQ. Nearly identical simulation results were found at various values of TQ $\geq$ 10. The time step of several values of TQ was determined by recording every time step during a few seconds of a simulation at a given TQ. The maximum and average time steps are shown in Table A.1. As previously mentioned, the Surf2D code was able to perform simulations at higher gas pressures (p $\geq$ 80 mbar) more quickly than SimION. A time step of 0.1 ns, less than the minimum value in Table A.1, the Surf2D simulations were able to perform the calcuations at least twice as fast as SimION simulations at a TQ of 10. (SimION simulations were conducted at TQ = 10 due to the faster calculation time as compared to simulations at higher TQ values, also shown in Table A.1, and the results were nearly identical to those performed with high values of TQ.)

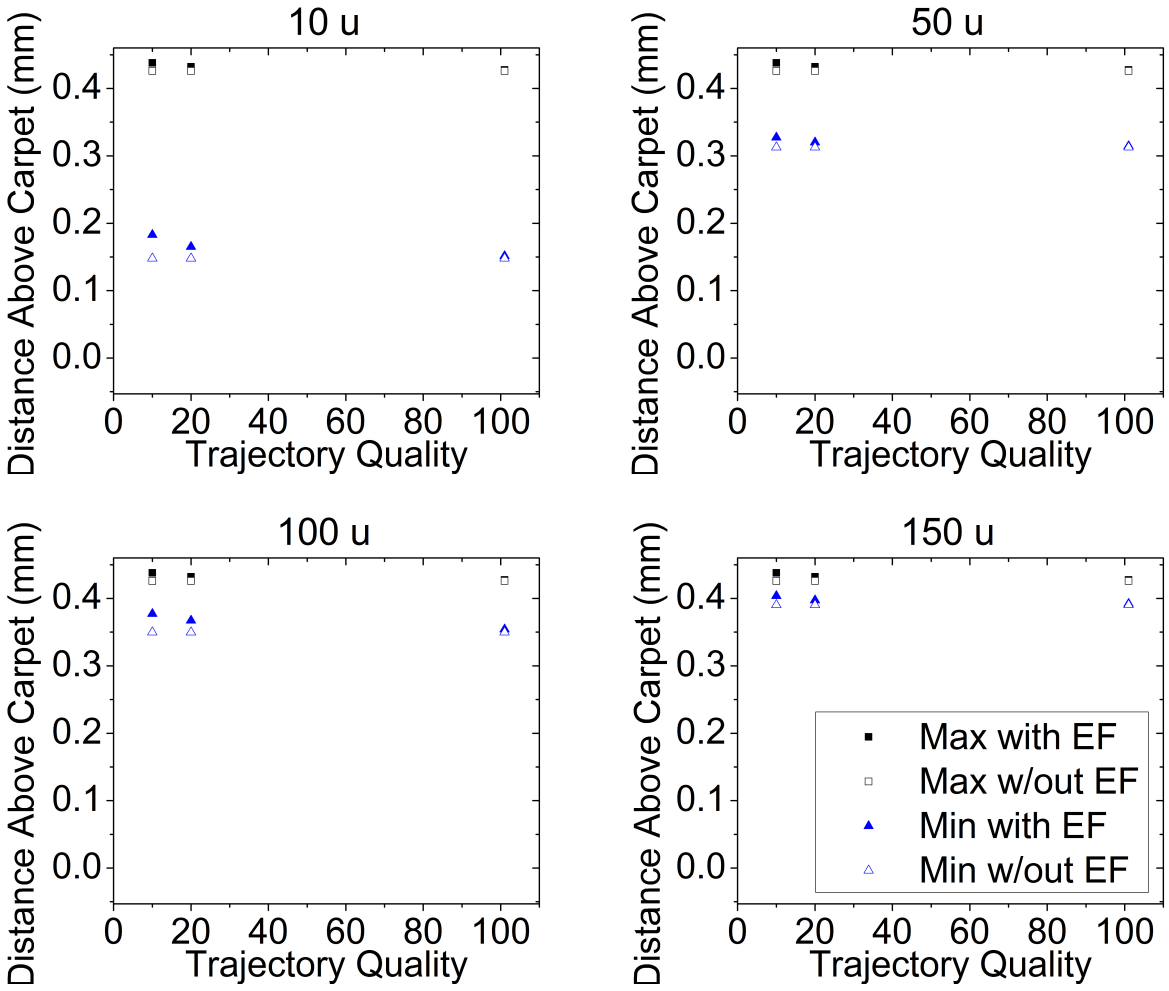

Figure A.2: Comparison of simulations with and without the exponential damping factor (EF) for four singly-charged ion masses. The maximum and minimum distances above the carpet are shown in order to illustrate the limits of the ion distance above the carpet electrodes. Parameters: a = 0.4 mm, $\gamma = 0.5$, 70 V RF amplitude, 4 MHz RF frequency, 3 V/cm drag field, 10 V/cm push field, 200 mbar, and 5 ions flown at each data point.

Table A.1: The average and maximum time steps for different values of trajectory quality. The time steps decrease as the TQ increases. Parameters: a = 0.4 mm, γ = 0.5, 150 u singly-charged ion, 100 V RF amplitude, 4 MHz RF frequency, 3 V/cm drag field, 10 V/cm push field, 200 mbar, and at least 400 recorded time steps. The calculation time is the real time required for an ion to move 1 cm.

Trajectory Quality	Average Time Step	Maximum Time Step	Calculation Time per Ion
	ns	ns	s
10	2.82	9.88	56
20	1.78	4.95	169
101	0.383	0.493	843
150	0.160	0.208	

Appendix B

Measurement Details

This appendix summarizes the procedure used to validate the composition of the ion sources. The results of the tests are also presented.

B.1 Ion Source Purity

The composition of the ion sources was checked with a SRS 300 Residual Gas Analyzer [74]. The RGA was attached to the upper left port (as viewed from the side opposite the door) of the RF carpet test chamber (see Section 4.1). At this position, the ion source at the end of the acuator arm could be aligned with the RGA entrance.

The filament of the RGA ionizies the residual gas. For measurements of ions that are already present (such as the ion source scans), the scans were taken with the filament off so that the residual gas would not be analyzed and included in the results. Scans were taken in both "filament enabled" and "filament by-pass" modes. The setting of the RGA upon purchase is the "filament enabled" mode, and during these scans the filament was off and no voltages were applied to the features at the input of the RGA. The RGA was modified so

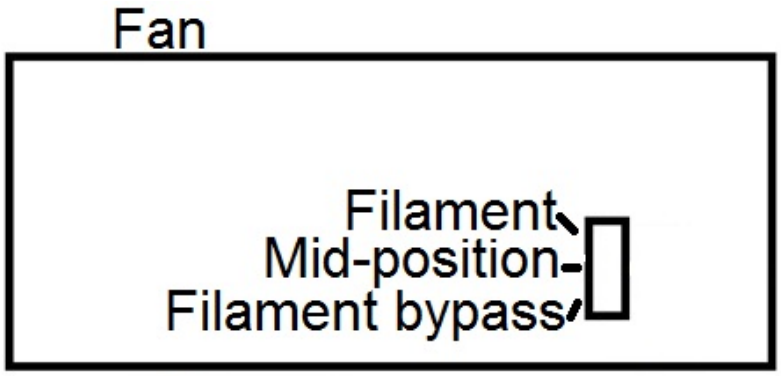

Figure B.1: Cartoon of the location of the switch that determines the mode of operation for the filament.

that the voltages of the input features (the focus plate, anode grid, and repeller grid) could be adjusted with the filament off. Before the modification, the aforementioned voltages could only be adjusted when the filament was on. This "filament by-pass" mode allowed the input voltages to be adjusted to focus more ions into the RGA. In either mode, enough ions were able to enter the RGA for a successful mass scan. In order to determine which mode the RGA is in, remove the electronics control unit (ECU) from the RGA and unscrew the top casing containing the fan. Inside a switch has been added. A rough sketch of the location and positions of the switch is shown in Figure B.1.

In order to take a mass scan of an ion source with the RGA, the chamber was first pumped down to less than 10^{-4} mbar. The RGA should not be operated at gas pressures greater than 10^{-4} mbar. The base pressure of the chamber was usually on the order of 10^{-6} mbar during the mass scans. The resistance of the power resistor in the ion source circuit, as shown in Figure 4.3, was adjusted so that the heater current was 1.5-2.2 A. The ion source and lens bias voltages were then adjusted so that I_{Carpet} (the difference between the ion source and lens currents) was 20-150 nA.

Sodium, potassium, and rubidium alkali aluminosilicate ion sources from Heatwave Labs,

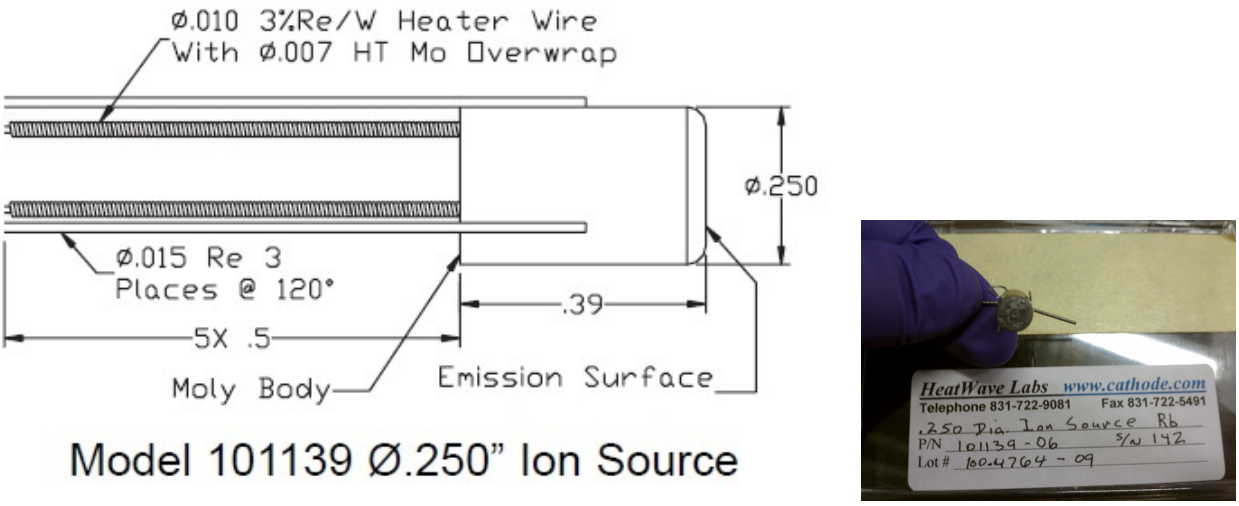

Figure B.2: Left: Schematic of the alkali aluminosilicate ion sources used during the measurements [15]. Right: Photograph of rubidium source #3 (Rb3).

Inc. [15] were tested as a part of this work. A schematic and image of an ion source is shown in Figure B.2. The need for the scans arose when measurements with a sodium ion source yielded efficiency results on par with efficiency results with a potassium ion source. The sodium ion transport efficiencies should have been worse than those of potassium ions due to the lighter mass of the sodium ions. Therefore, the composition of the source needed to be verified. The mass range of the scans was chosen to include the masses of the neighboring alkali elements of the sample source, and the mass increment of the scans was 0.1 nA. The following sources were used in this work: two rubidium (internal numbers Rb2 and Rb3), one potassium (K1) and one sodium (Na1). The results of the mass scans are shown in Figure B.3.

The rubidium and potassium sources were composed of the appropriate elements, as shown in Figure B.3. However, the sodium source contained mostly potassium and rubidium. After contacting the company, another sodium soure was procurred that did indeed contain sodium. The mass scans verifying its composition were taken after the completion of the

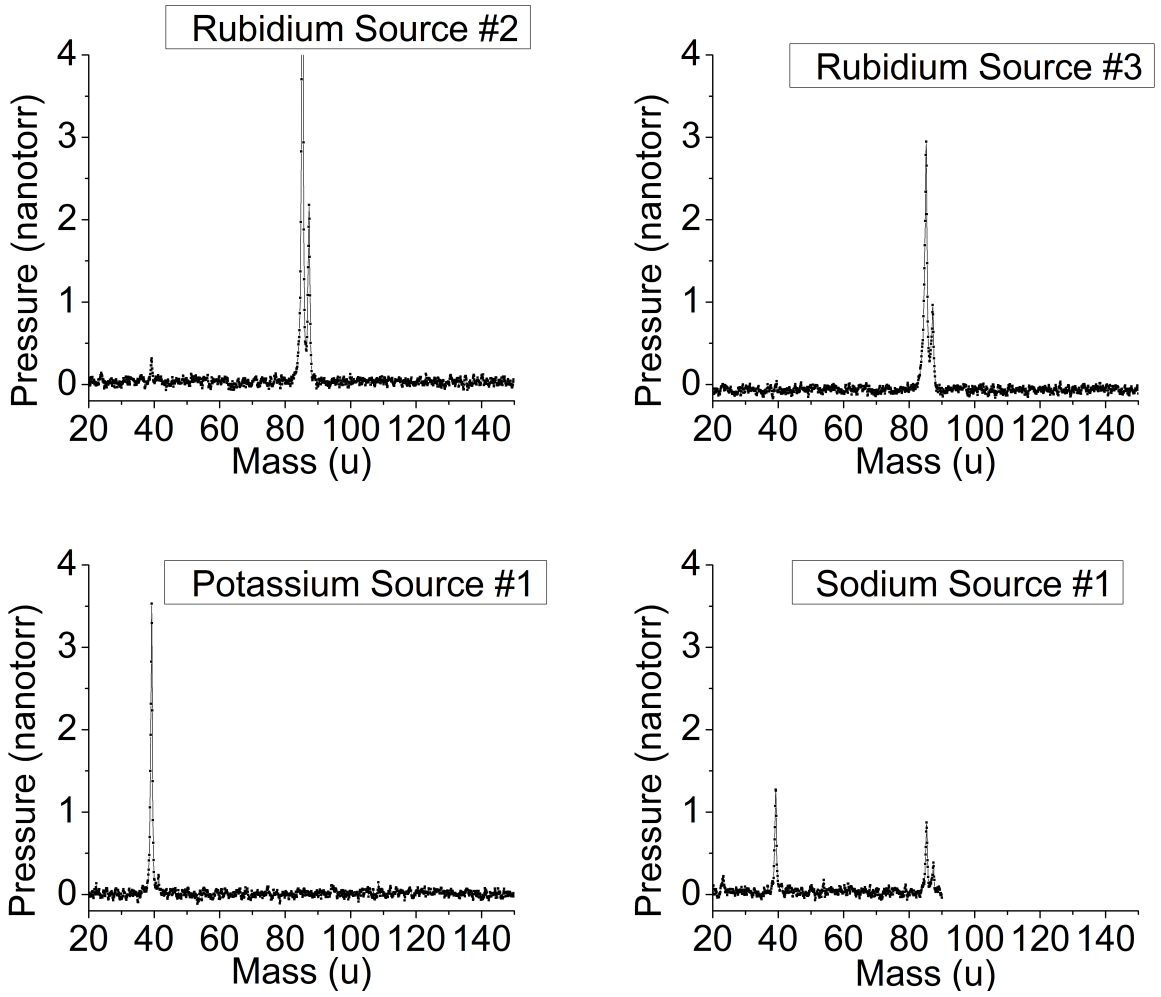

Figure B.3: Mass scans of the ion sources used in this work. All scans except the rubidium #3 scan were conducted with a source heating current of 2.01 A (1.77 A for Rb3). Upper left: Rubidium source used in all Rb^+ ion linear carpet measurements. Upper right: Rubidium source used in the circular carpet ion jumping experiments. Lower left: Potassium source used for all K^+ ion measurements. Lower right: Sodium source that instigated the verification of the ion source compositions.

work presented in this disseration. The procedure summarized above should be used to ascertain the composition of all future ion sources.

Appendix C

Carpet Design Considerations

This appendix presents details about the design and manufacturing process for the RF carpets used in this work. First, some of the parameters of printed circuit board (PCB) design are discussed, and then the programming language used to create PCBs is given with examples.

C.1 Manufacturing Limits and Other Considerations

The manufacturing capabilities for PCBs vary from company to company. The companies that have been found that can produce RF carpets that are suitable for this work are listed in Table C.1. When a PCB is designed, some limitations may have an impact on the carpet design, and other aspects of the manufacturing process must be specified when a PCB is ordered.

The maximum size of a PCB, the minimum trace and gap widths, and substrate options are usually listed on a company's website. For example, Innovative Circuits, Inc. has a maximum flex (Kapton) substrate PCB size of 45.7 cm by 61 cm. However, a 1.9 cm border

Table C.1: List of companies that have produced RF carpets for use at the NSCL.

Company	Type of Carpets Manufactured
Gigatek Inc.	drag field carpets
Stevenage Circuits	drag field carpets with more than 2 layers
Innovative Circuits, Inc.	drag field and surfing prototypes
Flexible Circuit Technologies, Inc.	large area carpets for cyclotron gas stopper

around the edge is necessary to hold the substrate in place and is not able to be printed, so the maximum size is actually 41.9 cm by 57.2 cm (referred to as the plottable area). A stiffner can be added to the border to ease mounting the PCB into a frame, or thick tape can be added as an alternative.

A company may be able to manufacture a few minimum trace widths and gaps in series, but as the number of traces increases, so does the probability of a short between two traces. If electrical testing is specified, the company will check the boards for shorts before the boards are shipped. It is advisable to ask a representative from the PCB companies what the minimum trace and space width would be for hundreds of traces before designing a RF carpet. The trace and space widths affect the price since smaller pitch will likely require more attempts to produce a non-shorted board. In addition, the capacitance increases with decreasing pitch (for constant γ). The capacitance of the carpets was calculated with the free program FastFieldSolvers [72].

A thin substrate was desired to minimize the capacitance of the PCB (electric field lines will pass through the insulating substrate). Flexible substrates are thinner than rigid substrates, and Kapton was chosen due to its low outgassing rate, low signal attenuation (constant voltages along the bus bars), and small changes in its properties when cooled to 80 K. The RF carpets were printed onto 1 mil thick Kapton. Kapton has a dielectric constant of $\sim$3.4.

The RF carpet PCBs were ordered with the following additional specifications: no surface finish, no mask, no legend, Oxyban anti-tarnish finish, and the smallest possible amount of copper deposited (usually 1/4 oz). The more copper deposited, the taller the trace and the larger the capacitance.

C.2 RF Carpet Design: GERBER Format

RS-274X, also called "Extended Gerber," is the data transfer format used in the design of PCBs. A guide to the GERBER can be found at http://www.ucamco.com. For this work, the files were written in Notepad and saved with the appropriate extension. The file extensions were .gbl, .gtl, and .goutline, which stand for GERBER bottom layer, GERBER top layer, GERBER outline, respectively. The "via" (plated holes through the substrate) locations are listed in a drill file which has .drd as the file extension. Other types of file extensions are defined, for example, .gts for top layer soldermask. Several free programs online can be used to view the GERBER files. Pentalogix Viewmate [75] and Gerbv [76] are examples of two of these programs. The layers, outline, and drill files could be viewed simultaneously, as shown in Figure C.1.

The coordinates of the PCB features must be specified relative to an origin. The origin was chosen to be either at the lower left corner of the plottable area or at the lower left corner of the entire PCB, and the position of the origin was communicated to the PCB company as part of the ordering process. An outline file was often created to provide a visual guide of the PCB features relative to the edges of the substrate, as shown in Figure C.1 (right).

A sample of GERBER code is given below:

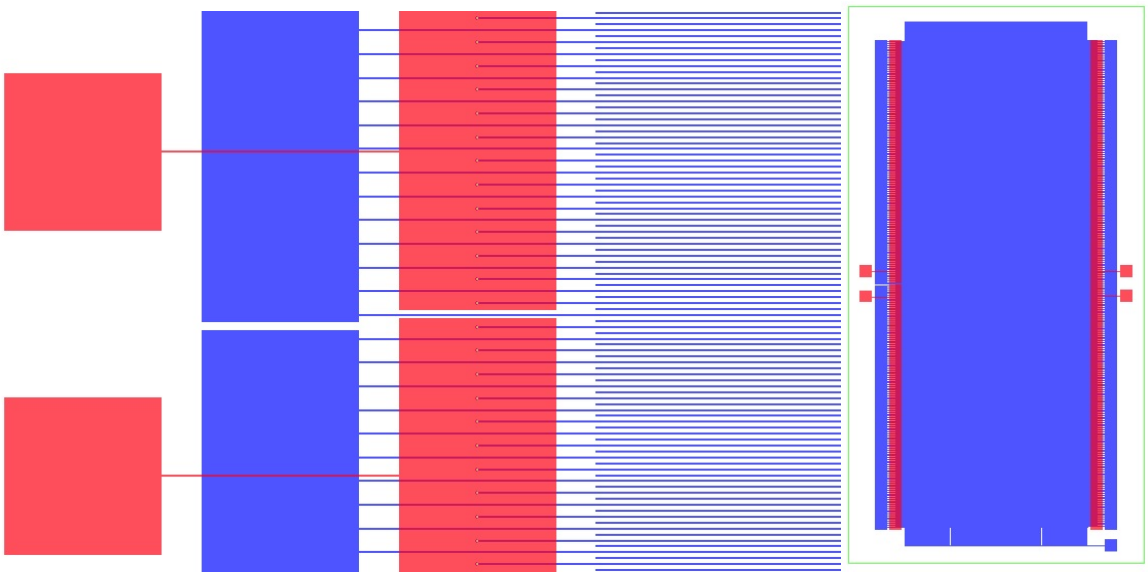

Figure C.1: The GERBER design files for the large linear prototype (see Chapter 5). The via drill holes appear as white dots, the top layer as blue, the bottom layer as red, and the outline as green. Left: Close-up of the large linear prototype at the boundary between the two regions. The carpet was divided into two segments so that it could be driven with two circuits if necessary. Right: Full view of the carpet with the green outline illustrating the position of the border of the PCB substrate.

```
G75*
G70*
%OFA0B0*%
%FSLAX24Y24*%
%IPPOS*%
%LPD*%
%ADD22R,1X0.2*%
D22*
X017500Y008900D02*X180000Y008900D01*
%ADD10C,0.005*%
D10*
G01X012525Y017500D02*G03X008349Y025642I010025J000000D01*
M02*
```

"G75*" sets the circular interpolation mode to multi-quadrant which allows a full circle to be drawn. The alternative is "G74*" which restricts circular traces to one quadrant. "G70" specifies that the units are in inches ("G71" for millimeters). "%OFA0B0*%" specifies the offset to be 0 along both the A and B axes. "%FSLAX24Y24%" is the format statement that

specifies the number of integers and decimal places for each axis (in this case, 2 integers and 4 decimal places for each axis), and the "LA" command omits leading zeros. "IPPOS" sets the image polarity to positive, and "LPD" sets the layer polarity to dark. These parameters set the image default to clear and the added features (the copper traces) to dark.

The aperture description, AD, defines the shape with which an image is drawn. "%ADD22R,1X0.2*%" defines an aperture, AD, with D-code number 22, and the aperture is called by its label, ie."D22*". The aperture is a rectangle, "R", which is 1" by 0.2". In order to draw a feature with this aperture, the beginning and end of the trace should be specified from the center of the aperture (ie. for a 2" line from left to right, the difference in the x axis would only be 1" since the aperture extends 0.5" beyond its center along the x axis). "%ADD10C,0.005*%" defines a circular aperture with a radius of 0.005", which was at the manufacturing limit of Innovative Circuits, Inc.

In order to draw a trace, the starting position is defined, here shown as X017500Y008900, followed by "D02*" which defines that at this point no image is generated (exposure off). The next set of coordinates, X180000Y008900, is followed by "D01*" which signals that an image should be drawn straight from the previously defined point to the given coordinate (exposure on). The second example draws a circular trace. "G01" is the default which calls for linear interpolation, and this G-code is used at the beginning of the trace. "G03" defines counter clockwise circular interpolation, and "G02" clockwise interpolation. The I and J coordinates after the X and Y coordinates of the trace end point specifiy properties of the arc drawn between the two points. The I coordinate is the offset between the arc start point and its center parallel to the X axis and the J coordinate is the offset between the arc start point and its center parallel to the Y axis. "M02*" ends the program.

The drill (.drd) file are slightly different. An example is given below:

```
%
M48
M72
T01C0.0100
%
T01
X000000Y000000
M30
```

"M48" specifies that the section is general header information, and "M72" sets the measurement units to inches (M71 for metric). The T codes define the drill hole size, and "M30" ends the program. No traces are drawn, the location of the holes is simply given.

In order to draw larger features that are not along an axis, several incremental, yet overlapping, traces can be drawn (preferably along the long axis). A scripting language could be used to quickly create GERBER code since most of the features of an RF carpet are evenly-spaced traces. The author preferred Microsoft Excel. The lines of code defining the traces were split into several cells along a row. For example, X would be in cell 1, 017500 in cell 2, Y in cell 3, etc. The "concatenate" command was used at the end of the row to reassemble the code. The separation of the numbers from the letters allowed the numerical values to be incremented. In addition, the "round" command was used to limit the X and Y coordinates to 4 decimal place values when sine and cosine functions were required to calculate the endpoint of the circular traces. The column of code was then copied into a Notepad file.

REFERENCES

REFERENCES

[1] L. Weissman, P.A. Lofy, D.A. Davies, D.J. Morrissey, P. Schury, S. Schwarz, T. Sun, and G. Bollen. First extraction tests of the NSCL gas cell. *Nucl. Phys. A*, 746:655–658, 2004. Proceedings of the Sixth International Conference on Radioactive Nuclear Beams (RNB6).

[2] M. Petrick, W.R. Plaβ, K.-H. Behr, A. Brünle, L. Caceres, J. Clark, Z. Di, S. Elisseev, M. Facina, A. Fettouhi, H. Geissel, W. Hüller, M. Huyse, C. Karagiannis, B. Kindler, R. Knöbel, Y. Kudryavtsev, J. Kurcewicz, T. Levant, Yu.A. Litvinov, B. Lommel, M. Maier, D.J. Morrissey, G. Münzenberg, M. Portillo, G. Savard, C. Scheidenberger, P. Van Duppen, H. Weick, M. Winkler, and B. Zabransky. Online test of the FRS ion catcher at GSI. *Nucl. Instrum. Meth. B*, 266(19-20):4493–4497, 2008. Proceedings of the XVth International Conference on Electromagnetic Isotope Separators and Techniques Related to Their Applications.

[3] Michiharu Wada, Yoshihisa Ishida, Takashi Nakamura, Yasunori Yamazaki, Tadashi Kambara, Hitoshi Ohyama, Yasushi Kanai, Takao M. Kojima, Youichi Nakai, Nagayasu Ohshima, Atsushi Yoshida, Toshiyuki Kubo, Yukari Matsuo, Yoshimitsu Fukuyama, Kunihiro Okada, Tetsu Sonoda, Shunsuke Ohtani, Koji Noda, Hirokane Kawakami, and Ichiro Katayama. Slow RI-beams from projectile fragment separators. *Nucl. Instrum. Meth. B*, 204:570–581, 2003. 14th International Conference on Electromagnetic Isotope Separators and Techniques Related to their Applications.

[4] Michiharu Wada. Deceleration and cooling of radioactive isotope beams - from Gev to μev. *Nucl. Instrum. Meth. A*, 532(1-2):40–47, 2004. International Workshop on Beam Cooling and Related Topics.

[5] G. Bollen. "Ion surfing" with radiofrequency carpets. *Int. J. Mass. Spectrom.*, 299(2-3):131–138, 2011.

[6] Walter Loveland, David J. Morrissey, and Glenn T. Seaborg. *Modern Nuclear Chemistry*. John Wiley & Sons, Inc., Hoboken, New Jersey, USA, 2006.

[7] N. Joshi, private communication.

[8] D.J. Morrissey, G. Bollen, M. Facina, and S. Schwarz. Pulsed extraction of ionization from helium buffer gas. *Nucl. Instrum. Meth. B*, 266(21):4822–4828, 2008.

[9] P. A. Lofy. Development of a high-pressure, gas-filled ion source for a radioactive beam facility. *Ph.D. Dissertation*, 2003.

[10] G. K. Pang. Development of radiofrequency carpets for ion transportation at the NSCL. *Ph.D. Dissertation*, 2011.

[11] S. Schwarz. RF ion carpets: The electric field, the effective potential, operational parameters and an analysis of stability. *Int. J. Mass. Spectrom.*, 299(2-3):71–77, 2011.

[12] M. Brodeur, A.E. Gehring, G. Bollen, S. Schwarz, and D.J. Morrissey. Experimental investigation of the ion surfing transport method. *Int. J. Mass. Spectrom.*, 336:53–60, 2013.

[13] Jerry Sevick. *Transmission Line Transformers*. Noble Publishing Corporation, USA, 2001.

[14] J. Ottarson, private communication.

[15] http://www.cathode.com.

[16] G. Bollen, D.J. Morrissey, and S. Schwarz. A study of gas-stopping of intense energetic rare isotope beams. *Nucl. Instrum. Meth. A*, 550(1-2):27–38, 2005.

[17] C. Guénaut, G. Bollen, S. Chouhan, F. Marti, D.J. Morrissey, D. Lawton, J. Ottarson, G.K. Pang, S. Schwarz, B.M. Sherrill, M. Wada, and A.F. Zeller. The cyclotron gas stopper project at the NSCL. *Hyperfine Interactions*, 173:35–40, 2006.

[18] G. Bollen, C. Campbell, S. Chouhan, C. Guénaut, D. Lawton, F. Marti, D.J. Morrissey, J. Ottarson, G. Pang, S. Schwarz, A.F. Zeller, and P. Zavodszky. Manipulation of rare isotope beams - from high to low energies. *Nucl. Instrum. Meth. B*, 266(19-20):4442–4448, 2008. Proceedings of the XVth International Conference on Electromagnetic Isotope Separators and Techniques Related to their Applications.

[19] http://isolde.web.cern.ch/isolde/.

[20] http://www.triumf.ca/about-triumf/triumf-faq/isac-backgrounder.

[21] H. L. Ravn. Radioactive ion beam projects based on the two accelerator or ISOL principle. *Philos. Trans. R. Soc. London, Ser. A*, 356(1744):1955–1984, 1998.

[22] M. Smith, M. Brodeur, T. Brunner, S. Ettenauer, A Lapierre, R. Ringle, V. L. Ryjkov, F. Ames, P. Bricault, G. W. F. Drake, P. Delheij, D. Lunney, F. Sarazin, and J. Dilling. First penning-trap mass measurement of the exotic halo nucleus ^{11}Li. *Phys. Rev. Lett.*, 101:202501, Nov 2008.

[23] W. Gelletly. Science with radioactive beams: The alchemist's dream. *Contemp. Phys.*, 42:285–314, 2001.

[24] R.F. Casten and B.M. Sherrill. The study of exotic nuclei. *Prog. Part. Nucl. Phys.*, 45, Supplement 1:S171–S233, 2000.

[25] D.J. Morrissey and B.M. Sherrill. Radioactive nuclear beam facilities based on projectile fragmentation. *Philosophical Transactions of the Royal Society of London. Series A: Mathematical, Physical and Engineering Sciences*, 356(1744):1985–2006, 1998.

[26] D.J. Morrissey, B.M. Sherrill, M. Steiner, A. Stolz, and I. Wiedenhoever. Commissioning the A1900 projectile fragment separator. *Nucl. Instrum. Meth. B*, 204:90–96, 2003. 14th International Conference on Electromagnetic Isotope Separators and Techniques Related to Their Applications.

[27] G. Bollen. Ion trap mass spectrometry of rare isotopes. *Acta. Phys. Pol. B*, 39:433–444, 2008.

[28] G Bollen and S Schwarz. Penning trap mass measurements on rare iosoptes - status and new developments. *J. Phys. B: At. Mol. Opt. Phys.*, 36:941–951, 2003.

[29] G. Bollen, D. Davies, M. Facina, J. Huikari, E. Kwan, P. A. Lofy, D. J. Morrissey, A. Prinke, R. Ringle, J. Savory, P. Schury, S. Schwarz, C. Sumithrarachchi, T. Sun, and L. Weissman. Experiments with thermalized rare isotope beams from projectile fragmentation: A precision mass measurement of the superallowed β emitter ^{38}Ca. *Phys. Rev. Lett.*, 96:152501, Apr 2006.

[30] S Schwarz, G Bollen, D Lawton, P Lofy, D.J Morrissey, J Ottarson, R Ringle, P Schury, T Sun, V Varentsov, and L Weissman. The low-energy-beam and ion-trap facility at NSCL/MSU. *Nucl. Instrum. Meth. B*, 204:507 – 511, 2003. 14th International

Conference on Electromagnetic Isotope Separators and Techniques Related to their Applications.

[31] A. A. Kwiatkowski, B. R. Barquest, G. Bollen, C. M. Campbell, R. Ferrer, A. E. Gehring, D. L. Lincoln, D. J. Morrissey, G. K. Pang, J. Savory, and S. Schwarz. Penning trap mass measurement of ^{26}Si. *Phys. Rev. C*, 81:058501, May 2010.

[32] C. J. Barton, D. S. Brenner, N. V. Zamfir, M. A. Caprio, A. Aprahamian, M. C. Wiescher, C. W. Beausang, Z. Berant, R. F. Casten, J. R. Cooper, R. L. Gill, R. Krücken, J. R. Novak, N. Pietralla, M. Shawcross, A. Teymurazyan, and A. Wolf. Mass measurement of ^{80}Y by β-γ coincidence spectroscopy. *Phys. Rev. C*, 67:034310, Mar 2003.

[33] L. Weissman, D.J. Morrissey, G. Bollen, D.A. Davies, E. Kwan, P.A. Lofy, P. Schury, S. Schwarz, C. Sumithrarachchi, T. Sun, and R. Ringle. Conversion of ^{38}Ca/^{37}K projectile fragments into thermalized ion beams. *Nucl. Instrum. Meth. A*, 540(2-3):245–258, 2005.

[34] R. Ringle, P. Schury, T. Sun, G. Bollen, D. Davies, J. Huikari, E. Kwan, D.J. Morrissey, A. Prinke, J. Savory, S. Schwarz, and C. Sumithrarachchi. Precision mass measurements with LEBIT at MSU. *Int. J. Mass. Spectrom.*, 251(2-3):300–306, 2006. Ultra-Accurate Mass Spectrometry and Related Topics.

[35] K. Minamisono, G. Bollen, P. F. Mantica, D. J. Morrissey, and S. Schwarz. Collinear laser spectroscopy and polarized exotic nuclei at NSCL. *Proceedings of the Institute for Nuclear Theory*, 16:180, 2009.

[36] A. Klose, K. Minamisono, Ch. Geppert, N. Frömmgen, M. Hammen, J. Krämer, A. Krieger, C.D.P. Levy, P.F. Mantica, W. Nörtershäuser, and S. Vinnikova. Tests of atomic charge-exchange cells for collinear laser spectroscopy. *Nucl. Instrum. Meth. A*, 678:114–121, 2012.

[37] H.-Jürgen Kluge and Wilfried Nörtershäuser. Lasers for nuclear physics. *Spectrochimica Acta Part B: Atomic Spectroscopy*, 58(6):1031–1045, 2003. LAP-2002 International Conference on Laser Probing.

[38] http://www.nscl.msu.edu/exp/sr.

[39] L. E. Linhardt, L. Baby, D. W. Bardayan, J. C. Blackmon, H. Gardiner, E. Johnson, E. Koschiy, K. T. Macon, M. Matos, B. C. Rasco, G. Rogachev, D. Santiago-Gonzalez, and I. Wiedenhoever. Measurement of ^{17}F + p reactions with ANASEN. *J. Phys.: Conf. Ser.*, 403:012036, 2012.

[40] D. Suzuki, M. Ford, D. Bazin, W. Mittig, W.G. Lynch, T. Ahn, S. Aune, E. Galyaev, A. Fritsch, J. Gilbert, F. Montes, A. Shore, J. Yurkon, J.J. Kolata, J. Browne, A. Howard, A.L. Roberts, and X.D. Tang. Prototype AT-TPC: Toward a new generation active target time projection chamber for radioactive beam experiments. *Nucl. Instrum. Meth. A*, 691:39–54, 2012.

[41] A. Simon, S.J. Quinn, A. Spyrou, A. Battaglia, I. Beskin, A. Best, B. Bucher, M. Couder, P.A. DeYoung, X. Fang, J. Görres, A. Kontos, Q. Li, S.N. Liddick, A. Long, S. Lyons, K. Padmanabhan, J. Peace, A. Roberts, D. Robertson, K. Smith, M.K. Smith, E. Stech, B. Stefanek, W.P. Tan, X.D. Tang, and M. Wiescher. Sun: Summing NaI(Tl) gamma-ray detector for capture reaction measurements. *Nucl. Instrum. Meth. A*, 703:16–21, 2013.

[42] J. Ärje, J. Äystö, H. Hyvönen, P. Taskinen, V. Koponen, J. Honkanen, A. Hautojärvi, and K. Vierinen. Submillisecond on-line mass separation of nonvolatile radioactive elements: An application of charge exchange and thermalization processes of primary recoil ions in helium. *Phys. Rev. Lett.*, 54:99–101, Jan 1985.

[43] Ranjan, M., Purushothaman, S., Dickel, T., Geissel, H., Plass, W. R., Schäfer, D., Scheidenberger, C., Van de Walle, J., Weick, H., and Dendooven, P. New stopping cell capabilities: RF carpet performance at high gas density and cryogenic operation. *EPL*, 96(5):52001, 2011.

[44] Guy Savard. Large radio-frequency gas catchers and the production of radioactive nuclear beams. *J. Phys.: Conf. Ser.*, 312(5):052004, 2011.

[45] W. Trimble, G. Savard, B. Blank, J.A. Clark, F. Buchinger, T. Cocolios, J.E. Crawford, A. Frankel, J.P. Greene, S. Gulick, J.K.P. Lee, A. Levand, M. Portillo, K.S. Sharma, J.C. Wang, B.J. Zabransky, and Z. Zhou. Development and first on-line tests of the RIA gas catcher prototype. *Nucl. Phys. A*, 746:415 – 418, 2004. Proceedings of the Sixth International Conference on Radioactive Nuclear Beams (RNB6).

[46] C. Scheidenberger, H. Geissel, M. Maier, G. Münzenberg, M. Portillo, G. Savard, P. Van Duppen, H. Weick, M. Winkler, M. Yavor, F. Attallah, K.-H. Behr, V. Chichkine, S. Eliseev, M. Hausmann, M. Hellström, E. Kaza, B. Kindler, Y. Litvinov, B. Lommel, G. Marx, M. Matos, N. Nankov, T. Ohtsubo, K. Sümmerer, Z.-Y. Sun, and Z. Zhou. Energy and range focusing of in-flight separated exotic nuclei - A study for the energy-buncher stage of the low-energy branch of the Super-FRS. *Nucl. Instrum. Meth. B*, 204:119–123, 2003. 14th International Conference on Electromagnetic Isotope Separators and Techniques Related to their Applications.

[47] H. Weick, H. Geissel, C. Scheidenberger, F. Attallah, T. Baumann, D. Cortina, M. Hausmann, B. Lommel, G. Münzenberg, N. Nankov, F. Nickel, T. Radon, H. Schatz, K. Schmidt, J. Stadlmann, K. Sümmerer, M. Winkler, and H. Wollnik. Slowing down of relativistic few-electron heavy ions. *Nucl. Instrum. Meth. B*, 164-165:168–179, 2000.

[48] L Weissman, D.A Davieas, P.A Lofy, and D.J Morrissey. Stopping energetic heavy ions in one-bar helium: narrow incident momentum distributions. *Nucl. Instrum. Meth. A*, 522(3):212–222, 2004.

[49] L. Weissman, D.A. Davies, P.A. Lofy, and D.J. Morrissey. Stopping energetic heavy-ions in one-bar helium: broad incident momentum distributions. *Nucl. Instrum. Meth. A*, 531(3):416–427, 2004.

[50] http://www.srim.org/.

[51] G. Savard, J. Clark, C. Boudreau, F. Buchinger, J.E. Crawford, H. Geissel, J.P. Greene, S. Gulick, A. Heinz, J.K.P. Lee, A. Levand, M. Maier, G. Münzenberg, C. Scheidenberger, D. Seweryniak, K.S. Sharma, G. Sprouse, J. Vaz, J.C. Wang, B.J. Zabransky, and Z. Zhou. Development and operation of gas catchers to thermalize fusion-evaporation and fragmentation products. *Nucl. Instrum. Meth. B*, 204:582–586, 2003. 14th International Conference on Electromagnetic Isotope Separators and Techniques Related to their Applications.

[52] C. Sumithrarachchi, private communication.

[53] Glenn F. Knoll. *Radiation Detection and Measurement*. John Wiley & Sons, Inc., Hoboken, New Jersey, USA, 2000.

[54] http://www-linux.gsi.de/ weick/atima/.

[55] O.B. Tarasov and D. Bazin. Lise++ : design your own spectrometer. *Nuclear Physics A*, 746:411 – 414, 2004. Proceedings of the Sixth International Conference on Radioactive Nuclear Beams (RNB6).

[56] A. Takamine, M. Wada, Y. Ishida, T. Nakamura, K. Okada, Y. Yamazaki, T. Kambara, Y. Kanai, T. M. Kojima, Y. Nakai, N. Oshima, A. Yoshida, T. Kubo, S. Ohtani, K. Noda, I. Katayama, P. Hostain, V. Varentsov, and H. Wollnik. Space-charge effects in the catcher gas cell of a rf ion guide. *Review of Scientific Instruments*, 76(10):103503, 2005.

[57] D. J. Morrissey. Extraction of thermalized projectile fragments from gas. *The Eur. Physs Jour. Spec. Top.*, 150:365–366, 2007.

[58] P. Dendooven, S. Purushothaman, and K. Gloos. On a cryogenic noble gas ion catcher. *Nucl. Instrum. Meth. A*, 558(2):580–583, 2006.

[59] S. Purushothaman, P. Dendooven, I. Moore, H. Penttilä, J. Ronkainen, A. Saastamoinen, J. Äystö, K. Peräjärvi, N. Takahashi, and K. Gloos. Cryogenic helium as stopping medium for high-energy ions. *Nucl. Instrum. Meth. B*, 266(19-20):4488–4492, 2008. Proceedings of the XVth International Conference on Electromagnetic Isotope Separators and Techniques Related to their Applications.

[60] L.M. Simons. The cyclotron trap for antiprotons. *Hyperfine Interactions*, 81:253–262, 1993.

[61] P. DeCecco, P. Hauser, D. Horváth, F. Kottmann, L.M. Simons, and D. Taqqu. A new method to produce a negative muon beam of kev energies. *Nucl. Instrum. Meth. A*, 394(3):287–294, 1997.

[62] I. Katayama, M. Wada, H. Kawakami, J. Tanaka, and K. Noda. Cyclotron ion guide for energetic radioactive nuclear ions. *Hyperfine Interactions*, 115:165–170, 1998.

[63] Yuri K. Batygin. Space charge effects in cyclotron gas stopper. *Nucl. Instrum. Meth. A*, 629(1):37–42, 2011.

[64] J. Throck Watson and O. David Sparkman. *Introduction to Mass Spectrometry*. John Wiley & Sons, Inc., Hoboken, New Jersey, USA, 2007.

[65] H.G. Dehmelt. Radiofrequency spectroscopy of stored ions - I: Storage. *Adv. At. Mol. Phys.*, 3:53–72, 1967.

[66] M.D. Lunney and R.B. Moore. Cooling of mass-separated beams using a radiofrequency quadrupole ion guide. *Int. J. Mass. Spectrom.*, 190-191:153–160, 1999.

[67] Earl W. McDaniel and Edward A. Mason. *Thermal Properties of Ions in Gas*. John Wiley & Sons, Inc., New York, USA, 1988.

[68] http://www.simion.com.

[69] Stefan Schwarz. IonCool-A versatile code to characterize gas-filled ion bunchers and coolers (not only) for nuclear physics applications. *Nuclear Instruments and Methods*

in Physics Research Section A: Accelerators, Spectrometers, Detectors and Associated Equipment, 566(2):233–243, 2006.

[70] http://developer.imagej.net/downloads.

[71] http://www.innovative-circuits.com.

[72] http://www.fastfieldsolvers.com/.

[73] http://www.flexiblecircuit.com/.

[74] http://www.thinksrs.com/products/rga.htm.

[75] http://www.pentalogix.com/viewmate.php.

[76] http://gerbv.sourceforge.net/.